Softening and Damage Behavior of Human Arteries

Experiments, Constitutive Modeling and Numerical Simulation

Zur Erlangung des akademischen Grades eines
Doktors der Technischen Wissenschaften
ausgeführte Dissertation

eingereicht an der
Fakultät für Elektrotechnik und Informationstechnik
der Technischen Universität Graz

von

Hannah Weisbecker

Betreuer: Univ.-Prof. Dipl.-Ing. Dr. techn. Gerhard A. Holzapfel

February 2014

Abstract

Cardiovascular diseases are the leading cause of death in the western world. Modern medicine is moving towards less invasive surgery such as catheter-based interventions that reduce pain and hospitalization for the patient. However, these interventions are highly demanding for the surgeon due to the lack of direct feedback from the surgical site. During these interventions high stresses and even damage may occur, e.g., due to stent expansion and balloon inflation. Numerical models, informed by experimental data on the mechanical response of human tissue at supra-physiological loads, can improve the design of stents, balloons and surgical procedures. This PhD Thesis aims to develop a computational framework for modeling catheter-based interventions with an appropriate constitutive damage model fitted to experimental data for human arterial tissues. Consequently, the work comprises three major topics, namely, experiments, mathematical modeling and computational simulation.

The experimental work involves uniaxial extension tests on human aortas in both physiological and supra-physiological load ranges. These tests are conducted on the intact wall, on the separated layers, intima, media and adventitia, and on the enzyme treated media. In the enzyme treated specimens elastin and collagen, the main load bearing components of the arterial wall, are degraded to better understand the contributions of these components on the damage and softening behavior.

For modeling the softening behavior of the tissue, an established hyperelastic constitutive model was extended with a damage function. Such a strain-energy function is capable of describing the Mullins-like behavior of arterial tissue. The experimental data, together with results from fitting the model, suggest that softening and damage are primarily associated with the collagen fibers.

The framework for numerical simulations to model damage in patient-specific geometries accounts for initial stresses, i.e. residual stresses and prestresses. Residual stresses are those stresses present in an unloaded artery to adjust transmural stresses at physiological loads that result from the different material properties of intima, media and adventitia. A method to include the residual stresses on patient-specific geometries is developed. If the geometry of an artery is derived from *in vivo* medical imaging, it is loaded by blood pressure. Hence, the finite element algorithm has to account for this load on the given geometry. This work presents an advanced method to include prestresses which reduces computational costs compared to available algorithms.

In the future, more detailed experimental data on the inter-patient and intra-patient variability in the mechanical response of human tissue and thus of material parameters will further enhance the framework for patient-specific modeling of damage in human arteries. Furthermore, multiscale models may lead to a better understanding of the damage mechanism.

Zusammenfassung

Krankheiten des Herz-Kreislauf-Systems sind die führende Todesursache in der westlichen Welt. Die moderne Medizin entwickelt katheterbasierte Eingriffe, durch die Schmerzen gelindert und Krankenhausaufenthalte verkürzt werden. Solche Eingriffe stellen hohe Ansprüche an den Chirurgen, da dieser kein direktes Feedback von dem Ort des Eingriffes erhält. Außerdem kann es z. B. beim Einsetzen eines Stents und beim Aufblasen eines Ballons zu hohen Spannungen und Schädigungen im Gewebe kommen. Mit numerischen Modellen ist eine Verbesserung der Formgebung von Stents und Ballons möglich. Eine Voraussetzung dafür sind experimentelle Daten der mechanischen Eigenschaften des menschlichen Gewebes. Diese Arbeit stellt eine numerische Simulationsmethode für katheterbasierte Operationen vor, die auf ein durch experimentelle Daten gestütztes konstitutives Modell für menschliches Arteriengewebe zurückgreift. Sie befasst sich mit den drei Teilaspekten: Experimente, mathematische Modellierung und numerische Simulation.

Der experimentelle Teil der Arbeit untersucht das mechanische Verhalten von menschlichen Aorten bei physiologischen und supra-physiologischen Dehnungen anhand uniaxialer Zugversuche. Unterschieden wird dabei zwischen den drei Schichten, Intima, Media und Adventitia. Die mechanisch relevanten Komponenten der Arterienwand, Elastin und Kollagen, werden in der Media spezifisch von Enzymen verdaut. Auf diese Weise lässt sich der Einfluss beider Komponenten auf die Schädigung im Gewebe untersuchen.

Zur Modellierung der Entfestigung des Gewebes dient ein etabliertes hyperelastisches Modell, das durch die Erweiterung mit einer Schädigungsfunktion den „Mullinseffekt“ in arteriellem Gewebe beschreibt. Die experimentellen Daten zeigen, zusammen mit den Ergebnissen aus dem Parameterfit des Modells, dass die Entfestigung des Gewebes hauptsächlich mit den Kollagenfasern zusammenhängt.

Das numerische Schädigungsmodell berücksichtigt sowohl Residuumsspannungen als auch Vorspannungen im Gewebe. Residuumsspannungen treten in der unbelasteten Arterienwand auf, um die Spannungsgradienten über die Wandstärke auszugleichen, die durch die unterschiedlichen Materialeigenschaften von Initma, Media und Adventitia auftreten. Eine in der Arbeit entwickelte Methode bindet die Residuumsspannungen in patientenspezifische Geometrien ein. Wird die Geometrie einer Arterie aus *in vivo* Bildgebungsverfahren rekonstruiert, ist sie bereits mit Blutdruck belastet und dadurch verformt. Dies muss im finite Elemente Algorithmus berücksichtigt werden. Dieser Teil der Arbeit beschreibt eine Methode, um Vorspannungen zu berücksichtigen, welche den notwendigen Rechenaufwand gegenüber bestehenden Algorithmen verringert.

In der Zukunft können detailliertere experimentelle Daten über die Veränderlichkeit von Materialkennwerten in einem Patienten und zwischen verschiedenen Patienten numerische Modelle weiter verbessern. Außerdem ermöglicht die Weiterentwicklung von mehrskaligen Modellen ein besseres Verständnis für die Schädigungsmechanismen.

Preface

My sincere thanks go to Professor Gerhard A. Holzapfel for giving me the opportunity to write my PhD Thesis at the Institute of Biomechanics at Graz University of Technology. I am very grateful for the numerous productive discussions on arterial mechanics.

The work was funded by the European Commission under the 7th Framework Programme in the scope of the project SCATh – Smart Catheterization. My thanks go to Professor David M. Pierce for coordinating the project at the Institute of Biomechanics and for supporting my work.

Special thanks go to Professor Ray W. Ogden for agreeing to be an examiner of this Thesis and for sharing his knowledge of nonlinear continuum mechanics.

I wish to thank Gerhard Sommer for sharing his experience in the experimental characterization of biological tissue and Michael J. Unterberger for valuable discussions on material modeling. Furthermore I gratefully acknowledge the help and support of all my colleagues and the students at the Institute of Biomechanics.

I gratefully acknowledge the support of Professor Peter Regitnig and Christian Viertler, who prepared and discussed histological specimens of the arterial wall. My thanks go to Borja Rodríguez Vila for providing the patient-specific finite element mesh of an aorta.

Furthermore, I would like to thank Peter Neumeister and Professor Jonas Stålhand for their support and their good advice.

Finally, my thanks go to my sister and my parents who supported me throughout the time that I worked on this Thesis.

CONTENTS

1 INTRODUCTION

1.1 Motivation

Cardiovascular diseases go far back in human history. Allam et al. [1] show that artherosclerosis is commonplace in Egyptian mummies from a time of the Middle Kingdom the Greco-Roman period. Nowadays cardiovascular diseases are the leading cause of death in the western world. In Europe cardiovascular diseases cause over 4 million deaths each year. This corresponds to 47 % of all deaths in Europe. Consequently, cardiovascular diseases causes high costs with an estimated €196 billion per year to the EU economy [2]. Similar trends are reported for the United States and China, where 32.8 % and 32.0 % of all deaths are attributed to cardiovascular disease, respectively [3, 4].

Modern medicine is developing towards less invasive surgical procedures where open surgery is being replaced by catheter-based interventions. These reduce pain and hospitalization for the patient. However, they are highly demanding for the surgeon and thus still have unacceptably high risks for patients. If the surgeon is provided with visual or haptic feedback for catheter guidance, patient safety can be improved.

Deployment of stents-grafts or inflation of intra-aortic balloons can cause large deformations in the aorta, thus generating high stresses which may cause damage in the tissue. Typically, an endograft for endovascular repair of aortic aneurysms is oversized by $10-20$ % to maintain adequate sealing between the vessel and the graft [5]. Intra-aortic balloon inflation aims at temporarily shutting down the blood flow. Thus, such balloons also induce large deformations and high stresses to the aorta.

Finite element simulation can provide informations to enhance these surgical procedures in two ways. First, based on simulation of induced stresses and damage, catheter and stent-design can be improved. Second, real-time evaluation of stress and damage fields in surgery can support the surgeon. For example, visual feedback can show the stress distribution in the arterial tissue at the site of balloon inflation or stent expansion. In both cases, the mechanical properties of the arterial wall have to be determined experimentally. Then, stress and damage distribution can be computed from numerical simulations with reasonable accuracy. Finite elements provide an excellent framework to model soft biological tissues with large deformations. The aim of this PhD Thesis is to develop a computational framework to model catheter-based interventions and to supply model parameters from experiments on human tissues.

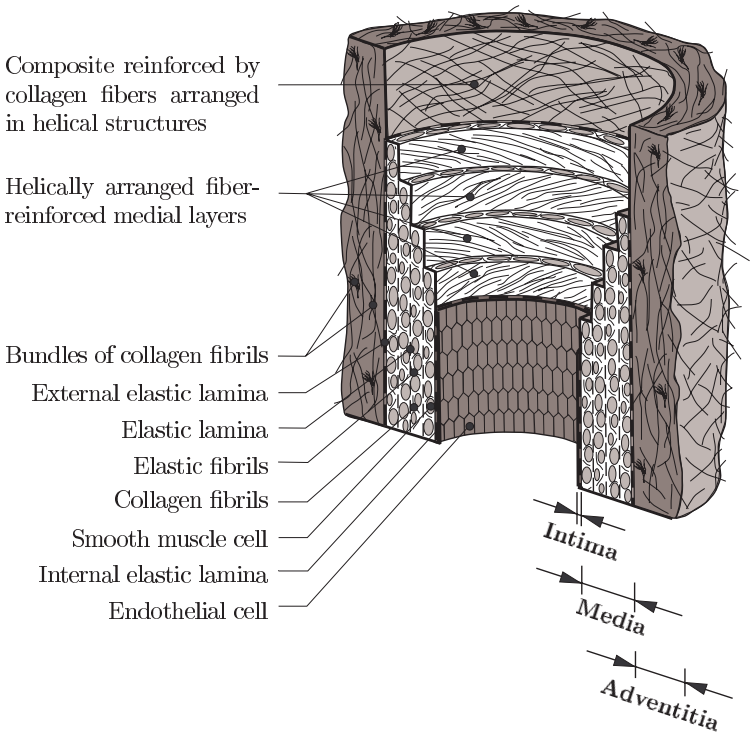

Figure 1.1: Three-layered structure of an aged artery showing I: intima, M: media and A: adventitia, adapted from [7].

The mechanism for the softening in arterial tissue is still not fully understood. More experiments including mechanical and ultrastructural examinations are needed for a better understanding. This information will facilitate the development of structural mechanical models based on the physical principles that lead to softening and damage.

1.2 Arterial Tissue

Insight in the structure of the arterial wall is a prerequisite for an adequate mechanical description of the tissue. This section describes the components of main interest for the mechanical modeling. For a detailed description of the morphology of the arterial wall, the reader is referred to [6].

1.2.1 Structure of Arterial Wall

Arteries consist of three layers, the innermost layer is the intima followed by the media and the adventitita, as shown in Fig. 1.1. Intima and media are separated by the elastic lamina interna, and media and adventitia are separated by the elastic lamina externa.

In healthy young arteries, the intima consists of a single layer of endothelial cells and is assumed to bear no load. With age the intima thickens due to deposit of collagen fibers and smooth muscle cells and thus becomes relevant from the mechanical point of view.

The media is a sandwich-like structure of elastin, bundles of collagen fibrils and smooth muscle cells. Two families of collagen fibers are helically wound around the lumen and the smooth muscle cells have a circumferential alignment.

The adventitia comprises collagen fibers organized in thick bundles which form two helically arranged families of fibers within a ground matrix. Fibroblasts regulate the synthesis of extracellular matrix and collagen.

1.2.2 Elastin

Elastin is responsible for the elasticity and resilience of extracellular tissues such as lung, ligament, tendon and skin. It consists of a massively crosslinked array of tropoelastin. In large arteries elastic fibers form concentric rings around the lumen.

Elastin is the main component of the elastic fibers of which it forms the elastic internal core. It is interdispersed and surrounded by microfibrils [8]. Electronmicroscopy studies suggest that parallel-aligned filaments build up a fibrillar substructure of elastin [9]. The Marfan syndrome is caused by the loss of functionality of fibrilin, another component of the elastic fibers [10].

1.2.3 Collagen

Collagen is the most abundant protein in vertebrae. Apart from being an important constituent of blood vessels, different collagen types are found in other connective tissue like bone, tendon, cartilage, teeth and skin.

The collagen molecule consists of three helically wound peptide chains. The human aortic wall mainly consists of collagen type I and III. Both are fibrillar collagens where type I consists of two identical peptide chains and a third distinct peptide chain and type III consists of three identical chains [11]. The adventita predominantly contains collagen type I, the media contains approximately 30 % of collagen type I and 70 % of type III and the initma contains mainly collagen type III [12]. Mutations in collagen can lead to diseases like osteogenesis imperfecta or the Ehlers-Danlos syndrome. Scurvy is a disease were collagen fibrils can no longer be synthesized any due to the lack of vitamin C [13].

1.2.4 Other Mechanically Relevant Components

Azeloglu et al. [14] show that proteoglycans can regulate residual stresses in the aorta. Hence, proteoglycans have a significant influence on the stress distribution in arterial tissue. In [15] a microstructural model is proposed in which proteoglycans serve as crosslinks between collagen fibrils.

The aforementioned components only describe the passive behavior of aortic tissue. For an active stress contribution smooth muscle cells need to be considered. Models of the active response of smooth muscle cells have been proposed, e.g., in [16–19].

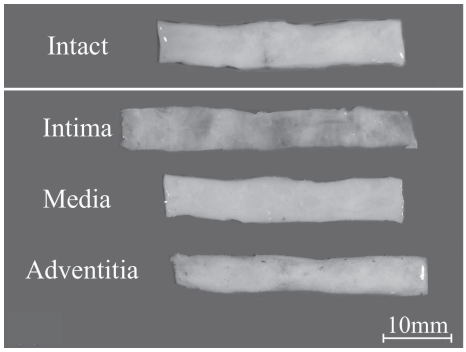

Figure 1.2: Residual stresses in the artery, adapted from [24]. The top figure shows the intact wall with three layers. The bottom figure shows intima, media and adventitia of the intact tissue strip after separation. The change of dimensions for the different layers, resulting from residual stresses within the tissue, is apparent.

1.2.5 Incompressibility

Arterial tissue is commonly modeled as an incompressible material. Experimental data support this assumption, e.g., Lawton [20] shows that the volume changes upon elongation are negligible. Furthermore, Carew et al. [21] investigate the volume change under internal pressure and longitudinal stretch.

1.2.6 Residual Stresses

In the load-free configuration, arteries are still in a stressed state. These residual stresses have a significant influence on the in vivo transmural stress distribution and render the stress distribution more uniform. When the arteries are cut, these residual stresses are released leading to deformations.

Early researchers investigated residual stresses in arteries by measuring the opening angles of radially cut arterial rings, e.g., [22, 23]. The residual stress state, however, is more complex. Holzapfel et al. [24] show that also upon separation of the layers residual stresses are set free, as illustrated in Fig. 1.2. The intima expands after separation whereas the media and adventitia contract. This means that the intima is under compression, and the media and adventitia are under tension in the three-layer composite.

1.3 Continuum Mechanical Framework

The framework of continuum mechanics describes the mechanical fields such as strain and stress in the artery by treating bodies like a continuum and disregarding the molecular or atomic structure. The fundamentals of nonlinear solid mechanics are detailed e.g., in [25].

1.3.1 Description of Continuum Mechanical Quantities

The position vector $\mathbf{X}$ labels a point on a body with respect to the reference configuration Ω_0 at $t = 0$. The position vector $\mathbf{x}$ labels a point on a body with respect to the current configuration Ω_t at $t > 0$. To describe the state of the body one has hence two possibilities.

In the Lagrangian description one follows a material particle and describes the continuum mechanical quantities such as displacement, strain and stress in terms of the reference configuration. This approach is commonly used in solid mechanics.

In the Eulerian description one describes the continuum mechanical quantities in terms of a fixed point in space. Consequently, they are expressed in terms of the current configuration. This approach is commonly used in fluid mechanics.

1.3.2 Kinematics

The displacement of a point labeled with $\mathbf{X}$ in the reference configuration Ω_0 and with $\mathbf{x}$ in the current configuration Ω_t is $\mathbf{u} = \mathbf{x} - \mathbf{X}$. This deformation is fully described by the deformation gradient tensor

$$\mathbf{F} = \frac{\partial \mathbf{x}}{\partial \mathbf{X}} = \mathbf{I} + \frac{\partial \mathbf{u}}{\partial \mathbf{X}}, \tag{1.1}$$

where $\mathbf{I}$ is the identity tensor. The deformation gradient is nonsymmetric and connects the initial configuration to the current configuration. The determinant

$$J = \det\mathbf{F} \tag{1.2}$$

describes the volume change of the material, where $J = 1$ denotes an incompressible deformation. In order to obtain a measure for the deformation, which neglects rigid body motion, the symmetric right and left Cauchy-Green tensors

$$\mathbf{C} = \mathbf{F}^{\mathrm{T}}\mathbf{F}, \qquad \mathbf{b} = \mathbf{F}\mathbf{F}^{\mathrm{T}}, \tag{1.3}$$

respectively, are used.

1.3.3 The Concept of Stress

Stress is defined as the force per unit surface area. For large deformations different stress measures are defined as both force and unit surface area can be measured in the reference and in the current configurations.

The traction vector $\mathbf{t}$ is defined as the current force per current unit surface area with the outward normal vector $\mathbf{n}$. Cauchy's theorem

$$\mathbf{t} = \boldsymbol{\sigma}\mathbf{n} \tag{1.4}$$

states the existence of a unique second-order tensor $\boldsymbol{\sigma}$. The Cauchy stress tensor $\boldsymbol{\sigma}$, also referred to as true stress tensor, is compatible with the Eulerian description. The symmetry of $\boldsymbol{\sigma}$ is postulated by the equilibrium of angular momentum.

For the first Piola-Kirchhoff stress tensor **P** the current force is related to the reference unit surface area. It can be derived from the Cauchy stress tensor as

$$\mathbf{P} = J\boldsymbol{\sigma}\mathbf{F}^{-\mathrm{T}}, \tag{1.5}$$

using Nanson's formula. The first Piola-Kirchhoff stress is in general non-symmetric and due to its definition a two point tensor with one index referring to the current and one index referring to the reference configuration.

The second Piola-Kirchhoff stress tensor **S** is fully compatible with the Lagrangian description. With a pull-back operation it is obtained from the Cauchy stress tensor as

$$\mathbf{S} = J\mathbf{F}^{-1}\boldsymbol{\sigma}\mathbf{F}^{-\mathrm{T}}. \tag{1.6}$$

Results are commonly reported using the Cauchy stress tensor. The eigenvalues of $\boldsymbol{\sigma}$ correspond to the principal stresses and the corresponding eigenvectors point in the directions of the principal stresses.

1.3.4 Hyperelasticity

One refers to a material as hyperelastic if a potential Ψ exists from which the stress can be derived. The Helmholz free-energy function Ψ is defined per unit reference volume. If $\Psi = \Psi(\mathbf{F})$ only depends on the deformation gradient it is called strain-energy function.

The Cauchy stress tensor is computed from the partial derivatives of Ψ as

$$\boldsymbol{\sigma} = J^{-1}\frac{\partial\Psi(\mathbf{F})}{\partial\mathbf{F}}\mathbf{F}^{\mathrm{T}}. \tag{1.7}$$

The normalization condition requires that the strain-energy function vanishes in the stress-free reference configuration and from physical considerations it is obvious that the strain-energy function increases with deformation, i.e.

$$\Psi(\mathbf{I}) = 0 \quad \text{and} \quad \Psi(\mathbf{F}) \geq 0. \tag{1.8}$$

Objectivity is required for constitutive equations, i.e. the strain energy has to be independent of rigid body motion. Therefore Ψ may only depend on the stretching part of **F** and

$$\Psi(\mathbf{F}) = \Psi(\mathbf{QF}) \tag{1.9}$$

must hold for all orthogonal tensors **Q**. It follows that by formulating the strain-energy function $\Psi(\mathbf{C})$ in terms of the right Cauchy-Green tensor **C** it fulfills the necessary and sufficient conditions for the strain energy to be objective, because the rotational part of **F** is removed.

The strain-energy function may be represented in terms of a set of independent strain invariants. For $\mathbf{C}$ these invariants are

$$I_1 = \mathrm{tr}(\mathbf{C}), \quad I_2 = \frac{1}{2}[\mathrm{tr}(\mathbf{C})^2 - \mathrm{tr}(\mathbf{C}^2)], \quad I_3 = \det(\mathbf{C}). \tag{1.10}$$

For an anisotropic material with two families of fibers, the strain-energy function also depends on the direction vectors $\mathbf{M}$ and $\mathbf{M}'$, i.e. $\Psi = \Psi(\mathbf{C}, \mathbf{M}\otimes\mathbf{M}, \mathbf{M}'\otimes\mathbf{M}')$. The number of independent invariants is increased to nine with the pseudo-invariants

$$\begin{aligned} I_4 = \mathbf{M}\cdot\mathbf{C}\mathbf{M}, \quad I_5 = \mathbf{M}\cdot\mathbf{C}^2\mathbf{M}, \quad I_6 = \mathbf{M}'\cdot\mathbf{C}\mathbf{M}', \quad I_7 = \mathbf{M}'\cdot\mathbf{C}^2\mathbf{M}', \\ I_8 = \mathbf{M}\cdot\mathbf{C}\mathbf{M}', \quad I_9 = (\mathbf{M}\cdot\mathbf{M}')^2. \end{aligned} \tag{1.11}$$

Note that I_4 and I_6 represent the square of the stretch in the directions $\mathbf{M}$ and $\mathbf{M}'$, respectively. To minimize the number of material parameters, constitutive equations for arterial tissue usually only consider the invariants I_1, I_4 and I_6 [7].

1.3.5 Nonlinear Finite Element Formulation

The nonlinear behavior of arterial tissue, including large deformation and initial stresses, pose several challenges to the finite element modeling. Nonlinearity in finite element formulations applied to arterial tissue has two causes: nonlinearity of the material models and nonlinearity due to large deformations.

Arterial tissue has a nonlinear stress-stretch response with exponential stiffening. For nonlinear material models the stiffness matrix $[\mathbf{K}]$ depends on the displacement $[\mathbf{u}]$ and thus changes during loading. An iterative method such as the Newton-Raphson method can solve the nonlinear equation

$$[\mathbf{K}(\mathbf{u})]\,[\mathbf{u}] = [\mathbf{f}], \tag{1.12}$$

where $[\mathbf{f}]$ is the vector of external forces.

Upon loading, arterial tissues may undergo large deformations. Hence, the weak or variational formulation of the equilibrium equations can be described in the initial or in the current configuration, also referred to as total Lagrangian and updated Lagrangian formulations [26].

Additionally, pressure always remains normal to the surface. Hence, it is not a conservative load and can not be derived from a potential function. This means that the tangent matrix is, in general, unsymmetric and an unsymmetric solver for the Newton-Raphson method is necessary [27].

1.3.6 Incompressible Materials

Standard displacement-based finite element formulations show volumetric locking for incompressible or nearly incompressible materials. A solution to this problem is a mixed variational approach following the Hu-Washizu principle. Here the variables solved for in the matrix representation of the finite element problem are the displacement **u**, the pressure p and the volume change J [28].

To facilitate the computation of incompressible materials the models are implemented in a compressible form and rendered incompressible with a penalty parameter. To this end a multiplicative decomposition of the deformation gradient $\mathbf{F} = J^{1/3}\overline{\mathbf{F}}$ is introduced that splits the deformation into a volumetric $J^{1/3}\mathbf{I}$ and an isochoric $\overline{\mathbf{F}}$ part, where $\det\overline{\mathbf{F}} = 1$. This multiplicative decomposition yields $\mathbf{C} = J^{2/3}\overline{\mathbf{C}}$. The strain-energy function Ψ is split into a volumetric (spherical) Ψ_{vol} and an isochoric (deviatoric) $\overline{\Psi}$ part according to

$$\Psi(\mathbf{C}) = \Psi_{\text{vol}}(J) + \overline{\Psi}(\overline{\mathbf{C}}). \tag{1.13}$$

An example for the volumetric part of the strain-energy function is

$$\Psi_{\text{vol}} = \frac{K}{2}\log(J)^2, \tag{1.14}$$

where K is a penalty parameter. The quasi-incompressible solution coincides with the incompressible solution if it is sufficiently large.

1.3.7 Initial Stresses

The term initial stress includes residual stresses and prestresses. Residual stresses are those stresses present in the load-free configuration. Prestresses are present in geometries reconstructed from medical imaging an result from *in vivo* axial pre-stretch and blood pressure.

Medical imaging is usually performed in vivo, and hence the reconstructed model geometry in the problem of interest has in vivo boundary conditions, e.g., a blood vessel at physiological blood pressure. However, classical finite element methods assume that simulations begin from an unloaded, stress-free reference condition. The problem, hence, is that the in vivo determined 'initial' geometry is not an unloaded reference configuration. To address this problem, Gee et al. [29, 30] proposed a method to include prestresses to patient-specific geometries of abdominal aortic aneurysms based on an updated Lagrangian approach.

As part of this PhD Thesis, their algorithm was generalized and implemented to a finite element software. The details are presented in Chapter 4. Briefly, an incremental deformation gradient is calculated from the incremental displacement for which each iteration step is solved. The incremental displacement is then deleted and the deformation gradient is updated with the incremental deformation gradient. Compared to the inverse design

analysis [31, 32], where the actual load free configuration is computed, the prestressing algorithm is not prone to buckling and it is easier to implement.

Usually the opening angle method is used to incorporate residual stress to arterial models by closing an arterial segment with a certain opening angle prior to loading, see, e.g., [33, 34]. Alastrué et al. [35] include residual stresses to a patient-specific model based on the opening angle method. The residual stress state, however, is more complicated and different dimension of the arterial layers after separation should be considered. Chapter 4 presents a method to account for the data of Holzapfel et al. [24]. A summary of the literature modeling residual stress in patient-specific diseased arteries using the finite element method is provided in Table 1 of [36].

1.4 Hyperelastic Modeling of Arterial Tissue

Several constitutive models have been proposed for arterial tissue. This section gives an overview of the hyperelastic models proposed for arteries and their characteristics.

1.4.1 Constitutive Equation

Commonly, the passive behavior of arterial tissue is modeled as an incompressible fiber reinforced tissue. Assuming that the elastin matrix behaves isotropically, it is modeled with an isotropic strain energy-function Ψ_{m}. The symmetrically aligned collagen fibers stiffen exponentially and are thus modeled with an anisotropic strain-energy function Ψ_{f}. The original form of the deviatoric part of such a strain-energy function is introduced in [7]

$$\begin{aligned}\overline{\Psi} &= \overline{\Psi}_{\mathrm{m}} + \overline{\Psi}_{\mathrm{f},4} + \overline{\Psi}_{\mathrm{f},6} \\ &= \frac{\mu}{2}(\bar{I}_1 - 1) + \sum_{i=4,6} \frac{k_1}{2k_2}\{\exp[k_2(\bar{I}_i - 1)^2] - 1\},\end{aligned} \tag{1.15}$$

where $\mu > 0$ and $k_1 > 0$ are stress like parameters and $k_2 > 0$ is a dimensionless parameter. The modified invariants are defined as $\bar{I}_a = J^{-2/3} I_a$ for $a = 1, 4, 6$. It is assumed that the fibers are only load bearing under tension, therefore, the anisotropic term $\Psi_{\mathrm{f},i}$ only contributes if $\bar{I}_i > 1$.

1.4.2 Fiber Dispersion

The assumption that all fibers are aligned exactly in the directions $\mathbf{M}$ and $\mathbf{M}'$ is not correct as already shown by [37]. It is possible to account for the dispersion of the fibers phenomenologically by replacing $\Psi_{\mathrm{f},i}$ in (1.15) with

$$\overline{\Psi}_{\mathrm{f},i} = \frac{k_1}{2k_2} \exp\{k_2[(1-\rho)(\bar{I}_1 - 3)^2 + \rho(\bar{I}_i - 1)^2]\}, \quad i = 4, 6, \tag{1.16}$$

where $0 \leq \rho \leq 1$ is a dimensionless parameter [38]. The higher the parameter ρ, the higher the isotropic contribution in the exponential response of the fibers. A structurally motivated way of introducing dispersion is the dispersion parameter κ in (1.15) where the pseudo-invariant $\bar{I}_4$ is replaced by $\bar{I}_4^* = \kappa\bar{I}_1 + (1-3\kappa)\bar{I}_4$ [39], i. e.

$$\overline{\Psi}_{\mathrm{f},i} = \frac{k_1}{2k_2}[\exp\{k_2[\kappa\bar{I}_1 + (1-3\kappa)\bar{I}_i - 1]^2\} - 1], \quad i = 4,6. \tag{1.17}$$

Again, the value of $\kappa \in [0, 1/3]$ determines the proportion of isotropic contribution in the mechanical response of the fibers. Both models encompass (1.15) as limiting cases for $\rho = 1$ and $\kappa = 0$, respectively. The main drawback of these models is, that they assume rotational symmetry of the fiber dispersion around the main fiber direction.

Recent measurements of the three-dimensional fiber distribution of collagen fibers [40] in the arterial layers show that collagen fibers are aligned closer to the axial direction in the adventitia, closer in the circumferential direction in the media and around 45° in the intima. The data also suggest that the assumption of rotational symmetry does not hold. The dispersion is rather in the axial and circumferential plane with very low dispersion along the radial direction. The first continuous three-dimensional distribution of collagen fibers is reported in [41], showing that the media has an alternating preferred fiber orientation through the thickness of the wall. Such structural data are a precondition for adequately modeling arterial tissue and the softening mechanism within the tissue.

Gasser [42] uses a Bingham distribution, which is not rotationally symmetric, to account for the different fiber dispersion in the tangential and cross-sectional plane to model the mechanical behavior of aneurysm tissue. However, they still use a phenomenological model for the collagen fibers.

1.4.3 Fiber Crimping

A further aspect that can be included in the models is fiber crimping. The collagen fibers show a wavy arrangement in the unloaded configuration and are only load bearing after they are straightened. One approach to account for this is the introduction of the additional parameters $I_{04} > 1$ and $I_{06} > 1$ that account for the crimping of the fibers in the unloaded state by altering the exponential expression in (1.15) to [43]

$$\overline{\Psi}_{\mathrm{f},i} = \exp[k_2(\bar{I}_i - I_{0i})^2] - 1, \quad i = 4,6. \tag{1.18}$$

In this case the anisotropic term only contributes if $\bar{I}_i > I_{0i}$, i.e. when the square of the stretch of the fibers is greater than I_{0i}. A different approach was used by Li and Robertson [44], who introduce an activation criterion for the recruitment of the collagen fibers using a metric for the deformation following a scalar measure of strain.

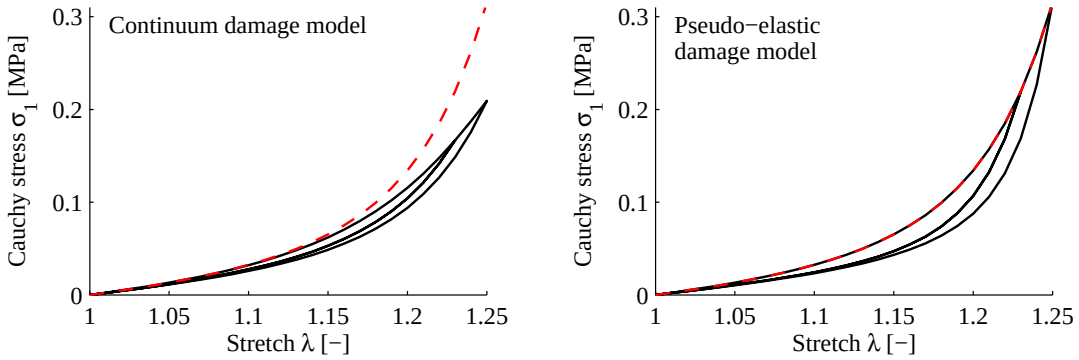

Figure 1.3: Continuum (a) and pseudo-elastic damage model (b) for cyclic loading using the same parameters for the undamaged strain-energy function (red). Contrary to the pseudo-elastic model, for the continuum damage model the primary loading does not correspond to the undamaged strain-energy function.

1.5 Damage Modeling of Arterial Tissue

There are two common approaches to add softening to the hyperelastic strain-energy functions, namely the continuum damage approach and the pseudo-elastic approach. In either way, a hyperelastic strain-energy function is multiplied by a reduction factor that governs the softening behavior of the material. The two different approaches, originally developed to describe the mechanical behavior of rubber, are introduced in the following.

1.5.1 Continuum Damage Models

The continuum damage model [45] has the form

$$\Psi(\mathbf{C},D) = (1-D)\Psi^0(\mathbf{C}), \tag{1.19}$$

where Ψ^0 is the effective strain-energy function and $0 < D \leq 1$ is an internal variable describing the softening of the material. Incorporating damage only in the deviatoric part of the strain-energy function and assuming that softening only occurs in the anisotropic term of the tissue response yields the constitutive equation

$$\overline{\Psi} = \overline{\Psi}_{\mathrm{m}} + (1-D_{\mathrm{f}})\overline{\Psi}^0_{\mathrm{f}}. \tag{1.20}$$

The isochoric part of the second Piola-Kirchhoff stress tensor is obtained by the differentiation of the strain-energy function with respect to the right Cauchy-Green tensor. It has the form

$$\overline{\mathbf{S}} = \overline{\mathbf{S}}_{\mathrm{m}} + \overline{\mathbf{S}}_{\mathrm{f}}, \quad \overline{\mathbf{S}}_{\mathrm{m}} = 2\frac{\partial \overline{\Psi}_{\mathrm{m}}}{\partial \mathbf{C}}, \quad \overline{\mathbf{S}}_{\mathrm{f}} = (1 - D_{\mathrm{f}})\overline{\mathbf{S}}_{\mathrm{f}}^{0}, \quad \overline{\mathbf{S}}_{\mathrm{f}}^{0} = 2\frac{\partial \overline{\Psi}_{\mathrm{f}}^{0}}{\partial \mathbf{C}}. \tag{1.21}$$

Figure 1.3(a) shows the stress-stretch response of the Cauchy stress computed from $\overline{\mathbf{S}}_{\mathrm{f}}^{0}$ (red) and $\overline{\mathbf{S}}_{\mathrm{f}}$ (black) for the continuum damage model. The damage variable D_{f} governs the hysteresis, leading to the typical Mullins-type behavior. The stress without including the damage variables differs from the primary loading path.

A possible evolution for the damage variable is given by Miehe [46] as

$$D(\alpha) = D_{\max}\left[1 - \exp\left(-\frac{\alpha}{\beta}\right)\right], \tag{1.22}$$

where $D_{\max}$ and β are dimensionless model parameters. $D_{\max}$ constrains the maximum softening and β determines how fast this softening occurs during the loading process. The evolution of the damage is governed by the variable α which depends on the maximum thermodynamic force that occurred over the history of the loading. Examples of other evolution equations are given in [47]. The continuum damage approach allows the inclusion of continuous softening as introduced in [46].

1.5.2 Pseudo-Elastic Damage Models

The pseudo-elastic model has a common strain-energy function for the primary loading path and a different strain-energy function for the unloading and reloading paths. This function is augmented by the damage variable η which modulates the softening behavior. In a general formulation, a pseudo-elastic strain-energy function Ψ has the form [48]

$$\Psi(\mathbf{C}, \eta) = \eta\,\Psi^{0}(\mathbf{C}) + \Phi(\eta), \tag{1.23}$$

where $0 < \eta \leq 1$ is a damage variable, $\Psi^{0}(\mathbf{C})$ is the strain-energy function of the undamaged material and $\Phi(\eta)$ is referred to as a damage function. Per definition the damage variable equals $\eta = 1$ on the primary loading curve. A possible pseudo-elastic strain-energy function for soft tissue is

$$\overline{\Psi} = \overline{\Psi}_{\mathrm{m}} + \eta_{\mathrm{f}}\overline{\Psi}_{\mathrm{f}} + \Phi_{\mathrm{f}}. \tag{1.24}$$

The corresponding second Piola-Kirchhoff stress tensor $\overline{\mathbf{S}}$ has the form

$$\overline{\mathbf{S}} = 2\frac{\partial \overline{\Psi}_{\mathrm{m}}}{\partial \mathbf{C}} + 2\eta_{\mathrm{f}}\frac{\partial \overline{\Psi}_{\mathrm{f}}^{0}}{\partial \mathbf{C}} = \overline{\mathbf{S}}_{\mathrm{m}} + \eta_{\mathrm{f}}\overline{\mathbf{S}}_{\mathrm{f}}^{0} = \overline{\mathbf{S}}_{\mathrm{m}} + \overline{\mathbf{S}}_{\mathrm{f}}. \tag{1.25}$$

Figure 1.3(b) shows the stress-stretch response of the Cauchy stress computed from $\overline{\mathbf{S}}_{\mathrm{f}}^{0}$ (red) and $\overline{\mathbf{S}}_{\mathrm{f}}$ (black) for the pseudo-elastic damage model. The essential difference to

Fig. 1.3(a) is that the primary loading curve and the stress response of the undamaged material coincide.

A possible evolution equation for the damage variable is proposed in [48] as

$$\eta = 1 - \frac{1}{r}\mathrm{erf}\left[\frac{1}{m}(\overline{\Psi}^{\max} - \overline{\Psi}^{0})\right], \tag{1.26}$$

where $\Psi^{\max}$ is the maximum of the strain energy reached over the history of the deformation. The parameter $r > 1$ defines the maximum of the damage that can be accumulated as the error function $\mathrm{erf}(x)$ for $x \geq 0$ only spans between 0 and 1. The parameter $m > 0$ determines how fast damage is accumulated. The damage variable equals $\eta = 1$ on the primary loading curve so that it is possible to fit the material parameters independently from the damage parameters. The pseudo-elastic model can be extended to model the residual deformation after unloading which is observed for arterial tissue [49].

Guo and Slys [50] compare the performance of a continuum damage model and a pseudo-elastic model to fit the mechanical response of rubber-like material. As expected both models can well describe the Mullins type behavior of the material. However, the agreement for the pseudo-elastic model is much better. This results from the fact that the parameter estimation is much simpler, because material and damage parameters are fitted separately. For the continuum damage model, all parameters have to be determined simultaneously, leading to a more complicated problem for parameter estimation.

1.5.3 Multiscale Damage Models

To provide a basic review on damage models for arterial tissue, the concepts of the multiscale models, namely the unit sphere and the reference volume element approach, are briefly presented. Introducing a failure criterion on the mircoscopic scale, i.e. for the collagen fiber network, leads to multi-scale damage models.

The concept of microsphere models for fibrous tissue under affine deformation goes back to Lanir [51]. The constitutive behavior of a single fiber, i.e. the behavior on the microscale, is formulated explicitly. Then the macroscopic strain energy is obtained by integrating the strain energy of the fibers over a unit sphere. Anisotropy in fiber alignment is included in the integrand by a density function. The theory was expanded to non-affine deformations by Miehe et al. [52].

Using representative volume elements for the finite element method, one can determine the macroscopic behavior of a material based on the microscopic structure. These models have two length scales, the microscopic scale of the reference volume element and the macroscopic scale of the finite element domain. The concept is described by Chandran and Barocas [53] with the following four solution steps. First, a guess of the macroscale deformation is generated for the macroscopic problem in which the finite element equations are formulated. Second, downscaling determines the deformation of the boundaries of the

reference volume element from the macroscopic deformation. Third, the microscopic problem is solved with the prescribed boundary conditions and the stresses in the microscale network are computed. Last, upscaling determines the average stress on the macroscale.

1.5.4 Experimental Data

Oktay et al. [54] first reported changes in the mechanical behavior of arteries after overstretching. They compare the mechanical response for the inflation of carotid arteries of canines before and after inflating a balloon catheter. An increase in diameter after the balloon inflation indicates that softening due to damage occurred.

Horny et al. [55] report experimental data of uniaxial extension tests for human aortic tissue. However, they tested the intact tissue without separating the layers and thus neglect the different mechanical and softening behavior of intima, media and adventitia.

Famaey et al. [56] evaluated tissue damage after arterial clamping by endothelial and smooth muscle integrity tests for mouse abdominal aorta. Unfortunately, tissue loading is only quantified by the external load, i.e. the clamping force, such that the stress-state inside the tissue remains unknown. Furthermore, data obtained from animal tissue should not be directly used to model surgical procedures for humans. One apparent difference, for example, is the intimal thickening that is only observed in human arteries and absent in animals [57]. However, such experiments give valuable insight in the impacts of supraphysiological loading.

The data presented in Chapter 2 are the first to determine the layer-specific material and damage parameter for human aortic tissue. They are a prerequisite for patient-specific numerical models of catheter-based interventions and may help understanding the role of each layer in softening and damage. Constitutive fitting suggests that softening is related to the collagen fibers and not to the elastin matrix. To verify this hypothesis, Chapter 3 presents data on elastase treated and on collagenase treated tissue and relates the structural changes after enzyme treatment to changes in the mechanical behavior. The data presented in this PhD Thesis are the first to show experimentally that damage is only associated to the collagen fibers, i.e. to the anisotropic part of the strain-energy function.

1.5.5 Application of Damage Models to Arterial Tissue

Hokanson and Yazdani [58] propose an anisotropic damage model for arteries using a fourth-order weighting tensor linked to the Ogden material model. The model can represent the Mullins effect, however, the model does not account for the anisotropy in the tissue and it is more complicated than utilizing a scalar damage variable.

Balzani et al. [59] introduce a continuum damage model assuming that damage is only accumulated in the anisotropic part of the strain-energy function, i.e. in the collagen fibers of the arterial tissue. The model describes the softening behavior qualitatively well, nonetheless, it is not calibrated to experimental data. Furthermore a value for the strain energy is defined that describes the initial damage state. This means softening due to preconditioning

is disregarded and softening due to damage is defined by a parameter which is arbitrarily defined without sound experimental data. Furthermore, the approach implies that there is a sharp threshold between softening in physiological and supra-physiological conditions.

Subsequently, Balzani et al. [60] propose a framework for continuum damage models that are able to reflect remanent strains. The model gives a good qualitative fit to one set of experimental data. Again, the issue of separation between softening due to preconditioning and softening due to damage is not addressed adequately. The uniaxial extension data are preconditioned to a stress of about 100 kPa which is an arbitrary value in light of the fact that uniaxial extension does not mimic physiological loading conditions.

A continuum damage model is also used by Marini et al. [61] to describe damage in aortic aneurysm tissues. They do not focus on the softening but consider the yield point as the initiation of damage, i.e. the point at which the tangent modulus has its maximum. Unfortunately, the damage model does not advance the identification of rupture prone aneurysms compared to other risk indices. However, the initiation of damage could be used to trigger growth and remodeling processes in mechanobiological models.

Rodríguez et al. [43] use a stochastic model where the fibers of different lengths are modeled as worm-like chains, an approach which requires justification. Collagen fibers of different length fail at different stretches and the increase of stretch leads to a consecutive failure of the fibers. Thus, a damage mechanism is naturally introduced in the fiber bundle. However, the worm-like chain model is an entropy based theory and on the scale of collagen fibers a model based on stored energy should be favored. The finite element implementation and numerical examples are presented in [62]. Again the calibration of this structurally motivated model is the biggest challenge due to the lack of experimental data.

Calvo et al. [63] present a continuous damage model for fibrous biological tissue that describes discontinuous softening in both matrix and fibers. Compared to the model proposed by Rodríguez et al. [43], it does not need to be calibrated at two different length scales. A comparison of the two models [64] shows that the performance is similar with a larger localization of damage in the stochastic model. However, the results in the Chapters 2 and 3 show that softening is not present in the matrix but only associated with the collagen fibers.

Li and Robertson [65] consider two damage mechanisms, mechanical damage and enzymatic damage, for the matrix. No softening is considered for the collagen fibers. The motivation for enzymatic damage is to model the growth of aneurysms rather than modeling mechanical damage due to supra-physiological stresses.

Peña et al. [66] consider continuous and discontinuous damage in their damage model following an approach introduced in [46]. In [67, 68] they add viscoelasticity in the damage models. Subsequently, Peña [69] bases a new approach for softening in the collagen fibers on the strain-energy function given in (1.18) where she weights the recruitment stretch

I_{0i} with an internal variable. This is a more structurally motivated approach to introduce softening compared to including the damage variable in front of the strain-energy function. Furthermore, the model also describes a permanent deformation observed after unloading arterial tissue.

Famaey et al. [70] propose a damage model that accounts for damage in three structural components of the aortic wall, namely the elastin matrix, the collagen fibers and the smooth muscle cells. This leads to a total of 21 parameters to describe the constitutive behavior. They propose an active and a passive damage mechanism for the smooth muscle cells driven by the maximum strain energy encountered by the smooth muscle cells and the matrix respectively. A finite element example discusses the influence of the passive smooth muscle cell damage.

In an experimental study Colombo et al. [71] show that mean strain does not significantly influence cell growth whereas variations in the cyclic strain amplitude result in a significant change in cell proliferation and apoptosis. These data motivate a damage model for smooth muscle cells that does not primarily depend on the maximum strain energy reached over the history, but considers the strain amplitude in the damage criterion. This is supported by experimental data on airway smooth muscle showing that the cells remodel when stretched up to twice their initial length [72, 73].

Including the active response within damage models and better understanding cell proliferation and apoptosis in response to supra-physiological loads are very important steps towards better and more reliable damage models.

Gasser [15] models damage on the collagen fiber level and defined an irreversible rearrangement of proteoglycans. The macroscopic stress is obtained by integrating over a unit sphere. Even though the model describes a possible mechanism for the softening in arterial tissue, sound experimental evidence is missing to support the assumptions.

Sáez et al. [74] propose a microsphere-based damage model in which they regard damage evolution in each integration direction separately. They show that the number of integration points for the integration performed over the unit sphere greatly depends on the number of integration points which are beyond the yield point of the tissue. To obtain a smooth response a high number of points is necessary leading to high computational costs for finite element models.

Hadi et al. [75] propose a multi-scale model for finite elements with a representative volume element comprised of a discrete fiber network. The fibers are represented by nonlinear springs whose stiffness approaches zero if the stretch reaches a critical value. This can either be interpreted as a rupture of a fiber or as a failure of fiber-to-fiber cross-links. The model is capable of predicting macroscopic failure of type I collagen gels.

A general problem for multiscale models is parameter identification because there are not enough experimental data, and thus the damage mechanisms are not yet well understood.

These models, however, can be used to test hypotheses on damage mechanisms and motivate experimental investigations.

The damage model presented in this PhD Thesis uses the pseudo-elastic approach due to advantages in the parameter estimation. One focus of this study lies on the use of patient-specific material parameters, therefore it is important that the experimental data are approximated well by the constitutive model. The model and its fit to experimental data are presented in Chapter 3 and we show that damage is only related to the collagen fibers. In a finite element framework for patent-specific modeling of damage it is applied in Chapter 5.

1.6 Organization of the PhD Thesis

The PhD Thesis is a compilation of four scientific papers presented in the following chapters:

- *'Layer-Specific Damage Experiments and Modeling of Human Thoracic and Abdominal Aortas with Non-Atherosclerotic Intimal Thickening'*, Weisbecker H, Pierce DM, Regitnig P and Holzapfel GA, J. Mech. Behav. Biomed. Mater., 12:93-106, 2012.
- *'The role of elastin and collagen in the softening behavior of the human aortic media'*, Weisbecker H, Viertler C, Pierce DM and Holzapfel GA, J. Biomech., 46:1859-1865, 2013.
- *'A generalized prestressing algorithm for finite element simulations of pre-loaded geometries with application to the aorta'*, Weisbecker H, Pierce DM and Holzapfel GA, Int. J. Numer. Method. Biomed. Eng., in press.
- *'A computational framework for patient-specific modeling of human arteries considering initial stresses and supra-physiological loads'*, Weisbecker H, Pierce DM, Rodriguez-Vila B, Gómez EJ and Holzapfel GA, submitted.

The first paper presents experimental data on human aortic tissues in physiological and supra-physiological load ranges for the separated layers: intima, media and adventitia. Based on these data we propose a pseudo-elastic damage model for human arterial tissue. The results indicate that damage is only associated to the anisotropic response of the collagen fibers. The second paper more closely investigates the role of elastin and collagen in the softening behavior observed in the media by enzymatic digestion of one of these components, respectively. Our results support the hypothesis that the softening behavior is only associated with the anisotropic response of the collagen fibers. The third paper presents a numerical method to include prestretches into finite element geometries. The prestretches are present in patient-specific geometries because medical imaging is performed *in vivo*, and hence the aorta is loaded with internal blood pressure and axial prestretch. The fourth

paper describes a finite element framework for modeling stress and damage distributions on a patient-specific framework by including residual stresses and prestresses. The experimental data and the model presented in the first paper are applied here again.

The work of this PhD Thesis contributed also to the following peer-reviewed journal papers, conference proceedings and conference lectures:

- Weisbecker H, Unterberger MJ, Holzapfel GA, *Constitutive modeling of arteries considering fiber recruitment and the 3D fiber distribution*, in preparation.
- Pierce DM, Fastl TE, Weisbecker H, Rodriguez-Vila B, Gómez EJ and Holzapfel GA, *A method for incorporating residual stretches/stresses into patient-specific simulations of arteries*, in preparation.
- Unterberger MJ, Weisbecker H, Holzapfel GA, *Torsion of a circular cylinder versus simple shear as a modeling basis for rheometer experiments: application to rubber and actin networks*, submitted.
- Pierce DM, Fastl TE, Weisbecker H, Rodriguez-Vila Bz, Gómez EJ and Holzapfel GA, *A method for incorporating residual stresses into patient-specific finite element simulations of arteries with an example on AAAs*, 6th European Congress on Computational Methods in Applied Sciences and Engineering (ECCOMAS 2012), Vienna, Austria, September 10 – 14, 2012.
- Weisbecker H, Pierce DM, Holzapfel GA, *Layer-specific modeling of damage induced softening in the human aorta and the influence of residual stretches*, 8th European Solid Mechanics Conference (ESMC2012), Graz, Austria, July 9 – 13, 2012.
- Fastl TE, Pierce DM, Weisbecker H and Holzapfel GA, *A method for incorporating residual stresses into finite element simulations with an application to abdominal aortic aneurysms*, 8th European Solid Mechanics Conference (ESMC 2012), Graz, Austria, July 9 – 13, 2012.
- Weisbecker H, Pierce DM, Rodriguez-Vila B, Gómez EJ and Holzapfel GA, *Patient-specific modeling of human thoracic aortas with consideration of damage*, SCATh Joint Workshop on New technologies for Computer/Robot Assisted Surgery, Madrid, Spain, July 9 – 10, 2012
- Weisbecker H, Pierce DM, Regitnig P, Holzapfel GA, *Damage modeling of the human aorta: Influence of collagenase and elastase*, 18th Congress of the European Society of Biomechanics (ESB2012), Lisbon, Portugal, July 1 – 4, 2012.
- Pierce DM, Weisbecker H, Schriefl AJ, Rodriguez-Vila B, Gómez EJ, Holzapfel GA, *Modeling arterial tissue and intraluminal thrombus: experimental and numerical results*, 2nd International Conference on Material Modelling (ICMM2) incorporating

the 12th European Mechanics of Materials Conference, Paris, France, August 31 – September 2, 2011.

- Weisbecker H, Pierce DM, Holzapfel GA, *Pseudo-elastic finite element modeling of damage in arterial tissue*, IUTAM Symposium on Computer Models in Biomechanics: from Nano to Macro, Stanford, California, USA, August 29 – September 2, 2011 (Poster presentation).
- Weisbecker H, Pierce DM, Holzapfel GA, *Pseudo-elastic modeling of damage for healthy human aortas with non-atherosclerotic intimal thickening*, 82nd Annual Scientific Conference of the International Association of Applied Mathematics and Mechanics (GAMM2011), Graz, Austria, April 18 – 21, 2011.
- Weisbecker H, Pierce DM, Holzapfel GA, *Modeling of damage-induced softening for arterial tissues*, Proceedings of the Joint Workshop on New Technologies for Computer/Robot Assisted Surgery, Graz, Austria, July 11 – 13, 2011.

2 LAYER-SPECIFIC DAMAGE EXPERIMENTS AND MODELING OF HUMAN THORACIC AND ABDOMINAL AORTAS WITH NON-ATHEROSCLEROTIC INTIMAL THICKENING

Abstract Many treatments for cardiovascular diseases include an endovascular insertion of stents or stent grafts into arteries, a procedure which may cause high tissue stresses and even damage in the arterial wall. In order to study such problems by using finite element methods, both appropriate constitutive models and experimental data on human tissue samples are required. Layer-specific experimental data for human tissue tested up to the supra-physiological loading range are rare in the literature. In this study intact and layer-separated experimental data from uniaxial extension tests are presented for human thoracic and abdominal aortas with non-atherosclerotic intimal thickening undergoing supra-physiological loading. A novel pseudo-elastic damage model, proposed to describe discontinuous softening in aortic arterial tissues, is fit to the obtained experimental data. Fitting of the model with and without consideration of damage accumulation in the non-collagenous matrix material reveals that tissue damage is primarily related to the collagen fiber fabric. By employing the fit model, the effect of aortic tissue pre-conditioning on the material parameters from the resulting data fits is evaluated. Histological examination of the collagen fibers under different applied stretches is used to gain more insights into the structural changes of the tissue under supra-physiological loading.

2.1 Introduction

Cardiovascular diseases are one of the leading causes of death in the western world [76]. Treatment protocols for various pathologies of the aorta often include the insertion of stent grafts such as endovascular thoracic or abdominal aneurysm repair. The deployment of stent grafts can generate high stresses and may cause damage in the arterial wall. To improve finite element (FE) studies aimed at improving the design of stent geometries and to facilitate the application of catheter-based procedures, we study the supra-physiological stress-strain response of human aortic tissue.

Little experimental data for the stress-strain response of arterial tissue in the supra-physiological range exists in the literature. Data on animal tissue, for example, for canines [54], help with a basic understanding of the behavior of arterial tissue. However, such data are not adequate for FE modeling of surgical procedures as the specific properties of the tissue vary among species. To the authors' knowledge the only supra-physiological experimental

data on human tissue was presented recently by Horný et al. [55] who conduct uniaxial tension tests on the intact human aorta. Unfortunately, no layer-specific data are yet presented so that it is not possible to differentiate the amount of damage which may be induced in the individual tissue layers, i.e. intima, media and adventitia.

In the present study uniaxial tension tests are conducted on both intact and layer-separated human aortic tissue samples, taken from both the thoracic and abdominal regions. Using uniaxial tension tests, high supra-physiological loading is induced in the tissue, a crucial requirement for damage experiments. The biaxial tension test is better able to mimic the physiological loading conditions, but the test is difficult to perform at higher loads because of the attachment with hooks that rupture the tissue at comparatively low strains. Nonetheless, a careful experimental protocol and fitting procedure can successfully determine reliable material parameters for anisotropic, hyperelastic constitutive models, as shown by Holzapfel [77]. Experimental tests are realized with three repeated load cycles for every prescribed load step in order to study both continuous softening and discontinuous softening described by the Mullins effect. Histological specimens are prepared and analyzed for tissues loaded to different stretches in an effort to examine possible changes in the mechanically relevant components.

In young arteries the intima is a thin layer of endothelial cells such that only the media and the adventitia are load bearing. In aged arteries, however, the intima thickens and all three layers are load bearing, and hence relevant from the mechanical point of view. The individual tissue layers can be modeled as fiber-reinforced composites with an isotropic matrix, mainly comprised of elastin, and two symmetrically arranged families of collagen fibers [7]. The material model was subsequently extended to account for the dispersion in the collagen fiber directions [39] and is used to model the hyperelastic material behavior observed after pre-conditioning of the tissue.

Hokanson and Yazdani [58] proposed a damage model for arteries by using a fourth-order weighting tensor to account for possible anisotropy of damage. This model can describe discontinuous damage, where damage accumulates only at loads higher than the maximum load reached within the deformation history. However, the approach is relatively complicated compared to the approach used in continuum damage mechanics, where a scalar damage variable serves as a reduction factor for an effective strain-energy function. Balzani et al. [78] introduced a continuum damage model assuming that damage accumulates only in the collagen fibers of the arterial tissue. This model can successfully describe damage-induced softening qualitatively, but it has not been calibrated to data, and hence the modeling assumptions were not proven experimentally. Balzani et al. [60] recently presented an extended version of the model and a good fit to one set of experimental data on the media of a human carotid artery. Rodríguez et al. [43] chose to model the collagen fibers using a worm-like chain approach. Discontinuous softening is introduced by defining different failure stresses for bundles of collagen fibers with different lengths. A FE implementation and numerical examples are presented by Rodríguez et al. [79]. Here again, due

to the lack of experimental data, calibration of this structurally-motivated model remains the biggest challenge.

Calvo et al. [63] presented a stochastic damage model for fibrous biological tissues which describes discontinuous softening in both the tissue matrix and the fibers. Compared to the model presented by Rodríguez et al. [43] it does not need to be calibrated at two different length scales. Alastrué et al. [64] compared these models and showed that the performance of the two models was similar, although with a larger localization of damage in the stochastic model. Li and Robertson [65] considered two damage mechanisms for the matrix, mechanical and enzymatic damage, whereas no softening of the fibers was considered. The inclusion of enzymatic damage was motivated by the study of aneurysm growth, rather than modeling mechanical damage due to supra-physiological stresses. Peña et al. [66] added continuous damage, where damage is always accumulated even at loads lower than the maximum reached within the deformation history, to the discontinuous damage in their models, following an approach introduced by Miehe [46].

In the present study a pseudo-elastic approach, which was first introduced by Ogden and Roxburgh [48], is used to describe damage-induced softening of arterial tissues. In the pseudo-elastic theory, the primary loading curve is described by an elastic strain-energy function. For unloading and reloading of the tissue this strain-energy function is modified by a damage parameter. Herein the material parameters can be fitted independently of the damage parameters, a significant advantage relative to approaches based on continuum damage. The model is proposed in the most general framework able to describe damage in both the matrix and the fiber components individually. Specifications of the model are fit to experimental data assuming that damage accumulates (i) in the fibers only, (ii) in the matrix only and (iii) in both constituents. Such a fitting procedure allows a judgement of the quantitative fit of the model to the data in view of the number of model parameters employed.

Discontinuous softening is observed at all load levels and the pre-conditioning behavior of the tissue can also be described by the Mullins effect [80]. Hence, contrary to other damage functions introduced in the literature, see, for example, Balzani et al. [78] and Calvo et al. [63], we define no threshold value for the damage. Rather then setting an *a priori* threshold for tissue damage in the model, we seek to clarify what model values of damage describe pre-conditioning-like softening and what values describe acute tissue injury beyond the physiological load range.

In the following sections the constitutive model is presented and the experimental protocol and data analysis methods are explained. Results of the uniaxial extension tests, the data fitting and the histological examinations are presented and finally discussed.

2.2 Materials and Methods

2.2.1 Constitutive Modeling

Kinematics, Pseudo-Elastic Damage Model

With forethought to implementation into an FE code, a multiplicative decomposition of the deformation gradient $\mathbf{F} = (J^{1/3}\mathbf{I})\overline{\mathbf{F}}$ is considered, where $J = \det\mathbf{F} > 0$ is the determinant of the deformation gradient, the volume ratio, and $\mathbf{I}$ is the second-order unit tensor. The term $J^{1/3}\mathbf{I}$ represents the volumetric part, while $\overline{\mathbf{F}}$, with $\det\overline{\mathbf{F}} = 1$, is the isochoric part of the deformation gradient [81]. Consequently, $\mathbf{C} = \mathbf{F}^{\mathrm{T}}\mathbf{F}$ denotes the right Cauchy-Green tensor, and $\overline{\mathbf{C}} = \overline{\mathbf{F}}^{\mathrm{T}}\overline{\mathbf{F}}$ is the modified right Cauchy-Green tensor [25].

To consider isotropic damage in the sense of decoupled volumetric-isochoric response, according to the multiplicative split of the deformation gradient $\mathbf{F}$, we postulate a decoupled representation of the strain-energy function $\Psi(\mathbf{C},\eta)$, where $\eta \in]0,1]$ is a damage variable. Thus, by consideration of the pseudo-elastic damage model as introduced by Ogden and Roxburgh [48], we have

$$\Psi(J,\overline{\mathbf{C}},\eta) = \Psi_{\mathrm{vol}}(J) + \eta\,\overline{\Psi}^{0}(\overline{\mathbf{C}}) + \Phi(\eta), \tag{2.1}$$

where Ψ_{vol} is a strictly convex function (with the minimum at $J = 1$) which describes the volumetric elastic response, the second function $\overline{\Psi}^{0}$ denotes the isochoric strain energy of the undamaged material, which describes the isochoric elastic response so that the damage phenomenon affects only the isochoric part of the deformation ([45]); the superscript 0 denotes an undamaged material. We require that $\Psi_{\mathrm{vol}}(J) = 0$ and $\overline{\Psi}^{0}(\overline{\mathbf{C}}) = 0$ hold if and only if $J = 1$ and $\overline{\mathbf{C}} = \mathbf{I}$, respectively. The third function Φ in (5.1) denotes a (smooth) damage function. Note, that damage is only accumulated in the deviatoric part of the strain-energy function and that the material remains isochoric even if damage is induced.

By definition the damage variable η is set to 1 on the primary loading curve. The material behavior on this curve is then described by the strain-energy function such that $\Phi(1) = 0$ and $\Psi(\mathbf{C},1) = \Psi_{\mathrm{vol}}(J) + \overline{\Psi}^{0}(\overline{\mathbf{C}})$. In the case of subsequent unloading and reloading, i.e. when $\eta < 1$, the damage evolves with the deformation so that [48]

$$\frac{\partial\Psi}{\partial\eta} = \overline{\Psi}^{0}(\overline{\mathbf{C}}) + \Phi'(\eta) = 0, \tag{2.2}$$

where $\Phi'(\eta) = \partial\Phi(\eta)/\partial\eta$. Thus,

$$\overline{\Psi}^{0}(\overline{\mathbf{C}}) = -\Phi'(\eta) \tag{2.3}$$

implicitly defines the damage variable η in terms of the deformation. Ogden and Roxburgh [48] have chosen the damage function as

$$-\Phi'(\eta) = m\,\mathrm{erf}^{-1}[r(\eta-1)] + \overline{\Psi}^{\max}, \tag{2.4}$$

where $\mathrm{erf}^{-1}(\cdot)$ is the inverse of the error function $\mathrm{erf}(\cdot)$ and $\overline{\Psi}^{\max}$ denotes the maximum of the strain energy obtained in the deformation history. Some algebraic manipulation, using (2.3), gives

$$\eta = 1 - \frac{1}{r}\mathrm{erf}\left[\frac{1}{m}(\overline{\Psi}^{\max} - \overline{\Psi}^{0})\right], \tag{2.5}$$

where $r > 1$ characterizes the maximum material damage that can be induced under loading, and $m > 0$ determines the dependence of the damage on the deformation. Small values of m indicate that significant damage already occurs at small strains, whereas for larger values of m damage will progress more slowly. To characterize the damage induced to the material, the minimum value $\eta^{\min}$ of the damage function is determined as

$$\eta^{\min} = 1 - \frac{1}{r}\mathrm{erf}\left(\frac{1}{m}\overline{\Psi}^{\max}\right). \tag{2.6}$$

Other constitutive equations for the softening function have been proposed by, for example, Beatty and Krishnaswamy [82] and Elías-Zúñuiga [83].

Given the strain-energy function (5.1), the second Piola-Kirchhoff stress tensor is calculated as $\mathbf{S} = 2\partial\Psi/\partial\mathbf{C} = \mathbf{S}_{\mathrm{vol}} + \overline{\mathbf{S}}$. Hence, the volumetric part of $\mathbf{S}$ is given by $\mathbf{S}_{\mathrm{vol}} = 2\partial\Psi_{\mathrm{vol}}(J)/\partial\mathbf{C}$, while the isochoric part $\overline{\mathbf{S}}$ of the second Piola-Kirchhoff stress tensor is determined by using (2.3), i.e.

$$\overline{\mathbf{S}} = 2\left[\eta\frac{\partial\overline{\Psi}^{0}(\overline{\mathbf{C}})}{\partial\mathbf{C}} + \overline{\Psi}^{0}(\overline{\mathbf{C}})\frac{\partial\eta}{\partial\mathbf{C}} + \Phi'\frac{\partial\eta}{\partial\mathbf{C}}\right] = \eta\overline{\mathbf{S}}^{0}, \qquad \overline{\mathbf{S}}^{0} = 2\frac{\partial\overline{\Psi}^{0}(\overline{\mathbf{C}})}{\partial\mathbf{C}}, \tag{2.7}$$

where $\overline{\mathbf{S}}^{0}$ is the isochoric second Piola-Kirchhoff stress tensor related to the undamaged material.

Damage Model for Arterial Tissue

The individual layers of the artery are modeled as fiber-reinforced composites with an additive decomposition of the strain-energy function $\overline{\Psi}^{0}$ into an energy stored in the non-collagenous matrix, say $\overline{\Psi}^{0}_{\mathrm{m}}$, and an energy stored in the collagen fibers, say $\overline{\Psi}^{0}_{\mathrm{f}}$. Hence (cf. [84]),

$$\overline{\Psi}^{0} = \overline{\Psi}^{0}_{\mathrm{m}} + \overline{\Psi}^{0}_{\mathrm{f}}. \tag{2.8}$$

The non-collagenous matrix is assumed to be isotropic and modeled as a neo-Hookean material, i.e.

$$\overline{\Psi}^{0}_{\mathrm{m}} = \frac{\mu}{2}(\bar{I}_1 - 3), \tag{2.9}$$

where $\mu > 0$ corresponds to the shear modulus of the material in the reference configuration, and $\bar{I}_1 = \mathrm{tr}(\overline{\mathbf{C}})$ is the first strain invariant of the modified right Cauchy-Green tensor $\overline{\mathbf{C}}$.

We assume here two collagen fiber families for all layers (as, for example, shown in Schriefl et al. [40] and, therefore, we use a two-fiber family model according to Holzapfel et al. [7] and Gasser et al. [39]. The related (anisotropic) strain-energy function may be written as

$$\overline{\Psi}^0_{\mathrm{f},i} = \frac{k_1}{2k_2}[e^{k_2(\overline{I}^\star_i-1)^2}-1], \qquad \overline{I}^\star_i = \kappa\overline{I}_1 + (1-3\kappa)\overline{I}_i, \qquad i=4,6, \tag{2.10}$$

where $i=4$ relates to one fiber family and $i=6$ to the other. The pseudo-invariants $\overline{I}_4 = \overline{\mathbf{C}} : \mathbf{M}\otimes\mathbf{M}$ and $\overline{I}_6 = \overline{\mathbf{C}} : \mathbf{M}'\otimes\mathbf{M}'$ correspond to the square of the stretches of the fibers in the fiber directions. The vectors $\mathbf{M}$ and $\mathbf{M}'$ denote the directions of the collagen fibers in the reference configuration. The fibers are symmetrically oriented with respect to the circumferential direction of the artery, and thus both $\mathbf{M}$ and $\mathbf{M}'$ are uniquely defined by the structural parameter φ, which defines the angle between the circumferential direction of the artery and the fiber direction. The dispersion parameter $\kappa \in [0, 1/3]$ describes radial symmetry of the dispersion about the fiber direction. Furthermore, we have the stress-like parameter $k_1 > 0$ and the dimensionless parameter $k_2 > 0$. In the proposed model the anisotropic strain-energy function $(2.10)_1$ only contributes to Ψ when $\overline{I}^\star_4 > 1$ or $\overline{I}^\star_6 > 1$. If one or more of these conditions is not satisfied then the relevant part of $(2.10)_1$ is omitted.

For the fiber contribution an interesting limiting case exists, namely for $k_2 \to 0$; then the corresponding strain-energy function reads

$$\overline{\Psi}^0_{\mathrm{f},i} = \frac{k_1}{2}(\overline{I}^\star_i - 1)^2, \qquad i=4,6, \tag{2.11}$$

such that the stiffening of the collagen fibers is described by a quadratic function rather than an exponential function.

We propose a general framework for modeling discontinuous damage in soft biological tissues by employing one damage function $\Phi_{\mathrm{m}}(\eta_{\mathrm{m}})$ for the non-collagenous matrix, with the damage variable η_{m} relating to the matrix, and two damage functions $\Phi_{\mathrm{f},4}(\eta_{\mathrm{f},4})$ and $\Phi_{\mathrm{f},6}(\eta_{\mathrm{f},6})$ for the two families of fibers, with the two damage variables $\eta_{\mathrm{f},4}$ and $\eta_{\mathrm{f},6}$ describing damage in the two families of collagen fibers separately. Hence, we are able to replace the strain-energy function $\Psi(\mathbf{C},\eta)$ in (5.1) by

$$\Psi(\mathbf{C},\eta_{\mathrm{m}},\eta_{\mathrm{f},4},\eta_{\mathrm{f},6}) = \Psi_{\mathrm{vol}} + \eta_{\mathrm{m}}\overline{\Psi}^0_{\mathrm{m}}(\overline{\mathbf{C}}) + \Phi_{\mathrm{m}}(\eta_{\mathrm{m}}) + \sum_{i=4,6}[\eta_{\mathrm{f},i}\overline{\Psi}^0_{\mathrm{f},i}(\overline{\mathbf{C}}) + \Phi_{\mathrm{f},i}(\eta_{\mathrm{f},i})], \tag{2.12}$$

where the energies $\overline{\Psi}^0_{\mathrm{m}}$ and $\overline{\Psi}^0_{\mathrm{f},i}$ are specified in (2.9) and (2.10), respectively.

In (2.12), the evolution of the damage variable η_{m} in the non-collagenous matrix is characterized by two parameters (r_{m}, m_{m}), cf. (5.2), while damage in both families of collagen fibers is characterized, in general, by four variables $(r_{\mathrm{f},4}, m_{\mathrm{f},4}, r_{\mathrm{f},6}, m_{\mathrm{f},6})$. The final form of

Donor	I	II	III	IV	V	VI	VII	VIII	IX	X	XI	XII	XIII	XIV	XV	XVI	XVII
Age [yrs]	55	48	47	53	61	79	61	69	77	68	53	44	48	68	74	62	69
Gender	F	F	F	M	F	M	M	F	F	M	M	M	M	F	F	F	M

Table 2.1: Overview over age and gender of the donors; M: male, F: female.

(2.12) remains to be specified for aortic arterial tissue via appropriate mechanical tests, where damage may accumulate only in the matrix material, or only in the collagen fiber fabric or in both constituents simultaneously.

Finally, by analogy with the procedure which led to (5.7), we determine $\overline{\mathbf{S}}$ from (2.12). Thus,

$$\overline{\mathbf{S}} = \eta_{\mathrm{m}}\overline{\mathbf{S}}^0_{\mathrm{m}} + \sum_{i=4,6} \eta_{\mathrm{f},i}\overline{\mathbf{S}}^0_{\mathrm{f},i}, \qquad \overline{\mathbf{S}}^0_{\mathrm{m}} = 2\frac{\partial \overline{\Psi}^0_{\mathrm{m}}}{\partial \mathbf{C}}, \qquad \overline{\mathbf{S}}^0_{\mathrm{f},i} = 2\frac{\partial \overline{\Psi}^0_{\mathrm{f},i}}{\partial \mathbf{C}}, \quad i = 4,6. \tag{2.13}$$

where $\overline{\mathbf{S}}^0_{\mathrm{m}}$ and $\overline{\mathbf{S}}^0_{\mathrm{f},i}$ are second Piola-Kirchhoff stress tensors related to the undamaged matrix and fiber fabric, respectively. With the two strain-energy functions (2.9) and (2.10) the two stress tensors can be specified. From (2.13) we obtain

$$\overline{\mathbf{S}}^0_{\mathrm{m}} = 2\frac{\partial \overline{\Psi}^0_{\mathrm{m}}}{\partial \overline{I}_1}\frac{\partial \overline{I}_1}{\partial \mathbf{C}} = \mu\frac{\partial \overline{I}_1}{\partial \mathbf{C}}, \tag{2.14}$$

$$\overline{\mathbf{S}}^0_{\mathrm{f},i} = 2\frac{\partial \overline{\Psi}^0_{\mathrm{f},i}}{\partial \overline{I}^{\star}_i}\frac{\partial \overline{I}^{\star}_i}{\partial \mathbf{C}} = 2k_1(\overline{I}^{\star}_i - 1)e^{k_2(\overline{I}^{\star}_i - 1)^2}\frac{\partial \overline{I}^{\star}_i}{\partial \mathbf{C}}, \qquad i = 4,6, \tag{2.15}$$

where it is straightforward to specify the kinematic relations $\partial \overline{I}_1/\partial \mathbf{C}$ and $\partial \overline{I}^{\star}_i/\partial \mathbf{C}$. The related Cauchy stress tensor $\sigma = J^{-1}\mathbf{F}\mathbf{S}\mathbf{F}^{\mathrm{T}}$ is obtained by a standard push-forward operation.

2.2.2 Experimental Protocol

Specimen Preparation

For the present study 16 thoracic and abdominal aortas with non-atherosclerotic intimal thickening were harvested within 24 hrs of death and stored in physiological solution at 4°C. Table 2.1 provides an overview of age and gender of the individual donors. Out of this pool of aortas, 14 thoracic aortas (60 ± 12 yrs, mean $\pm$ SD) and 9 abdominal aortas (61 ± 11 yrs) were tested, and the rest were omitted due to calcification of the tissue. All tests, performed with the aim to obtain information of the mechanical aortic behavior in the supra-physiological deformation and loading domains, were conducted within 48 hrs after removal from the body. The use of autopsy material from human subjects was approved by the Ethics Committee of the Medical University of Graz.

In the regions without visible atherosclerosis, dog-bone specimens were cut from the arterial tissue using a punching tool (length 37.3 mm; width at the clamping region 8.7 mm). The gauge section had a width of 4 mm and a length of 10 mm. The initial thickness of the specimens was measured with a videoextensometer (ME 46-350, Messphysik, Fürstenfeld, Austria), where the average of four measurements at evenly distributed locations was taken to determine one value for the mean thickness. Furthermore, two black markers were glued onto the specimen surface (with distance of about 5 mm) and tracked with a videoextensometer so that the local stretch could be calculated.

For the layer-separated specimens, intima, media and adventitia were separated manually. During separation of the individual layers, the dissection was not always perfect, but only (very) minor fractions of the media were found attached to the adventitia (cf. [85]). It was assumed here that the effect of imperfect layer separation on the mechanical behavior of the individual layers can be neglected.

Uniaxial Tension Test

Mechanical tests of tissue strips taken along the axial and circumferential directions of the aorta were conducted with a uniaxial testing machine (μ-Strain ME 30-1, Messphysik, Fürstenfeld, Austria), inside a tissue bath with physiological solution at 37°C. A force driven protocol was employed, where the forces were calculated *a priori* such that tissue loading resulted in a first Piola-Kirchhoff stress, i.e. force related to the area of the reference configuration, of 100, 300, 600, 900 kPa for the adventitia, and 50, 100, 300, 500 kPa for all other specimens. The adventitia was loaded with a different protocol because of its relatively high strength so that a similar number of load cycles were tested for each layer. Three cycles were executed for each load step in order to observe discontinuous softening of the tissue that was evident in the first cycle of a load step, and to simultaneously investigate the possibility of continuous tissue softening, that would be evident in subsequent cycles of the same load. The specimens were loaded quasi-statically at a rate of 5 mm/min.

Data Analysis

To evaluate the experimental data, and to specify and fit the proposed constitutive damage model, the Cauchy stress σ and the stretch λ in the loading direction were computed. The Cauchy stress was calculated as $\sigma = f/(tw)$, where f is the measured force, t is the specimen thickness and w is the width of the specimen in the current configuration. By introducing the specimen length l in the current configuration, we may write $twl = TWL$ due to the assumption of incompressibility of the tissue (capital letters denote related values in the undeformed configuration). The Cauchy stress can then be rewritten as

$$\sigma = \frac{f}{TW}\lambda, \tag{2.16}$$

where $\lambda = l/L$ denotes the stretch in the loading direction.

We assume here that the evolution of damage in both families of collagen fibers is the same so that damage is characterized by the two variables $r_\mathrm{f} = r_{\mathrm{f},4} = r_{\mathrm{f},6}$ and $m_\mathrm{f} = m_{\mathrm{f},4} = m_{\mathrm{f},6}$. The constitutive parameters $\mathbf{x} = [\mu, k_1, k_2, \varphi, \kappa, r_\mathrm{f}, m_\mathrm{f}]$ was performed using a nonlinear least-squares trust region algorithm implemented in the MATLAB (2009b, The MathWorks, Inc., Massachusetts, United States). First the Cauchy stress in the loading direction (2.16) is determined. Next, the lateral and the through-the-thickness stretches are calculated using the incompressibility condition and an additional constraint that the stress in the lateral direction equals zero. The parameter optimization was performed with these stresses and stretches minimizing the objective function

$$\chi = \sum_{i=1}^{n} [\sigma_i^{\mathrm{exp}}(\mathbf{C}) - \sigma_i^{\mathrm{mod}}(\mathbf{C}, \mathbf{x})]^2, \tag{2.17}$$

where n is the number of considered data points σ_i^{exp} are the Cauchy stresses determined experimentally and σ_i^{mod} are the corresponding values predicted by the strain-energy function Ψ for both the circumferential and the axial direction.

With the obtained constitutive parameters the lateral and through-the-thickness stretches were updated and the fitting was repeated until the solution converged. The material parameters were fit to the primary load path, and then the damage parameters were determined using the entire loading history. For the material parameters associated with the anisotropic part of the strain-energy function, it is assumed that the fibers are not under compression during the experiment and only results with $\bar{I}_4^* \geq 1$ were considered. Different sets of initially-guessed material parameters were tested as these may lead to different fitting results [86], and in all physically-reasonable cases the resulting material parameters were nearly identical. The coefficient of determination R^2 was used to evaluate the goodness of fit.

Three different cases were tested in fitting the damage parameters to specify an accurate and efficient damage model for aortic tissues. First, the strain-energy function (2.12), which considers damage accumulation in both the non-collagenous matrix and the collagen fabric, was fit to the experimental data (Case I). Second, a constitutive model considering damage accumulation only in the collagen fibers ($\eta_\mathrm{m} = 1$ and $\Phi_\mathrm{m} = 0$) was fit for comparison (Case II). Finally, for the sake of completeness, a model considering damage accumulation only in the matrix material, i.e. (2.12) with $\eta_{\mathrm{f},4} = \eta_{\mathrm{f},6} = 1$ and $\Phi_{\mathrm{f},4} = \Phi_{\mathrm{f},6} = 0$, was also fit for comparison (Case III).

Statistical Analysis

Values for the material parameters, which best characterize the entire specimen populations, are reported as the medians and interquartile ranges, as not all parameters show a normal distribution and outliers can affect the mean and standard deviation severely. A correlation between the material parameters and age is investigated with the correlation

coefficient r_s and the significance of the correlation is tested using the Fisher transformation. The Wilcoxon rank-sum test is used to examine the significance of differences in the parameters determined for abdominal and thoracic aortas, and to access the influence of gender on the fit parameters taking into account the Bonferroni-Holm correction. For all tests $p < 0.05$ was assumed to be significant.

Histology

Histological specimens were prepared to gain insight on the qualitative structural changes of collagen at various levels of stretch. To this end, axial and circumferential specimens of the same intact thoracic aorta (Donor XIII) were stretched in the circumferential direction to $\lambda_c = 1.05, 1.35, 1.50$, and in the axial direction to $\lambda_a = 1.05, 1.20$. The different stretches in the two directions is a result of the anisotropy of the tissue. Specimens were mounted in a custom made frame at the specified stretches, fixed in a 4% buffered formaldehyde solution (pH 7.4) and prepared for histology. Two types of specimen cross-sections were investigated: (i) cuts in the plane of the tissue, and (ii) cuts normal to this plane along the loading direction. Picrosirius red stains were used to visualize collagen using its birefringent properties under polarized light.

2.3 Results and Discussion

2.3.1 Model Specification

The pseudo-elastic damage models related to Case I and Case II give similarly good results in terms of fitting the stress-stretch data, as quantified by the R^2-values (both > 0.9 in most cases). The model related to Case III, considering damage accumulation only in the non-collagenous matrix, gives relatively poor results wherein the hysteresis in the data is not reproduced. Therefore, the model describing Case III was dismissed from further consideration.

Comparing the models of Cases I and II more closely, for the majority of the stress-stretch data the two models generate very similar damage parameters r_f and m_f from the fitting process. In many of these fits, the parameters r_m and m_m are very large such that η_m remains approximately one over the whole load history, and, as a consequence, the inclusion of the damage variable η_m for the non-collagenous matrix does not provide any additional accuracy to the fit. In most of the remaining fits the parameter r_m is nearly zero at stretches less than 1.01 such that the minimum of the damage function is already reached, i.e. complete damage occurs very early in the load history.

A comparison of a representative model fit is shown in Fig. 2.1. Therein, experimental data from the media of the thoracic aorta of Donor II is compared with the corresponding model, i.e. Case I, Fig. 2.1(a), and Case II, Fig. 2.1(c), where the goodness of fit is the same for both cases ($R^2 = 0.98$). However, the damage evolution for Case I, Fig. 2.1(b), shows that the minimum damage variable $\eta_m^{\min}$ for the non-collagenous matrix material remains

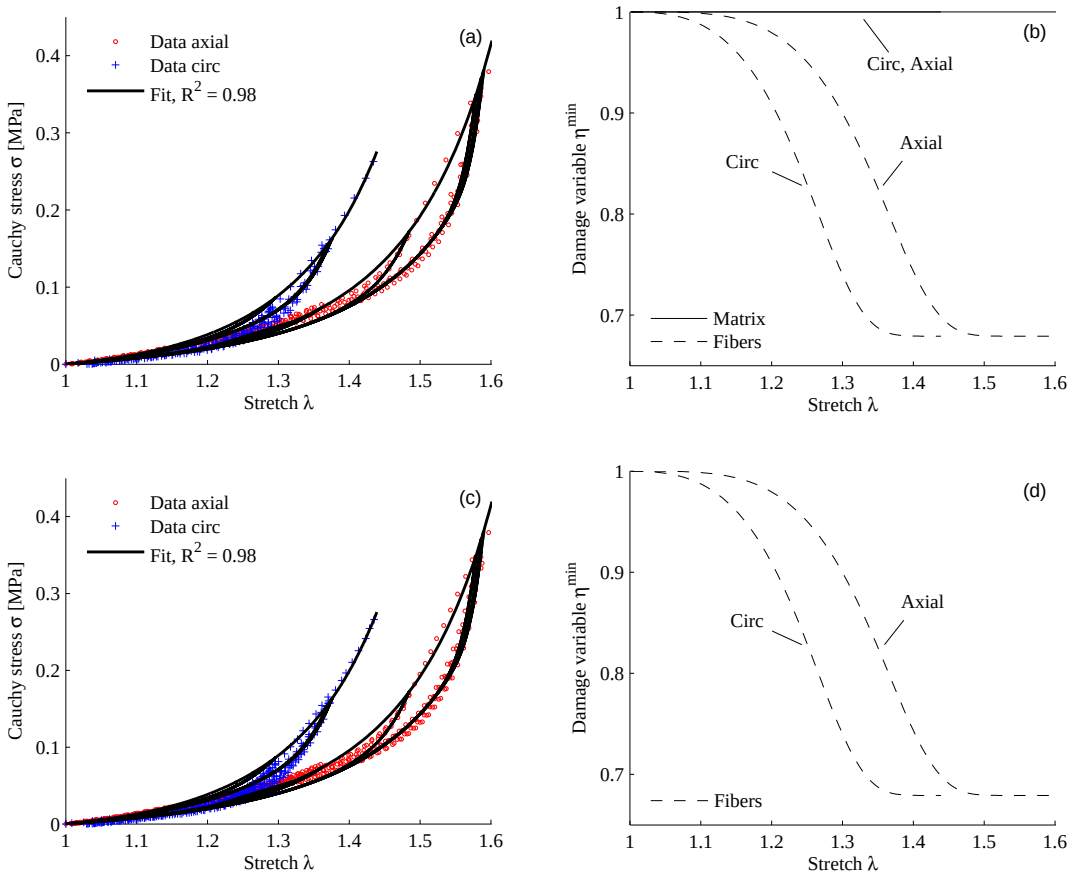

Figure 2.1: Representative comparison of Case I (damage accumulation in both matrix and collagen fibers) – top row, and Case II (damage only in collagen fibers) – bottom row, for the media of Donor II. Cauchy stress σ versus stretch λ (a) and (c); experimental data ($\circ$ and $+$) compared with constitutive model (solid curve). Evolution of the minimum damage variable $\eta^{\min}$ with stretch λ (b) and (d); $R^2 = 0.98$ for both cases.

one for the entire loading range, hence the matrix material is considered to be undamaged. The damage evolution in the fibers is similar for the Cases I and II, see Fig. 2.1(d).

The fitting of other specimens with Case I sometimes generates complete damage of the non-collagenous matrix at stretches far below the physiological loading range (results not shown). However, this is not meaningful from a physical point of view.

Both Cases I and II generate similar data fits, and the inclusion of damage accumulation in the matrix material results in either no damage or not physically relevant damage. As a consequence we propose that tissue softening is primarily related to collagen fibers and we subsequently focus only on the model of Case II.

2.3.2 Material and Damage Parameters

The representative stress-stretch responses, as shown in Fig. 2.1, demonstrate the anisotropic behavior of the aortic tissue and a hysteresis during unloading from the primary load path. In all cases the proposed constitutive model is able to reproduce the experimentally determined stress-stretch data in an accurate manner.

The median thicknesses of the intima, media and adventitia are 0.48 mm, 1.18 mm and 0.93 mm for the thoracic aorta and 0.68 mm, 0.94 mm and 1.07 mm for the abdominal aorta, respectively. The constitutive parameters μ, k_1, k_2, φ, κ, r_f and m_f together with the coefficient of determination R^2, the median, the first quartile Q_1 and the third quartile Q_3, for the intima, media and the adventitia of the human thoracic aorta are summarized in Table 2.2. The same model parameters are presented in Table 2.3 for the layers of the abdominal aortas and in Table 2.4 for the intact aortic wall. It is important to note that the constitutive parameter k_2 in the intima of the abdominal aorta equals zero in the majority of the cases (cf. (2.11)), in contrast to all other layers. Intimal thickening is more pronounced in the abdominal aorta than in the thoracic aorta, see [87] and [57], so that the remodeling process might result in the change of the material response of the intima. A comparison of the median damage parameters r_f for the layer-separated tests suggests that the amount of damage accumulated is highest in the intima, as we obtain a value of 1 for both thoracic and abdominal aortas. The median damage parameters m_f are in the same range for all layers. Due to the earlier exponential stiffening of the intima relative to the other layers, the intima accumulates the most damage at a certain stretch (compare with Figs. 2.2(b) and (d)). Nonetheless, this does not mean that the most damage will be accumulated in the intima for loading the intact aortic wall due to compressive residual stresses as reported for the intima, for example, in [24].

In most cases the R^2-value is higher than 0.9. The angle φ for the intima varies between 38.1° and 54.2° for the thoracic aorta, and between 35.3° and 48.9° for the abdominal aorta. These results indicate that the fibers in the intima are in some specimens more aligned in the axial direction and in some specimens more in the circumferential direction. It is important to note that non-atherosclerotic intimal thickening increases with age, wherein collagen fibers are deposited in the intimal layer [57]. Hence, the collagen orientations may strongly depend on age. The median values for the Cauchy stress-stretch response and the related damage evolution are illustrated in Figs. 2.2(a), (b) for the thoracic aorta and in Figs. 2.2(c), (d) for the abdominal aorta. The qualitative mechanical stress-stretch response of the three tissue layers is similar to that reported for carotid arteries [38]. The circumferential specimens of the media are seen to stiffen at lower applied stretches in comparison to their respective orthogonal specimens, see Figs. 2.2(a) and (c). These results are in agreement with the obtained fiber alignments which are more circumferential in the medial layer, see the φ-values in the Table 2.2 and the values obtained from polarized microscopy recently reported by Schriefl et al. [40]. However, the fit angles provided here are larger for the media, as compared against the measured values. This may be

Donor	μ [MPa]	k_1 [MPa]	k_2 [-]	φ[°]	κ [-]	r_f [-]	m_f [-]	R^2
Intima								
I	0.021	4.90	15.52	40.5	0.20	1.95	0.007	0.95
II	0.052	11.64	0.0	44.5	0.28	1.93	0.010	0.91
III	0.034	1.45	7.36	44.8	0.12	1.00	0.017	0.96
IV	0.020	0.26	17.06	54.2	0.22	2.81	0.015	0.99
V	0.019	4.84	53.04	46.1	0.18	1.00	0.017	0.99
VI	0.091	20.07	0.0	44.4	0.22	1.00	0.015	0.99
VII	0.031	2.54	11.31	47.0	0.13	1.00	0.021	0.99
VIII	0.046	6.28	10.76	47.8	0.20	1.00	0.014	0.98
IX	0.043	3.39	15.34	42.8	0.20	2.84	0.009	1.00
X	0.055	6.27	30.23	49.0	0.15	1.00	0.011	0.96
XI	0.020	1.07	28.11	47.0	0.32	1.00	0.017	0.91
XII	0.035	3.85	3.37	48.1	0.17	1.00	0.018	0.98
XIII	0.041	1.73	3.35	51.2	0.10	1.36	0.008	0.92
XIV	0.029	6.33	36.52	38.1	0.22	1.00	0.011	0.97
Median	0.034	4.34	13.32	46.5	0.20	1.00	0.014	0.97
$[Q_1, Q_3]$	$[0.023, 0.045]$	$[1.93, 6.28]$	$[4.37, 25.35]$	$[44.4, 48.0]$	$[0.15, 0.22]$	$[1.00, 1.78]$	$[0.010, 0.017]$	$[0.95, 0.99]$
Media								
I	0.030	0.12	7.62	44.6	0.02	3.10	0.002	0.98
II	0.025	0.25	9.45	36.9	0.27	3.12	0.002	0.98
III	0.021	0.02	15.88	42.2	0.07	2.35	0.007	0.99
IV	0.023	0.06	3.85	45.3	0.02	1.53	0.013	0.99
V	0.021	0.12	1.75	43.2	0.02	1.78	0.005	0.90
VI	0.030	0.43	43.49	35.8	0.30	2.13	0.008	0.98
VII	0.034	0.15	17.07	39.3	0.22	2.11	0.014	0.99
VIII	0.022	0.22	18.64	37.7	0.27	1.77	0.010	0.98
IX	0.032	0.29	18.26	36.4	0.20	1.17	0.025	0.99
X	0.038	0.12	4.47	39.1	0.15	1.48	0.016	0.99
XI	0.021	0.14	6.74	37.3	0.27	1.96	0.009	0.99
XII	0.043	0.12	15.24	46.5	0.05	2.68	0.003	1.00
XIII	0.027	0.15	1.79	36.0	0.23	1.77	0.012	0.99
XIV	0.029	0.53	14.35	35.1	0.27	1.00	0.024	0.93
Median	0.028	0.14	11.90	38.4	0.21	1.87	0.009	0.99
$[Q_1, Q_3]$	$[0.022, 0.032]$	$[0.12, 0.24]$	$[5.04, 16.77]$	$[36.54, 42.97]$	$[0.05, 0.27]$	$[1.59, 2.29]$	$[0.006, 0.014]$	$[0.98, 0.99]$
Adventitia								
I	0.020	0.39	9.03	53.7	0.27	2.21	0.006	0.93
II	0.017	0.26	7.72	53.0	0.27	1.53	0.011	0.91
III	0.017	0.29	4.11	51.0	0.02	1.01	0.023	0.88
IV	0.014	0.22	9.93	54.1	0.23	2.40	0.006	0.93
V	0.008	0.79	1.09	51.6	0.03	1.00	0.029	0.93
VI	0.032	0.84	22.47	55.9	0.32	1.00	0.051	0.87
VII	0.024	0.40	11.01	54.7	0.25	1.00	0.224	0.91
VIII	0.032	1.58	2.04	48.7	0.05	1.20	0.022	0.91
IX	0.052	1.29	1.25	48.5	0.10	1.00	0.022	0.92
X	0.038	0.88	5.86	47.4	0.03	1.10	0.032	0.89
XI	0.015	0.21	4.67	34.6	0.28	1.40	0.021	0.96
XII	0.017	0.66	4.77	53.4	0.22	1.22	0.027	0.83
XIII	0.019	0.23	9.55	53.9	0.30	2.39	0.009	0.98
XIV	0.022	0.28	12.74	42.7	0.12	1.00	0.010	0.96
Median	0.020	0.39	6.79	52.3	0.23	1.15	0.022	0.92
$[Q_1, Q_3]$	$[0.017, 0.030]$	$[0.27, 0.83]$	$[4.25, 9.83]$	$[48.5, 53.9]$	$[0.06, 0.27]$	$[1.00, 1.50]$	$[0.010, 0.028]$	$[0.90, 0.93]$

Table 2.2: Constitutive parameters for the intima, media and the adventitia of the human thoracic aorta; together with the coefficient of determination R^2, the median, the first quartile Q_1 and the third quartile Q_3.

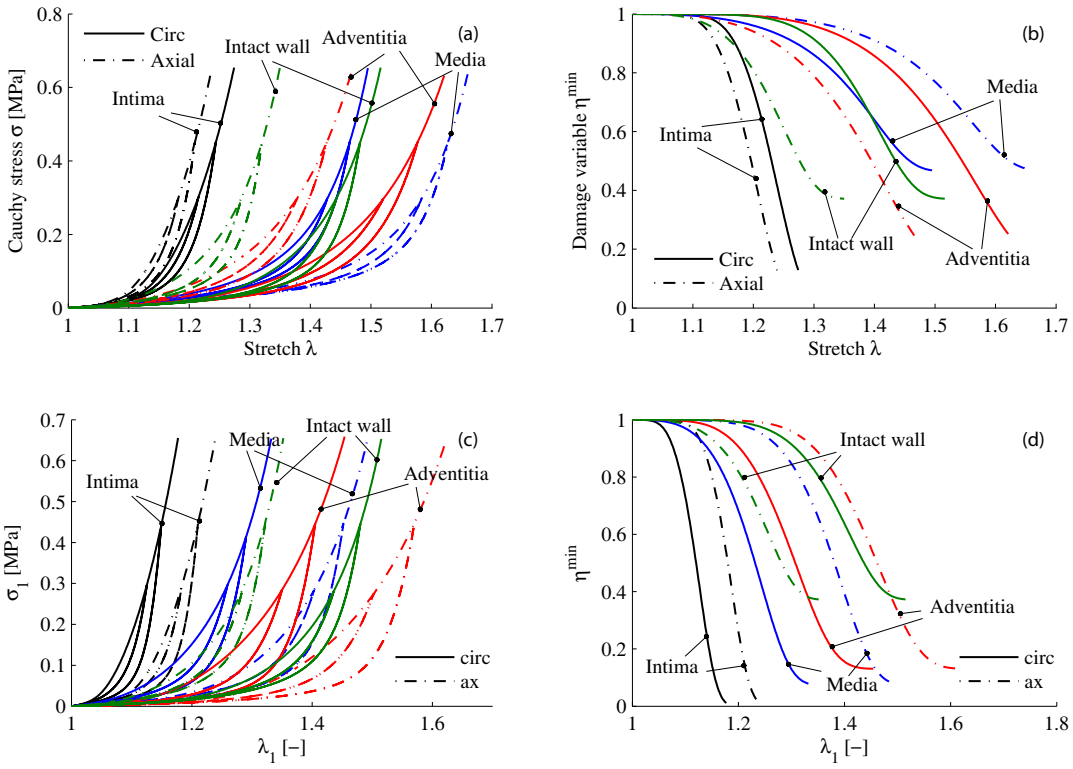

Figure 2.2: Cauchy stress-stretch response (a) and (c), and damage evolution (b) and (d) for the thoracic aorta (top row) and the abdominal aorta (bottom row) plotted with the median parameter values from Tables 2.2 – 2.4.

due to the fact that the material model used does not take crimping of the fibers into account. The un-crimping of fibers during stretching, as illustrated in Fig. 2.5, might change the angular alignment of the fibers.

2.3.3 Effect of Pre-Conditioning

Arterial tissues need to be pre-conditioned prior to recording data used for fitting the material response to an elastic constitutive equation. In this study, however, the material is modeled using a pseudo-elastic framework which can describe tissue softening after the initial load cycle. Hence, the pre-conditioning behavior is captured by the presented model which allows us to evaluate the effect of pre-conditioning on the material parameters.

As a representative example to evaluate the effect of aortic tissue pre-conditioning on the constitutive parameters, we use the constitutive parameters of Donor VII. The analytical solution for unloading and reloading the tissue to 150 kPa (cf. [38] for pre-conditioning of arterial tissue) was obtained. The reloading path was then fit by using the elastic part of the material model.

Donor	μ [MPa]	k_1 [MPa]	k_2 [-]	φ[°]	κ [-]	r_f [-]	m_f [-]	R^2
Intima								
I	0.044	5.51	0.00	35.3	0.22	2.27	0.008	0.92
V	0.033	10.14	0.00	46.3	0.27	2.28	0.031	0.95
VIII	0.068	25.91	67.45	37.5	0.23	11.59	0.002	0.92
IX	0.105	30.90	16.24	47.6	0.28	1.00	0.025	0.99
XII	0.138	22.98	0.00	40.5	0.25	1.00	0.016	0.98
XIII	0.005	0.98	49.78	47.6	0.17	1.00	0.003	0.98
XIV	0.041	10.15	0.00	36.1	0.28	1.00	0.052	0.97
XVI	0.028	5.11	0.00	48.9	0.25	1.00	0.046	0.99
XVII	0.076	5.14	103.31	38.5	0.25	1.00	0.006	0.96
Median	0.044	10.14	0.00	40.5	0.25	1.00	0.016	0.97
$[Q_1, Q_3]$	$[0.033, 0.076]$	$[5.14, 22.98]$	$[0.00, 49.78]$	$[37.5, 47.6]$	$[0.23, 0.27]$	$[1.00, 2.27]$	$[0.006, 0.031]$	$[0.95, 0.98]$
Media								
I	0.036	0.52	19.09	42.6	0.05	1.01	0.010	0.84
V	0.033	1.42	29.26	43.9	0.10	1.00	0.008	0.96
VIII	0.032	1.01	0.00	35.2	0.18	1.43	0.020	0.95
IX	0.028	0.92	10.33	35.0	0.28	1.31	0.008	0.98
XII	0.021	0.62	35.30	39.1	0.28	1.00	0.021	0.97
XIII	0.019	0.15	6.52	36.5	0.28	2.34	0.010	0.99
XIV	0.023	1.09	18.91	35.5	0.22	1.00	0.013	0.93
XVI	0.028	0.81	0.08	48.7	0.08	1.08	0.014	0.98
XVII	0.017	0.19	12.42	44.16	0.12	1.71	0.001	0.99
Median	0.028	0.81	12.42	39.1	0.18	1.07	0.010	0.97
$[Q_1, Q_3]$	$[0.021, 0.032]$	$[0.51, 1.01]$	$[6.52, 19.09]$	$[35.5, 43.9]$	$[0.10, 0.28]$	$[1.00, 1.42]$	$[0.008, 0.014]$	$[0.95, 0.98]$
Adventitia								
I	0.008	1.06	1.09	47.0	0.10	1.30	0.018	0.87
V	0.005	0.38	5.55	36.3	0.12	1.41	0.006	0.91
VIII	0.010	0.49	3.35	36.1	0.27	1.15	0.009	0.94
IX	0.016	0.44	3.41	45.9	0.12	1.00	0.008	0.95
XII	0.008	1.06	1.09	47.0	0.10	1.30	0.018	0.87
XIII	0.010	0.30	6.31	51.2	0.30	1.79	0.010	0.93
XIV	0.003	0.20	1.88	36.1	0.02	1.00	0.019	0.92
XVI	0.005	0.51	0.43	51.7	0.02	1.49	0.013	0.89
XVII	0.011	0.12	4.73	40.6	0.12	1	0.005	0.94
Median	0.010	0.38	3.35	40.59	0.11	1.15	0.010	0.92
$[Q_1, Q_3]$	$[0.005, 0.010]$	$[0.28, 0.49]$	$[1.88, 4.73]$	$[36.3, 47.0]$	$[0.03, 0.12]$	$[1.00, 1.41]$	$[0.008, 0.018]$	$[0.89, 0.94]$

Table 2.3: Constitutive parameters for the intima, media and the adventitia of the human abdominal aorta; together with the coefficient of determination R^2, the median, the first quartile Q_1 and the third quartile Q_3.

The material parameters describing the elastic response for both the non pre-conditioned and the pre-conditioned tissue layers are summarized in Table 2.5. Note that the constitutive parameters μ and k_1 have the tendency to be slightly lower for the pre-conditioned material, whereas the parameter k_2 is significantly higher. The consequences of these differences on the stress-stretch response is illustrated for the media in Fig. 2.3, clearly showing that exponential stiffening is greater for the pre-conditioned material. In the supra-physiological loading range the *in vivo* material is not pre-conditioned, which is in contrast to the physiological loading range. Therefore, the material behavior follows the primary loading curve. If this is modeled with the (high) k_2 value obtained from the pre-conditioning tests, the stresses in the supra-physiological loading range are overestimated due to incorrect extrapolation of the stress-strain response. Hence, material tests with

Donor	μ [MPa]	k_1 [MPa]	k_2 [-]	φ[°]	κ [-]	r_f [-]	m_f [-]	R^2
Thoracic aorta								
I	0.007	0.30	1.81	51.4	0.08	1.58	0.004	0.93
II	0.017	0.25	16.88	54.2	0.25	3.32	0.002	0.96
III	0.016	0.14	9.12	54.1	0.30	1.41	0.011	0.97
VI	0.015	0.91	71.80	38.6	0.32	1.00	0.026	0.98
VII	0.033	1.03	36.30	48.5	0.08	1.60	0.002	0.97
VIII	0.014	0.89	17.64	40.2	0.12	1.26	0.005	0.85
IX	0.022	1.07	34.29	53.7	0.28	1.84	0.008	0.98
X	0.019	1.80	1.74	51.1	0.08	1.22	0.012	0.98
XI	0.015	0.20	6.92	53.9	0.28	1.82	0.010	0.97
XII	0.018	0.56	15.55	49.4	0.00	1.74	0.009	0.94
XIII	0.010	0.18	2.42	50.9	0.00	1.88	0.008	0.99
XIV	0.027	0.56	239.02	41.9	0.27	1.00	0.012	0.96
Median	0.017	0.56	16.21	51.0	0.18	1.59	0.008	0.97
$[Q_1, Q_3]$	$[0.014, 0.019]$	$[0.24, 0.94]$	$[5.79, 34.79]$	$[46.8, 53.8]$	$[0.08, 0.28]$	$[1.25, 1.83]$	$[0.004, 0.011]$	$[0.95, 0.98]$
Abdominal aorta								
I	0.014	2.87	17.26	36.0	0.25	1.86	0.005	0.99
V	0.047	14.98	0.00	40.4	0.27	1.00	0.025	0.99
VIII	0.164	36.77	149.44	41.0	0.25	1.00	0.017	0.98
IX	0.012	9.03	0.00	34.7	0.20	3.83	0.001	0.83
XII	0.040	5.43	68.87	41.4	0.18	1.00	0.013	0.99
XIII	0.009	0.46	20.24	54.3	0.28	1.20	0.012	0.94
XIV	0.024	4.87	0.00	35.3	0.22	1.00	0.054	0.90
XVI	0.009	1.71	0.01	37.3	0.23	1.43	0.012	0.98
Median	0.019	5.15	8.64	38.8	0.24	1.10	0.013	0.98
$[Q_1, Q_3]$	$[0.012, 0.042]$	$[2.58, 10.52]$	$[0.00, 32.40]$	$[35.8, 41.1]$	$[0.21, 0.25]$	$[1.00, 1.54]$	$[0.010, 0.019]$	$[0.93, 0.99]$

Table 2.4: Constitutive parameters for the intact (three-layer composite) wall of the human thoracic and abdominal aortas; together with the coefficient of determination R^2, the median, the first quartile Q_1 and the third quartile Q_3.

supra-physiological loading and accurate modeling of stresses at such load levels are an important pre-requisite for modeling damage and understanding damage mechanisms in the tissue.

Furthermore, the example implies that the response of the tissue greatly depends on the maximum strain energy which the tissue has experienced in the load history. It is, thus, important to pre-condition arterial tissues with loads very similar to physiological loading states, otherwise a hyperelastic material model may not capture the *in vivo* material behavior. For example, if pre-conditioning is conducted with loads that are too high, i.e. beyond the physiological range, the tissue stresses will be underestimated because softening of the tissue sample is greater than the softening of the tissue *in vivo*.

2.3.4 Statistical Analysis

Here we analyze possible statistically-relevant differences ($p < 0.05$) between the fit constitutive parameters from the thoracic and abdominal aortic tissue layers. In addition, we investigate possible correlations between the constitutive parameters, and age and gender.

Intima	μ [MPa]	k_1 [MPa]	k_2 [-]	φ [°]	κ [-]
Pre-conditioned	0.031	2.4	62.3	47.0	0.13
Non pre-conditioned	0.031	2.5	11.3	47.0	0.13
Media					
Pre-conditioned	0.032	0.09	19.0	41.6	0.12
Non pre-conditioned	0.034	0.15	17.1	39.3	0.22
Adventitia					
Pre-conditioned	0.027	0.37	15.2	54.8	0.25
Non pre-conditioned	0.024	0.40	11.0	54.7	0.25

Table 2.5: Representative effect of pre-conditioning (up to a stress level of 150 kPa) on the (elastic) constitutive parameters for both the non pre-conditioned and the pre-conditioned intima, media and adventitia (Donor VII).

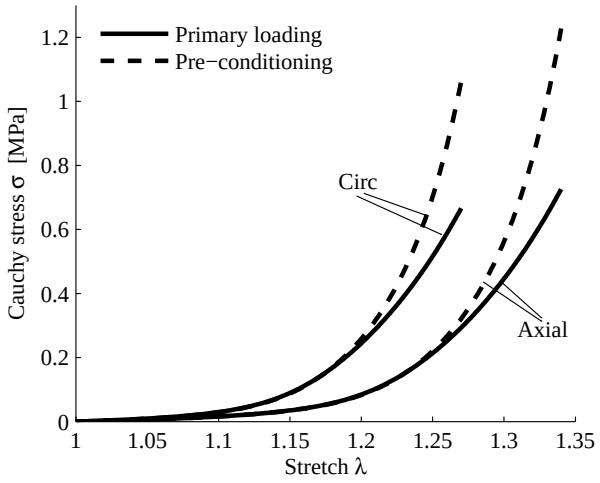

Figure 2.3: Representative effect of pre-conditioning (up to a stress level of 150 kPa) on the tissue response for the media of Donor VII. Response for the non pre-conditioned material (solid curves), and loading on the pre-conditioned material (dashed curves) for the constitutive parameters in Table 2.5.

Location	Layer	Parameter	r_s	CI	Linear regression
TA	M	k_1	0.61	$[0.12, 0.86]$	$0.0083\,\text{MPa yrs}^{-1}\,x - 0.304\,\text{MPa}$
TA	M	φ	-0.55	$[-0.83, -0.02]$	$-0.18^\circ\,\text{yrs}^{-1}\,x + 50.26^\circ$
TA	M	r_f	-0.59	$[-0.85, -0.09]$	$-0.033\,\text{yrs}^{-1}\,x + 3.964$
TA	A	μ	0.69	$[0.26, 0.90]$	$0.0007\,\text{MPa yrs}^{-1}\,x - 0.0172\,\text{MPa}$
TA	A	k_1	0.60	$[0.11, 0.86]$	$0.0224\,\text{MPa yrs}^{-1}\,x - 0.7458\,\text{MPa}$
TA	A	r_f	-0.62	$[-0.87, -0.14]$	$-0.023\,\text{yrs}^{-1}\,x + 2.750$
AA	A	r_f	-0.88	$[-0.98, -0.53]$	$-0.019\,\text{yrs}^{-1}\,x + 2.362$

Table 2.6: Significant correlation of the fit constitutive parameters with age. The confidence interval is calculated based on the confidence level of 95%. The equations for linear regression considers x, which denotes the age in yrs. r_s: correlation coefficient, CI: confidence interval, TA: thoracic aorta, AA: abdominal aorta, M: media, A: adventitia.

A statistically-relevant difference between the thoracic and abdominal aortas was found for the constitutive parameters κ (intima), for k_1, r_f (media) and for μ, k_2, φ and m_f (adventitia). Age dependency for the constitutive parameters was found for k_1, φ, r_f (media) and μ, k_1, r_f (adventitia) of the thoracic aorta, and for r_f (adventitia) of the abdominal aorta.

The constitutive parameters μ and k_1 increase, whereas the fiber angle φ and the damage parameter r_f decrease with age. The increase of parameters k_1 and μ with age indicates that the aorta stiffens progressively. This observation is in accordance with the arterial mechanics literature, see, for example, [88–90]. The decrease of φ with age may be due to remodeling of collagen, or the increase of cross-linking between the collagen fibers [89]. The decrease of r_f indicates that the maximum damage that can occur in the tissue increases, cf. (5.2), which might be associated with stiffening of the aortic tissue with age.

The values for the correlation coefficient r_s and the confidence interval (CI) together with the equations for the linear regression are summarized in Table 2.6 for different layers of thoracic and abdominal aortas. The linear dependency in age, as shown in Table 2.6, can be used in patient-specific finite element modeling of aortas.

A dependence of the constitutive parameters on the gender of the donors was not detected, as also reported by, for example, [91]. Nonetheless, the relatively small sample population (14 thoracic and 8 abdominal aortas) may contribute to the lack of a statistically-relevant results.

2.3.5 Histology

Traverse histological cuts oriented in the loading direction of the specimens and stained with picrosirius red are shown in Fig. 2.4; stretched with (a) $\lambda_\text{c} = 1.05$ and (b) $\lambda_\text{c} = 1.50$ in the circumferential direction, and with (c) $\lambda_\text{a} = 1.05$ and (d) $\lambda_\text{a} = 1.20$ in the axial direction. Note that in Figs. 2.4(a) and (b) the circumferential orientation of the specimen is

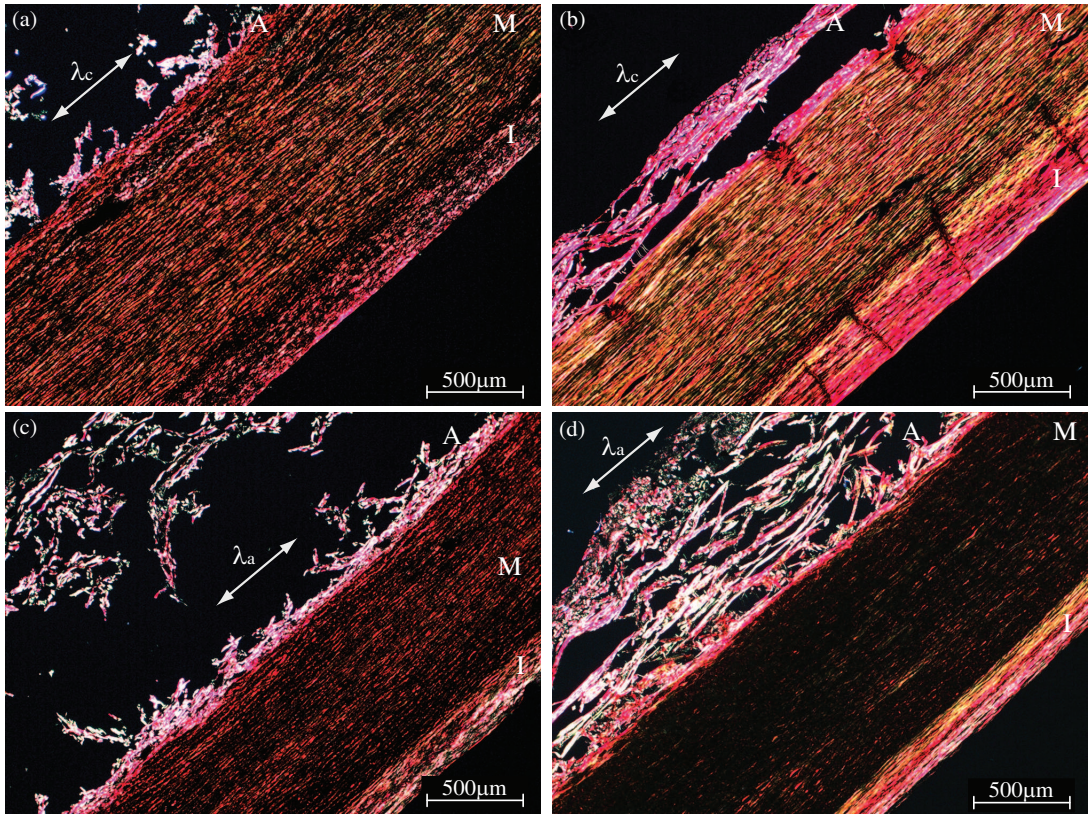

Figure 2.4: Collagen in the aortic wall visualized by picrosirius red staining at two circumferential stretches, i.e. (a) $\lambda_c = 1.05$ and (b) $\lambda_c = 1.50$, and at two axial stretches, i.e. (c) $\lambda_a = 1.05$ and (d) $\lambda_a = 1.20$. The orientation of the specimen is 45° from the horizontal direction, and the direction of the applied stretch (λ_c and λ_a) is indicated by a double-headed arrow; I: intima, M: media, A: adventitia.

rotated 45° from the horizontal, while in (c) and (d) that direction corresponds to the axial orientation of the specimen. For most specimens only a few laminae of the adventitia are still attached to the media, which is not due to the stretching of the tissue. The separation happens during microtome cutting of the histological specimens due to the different mechanical properties of the collagen fabric within the different layers. The brightness of the collagen fibers increases in all three tissue layers with loading in the circumferential direction (see Figs. 2.4(a) and (b)) indicating an increase in the alignment of the fibers. Higher loading results in this alignment of fibers, from a wavy form in an unloaded state, where only short and irregularly arranged sections of fibers are visible, to a more aligned form in the loaded state, where longer and more parallel or near parallel fibers are visible. With an increase of aligned fibers the birefringent structures increase in one histological cutting plane and result in more brightness. This effect is especially pronounced in the intima and adventitia. Under applied stretches in the axial direction, the brightness of the collagen in the media decreases while there is a brightness increase for the intima and the adventi-

tia (see Figs. 2.4(c) and (d)). The decrease in brightness for the media under axial stretch is seen because the collagen fibers in the media are oriented more in the circumferential direction so that an axial stretch does not align the fibers in the cutting plane.

Planar histological cuts, oriented in the plane of the tissue, of intimal specimens stretched in the circumferential direction, again stained with picrosirius red, are shown in Fig. 2.5, for (a) $\lambda_c = 1.05$, (b) $\lambda_c = 1.35$ and (c) $\lambda_c = 1.50$, where the direction of the applied stretch corresponds to the horizontal direction of the image which is the circumferential direction of the aorta. The alignment of the fibers increases with increasing applied stretches, and the angle between the fiber families and the circumferential direction φ decreases. This observation is in agreement with the underlying kinematics where the direction of the fibers in the current configuration $\mathbf{m}$ is obtained by applying the deformation gradient on the fiber direction in the reference configuration, i.e. $\mathbf{m} = \mathbf{FM}$. Collagen fiber alignment under pressure is also reported in [37]. The mean angles of the collagen fibers are $\varphi = 45.3^\circ$, 41.6°, 21.4° for $\lambda_c = 1.05, 1.35, 1.50$, respectively. An increase of the angle φ is observed for axial stretching of the tissue (results not shown).

Reviewing Figs. 2.4 and 2.5 in view of the mechanical stress-stretch data indicates that softening in the physiological loading range as well as in the supra-physiological loading range might be due to the alignment of these components, if it is not fully reversible. Furthermore, it indicates that softening does not result from (massive) fiber rupture as, for example, assumed in the model by Rodríguez et al. [43].

2.3.6 Comparison with Other Models

The pseudo-elastic damage model gives an excellent fit to the experimental data, with relatively few constitutive parameters, as it only introduces two damage parameters, contrary to models that account for damage in matrix and fibers, see, for example, [63]. Associating damage accumulation primarily in the collagen fibers has previously been assumed in several studies, for example, in the arterial damage model of Balzani et al. [78]. This assumption has now been justified by experimental data. The model by Balzani et al. [78] also uses two damage parameters. Additionally, a value for the strain energy, which describes the initial damage state, is defined *a priori* such that softening is not described in the physiological loading range. Hence, three parameters are needed in total to describe the damage behavior of the tissue. Defining an appropriate value for the strain energy, which describes the 'initial damage state', is difficult, especially as no adequate experimental data exist to the authors' knowledge. The proposed pseudo-elastic damage model adequately describes softening that occurs during pre-conditioning and actual damage in the supra-physiological loading range. This means that values for the damage variable, which distinguish tissue softening in the physiological loading range from softening due to damage, need to be determined. Therefore, the definition of an appropriate threshold value for the damage variable, and more experimental and numerical studies are necessary for a correct interpretation of the damage variable.

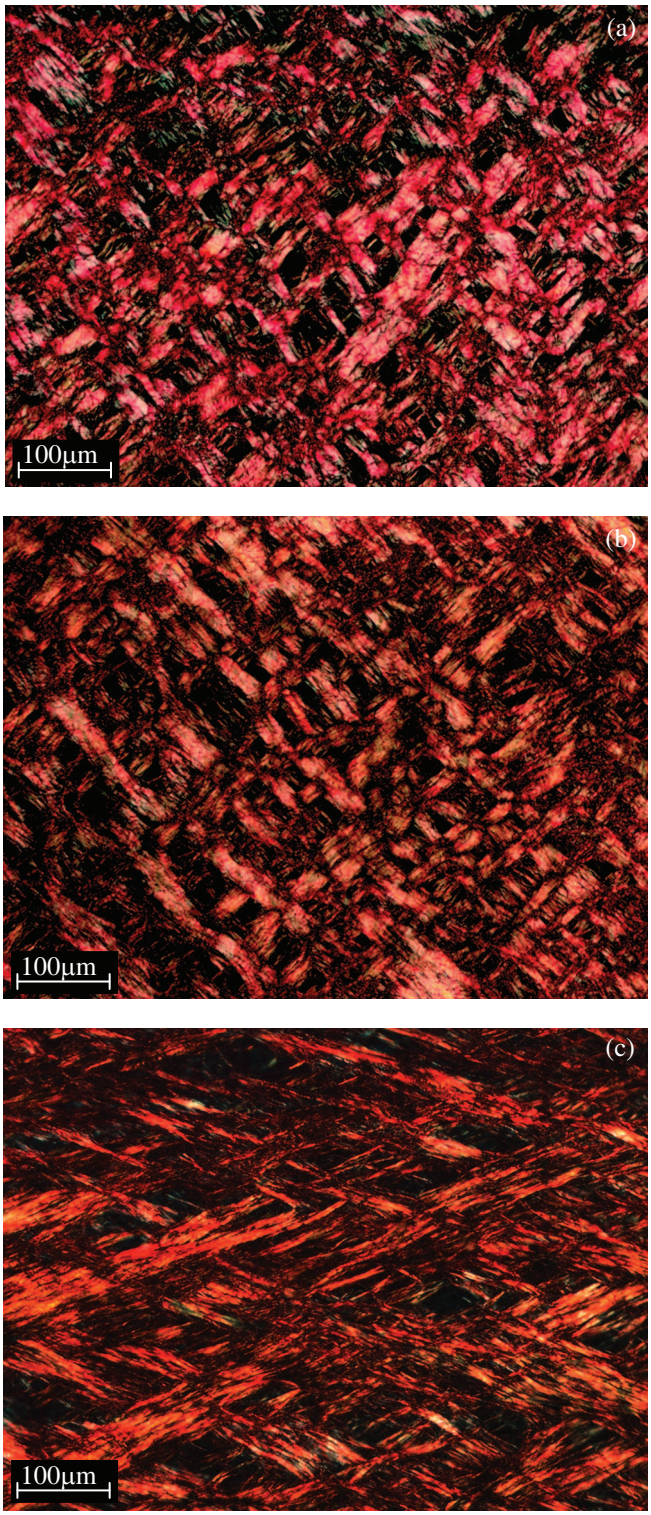

Figure 2.5: Collagen fibers in a planar cut of the intima visualized by picrosirius red staining at increasing applied circumferential stretches: (a) $\lambda_c = 1.05$, (b) $\lambda_c = 1.35$ and (c) $\lambda_c = 1.50$. The direction of applied stretch corresponds to the horizontal.

As opposed to the model presented by Peña et al. [66] and Balzani et al. [60], our model does not account for continuous damage. Some specimens tested have shown a very slight continuous softening and permanent deformation after unloading, which is not captured by the proposed pseudo-elastic damage model. Nevertheless, the proposed model is in good agreement with the experimental data. Therefore, and in order to avoid an increase in the number of constitutive parameters, only discontinuous softening is accounted for in the model. Peña [69] presents a model that incorporates a permanent deformation after tissue unloading. The presented pseudo-elastic damage model can easily be extended to describe this effect by using the approach presented by, for example, [49].

2.4 Conclusion

Experimental data on human tissues are crucial for the numerical simulation of catheter-based procedures such as the placement of a stent graft. In this study layer-specific experimental data of uniaxial extension tests under supra-physiological loading for human aortas were presented. Uniaxial experiments were used because higher loads can be applied to the tissues than in biaxial experiments. Fitting the model to the obtained data generates physiologically consistent results, for example, for the fiber angles. Hence, the model is able to capture the behavior at physiological loading, even though uniaxial extension tests do not mimic the physiological loading condition.

A novel pseudo-elastic damage model, which describes discontinuous softening, was fit to the experimental data. The pseudo-elastic damage approach was favored because therein it is possible to first fit the material parameters, independently of the damage parameters, which simplifies the fitting process. The proposed damage model is able to provide an excellent fit to the experimental data while employing a relatively low number of constitutive parameters. The fits with and without consideration of damage accumulation in the non-collagenous matrix material indicate that tissue damage is only accumulated in the collagen fiber fabric. Several models assume that damage is only attributed to the collagen fibers, however, experimental data and constitutive fits supporting this phenomenon have not been presented before. Nonetheless, the assumption of this study still needs to be confirmed by appropriate experiments in future studies.

The proposed approach for modeling damage does not include the definition of a minimum strain energy for damage initiation as done in several previous studies (see, for example, [63, 78]) because pre-conditioning can already be described by the Mullins effect. However, this means that softening already occurs at physiological load levels and a threshold for the damage variable needs to be determined to distinguish softening in the physiological loading range from softening due to tissue damage. In order to analyze such a distinction further experimental data and numerical studies are required.

Our model captures only the passive mechanical behavior aortic tissues which has important ramifications; for example, active behavior due to smooth muscle cell may also play

an important role with respect to damage accumulation. The influence of smooth muscle cell should, therefore, be considered in subsequent studies. Naturally, adequate modeling of the passive tissue response, as demonstrated here, is a pre-requisite for modeling the active tissue response. Furthermore, the purely mechanical nature of the model can only predict the tissue response immediately after exposure to supra-physiological loading. We do not account for biological or biochemical processes such as cell death [56] or neo-intimal hyperplasia [92] that are triggered by over-stretching the tissue, and which may alter mechanical properties of the tissue.

3 THE ROLE OF ELASTIN AND COLLAGEN IN THE SOFTENING BEHAVIOR OF THE HUMAN THORACIC AORTIC MEDIA

Abstract In a previous study we were able to accurately fit experimental data on arterial tissues at supra-physiological loads using a material model that accounts for softening/damage only in the portion of the model associated with the collagen fibers (*J. Mech. Behav. Biomed. Mater.* **12**:93–106, 2012). Naturally, this result leads to the hypothesis that the softening behavior is related only to the collagen fibers, and not to the matrix material. In this study we test this hypothesis by conducting uniaxial extension tests on elastase and collagenase treated tissues and on untreated control specimens from the media of human thoracic aortas. We relate structural changes in the tissue after enzyme treatment to changes in the corresponding mechanical behavior. Collagenase treated tissue does not exhibit any softening behavior under quasi-static cyclic loading, a result supporting our hypothesis. Conversely, elastase treated tissue exhibits continuous softening under the same loading conditions, indicating that the integrity of the tissue is destroyed upon removal of the elastin. Finally, we fit isotropic and anisotropic constitutive models to the mechanical response of the collagenase treated arterial tissue. While our anisotropic model better approximates the response of collagenase treated arterial tissues, we show that an isotropic matrix model is sufficient to accurately reproduce the mechanical response of untreated control specimens, consistent with current practice in the literature.

3.1 Introduction

In a recent study we showed that softening in aortic tissues due to supra-physiological loads can be modeled by accounting only for the softening in the strain energy associated with the collagen fibers, and not for the matrix material [93]. This phenomenological result leads naturally to the hypothesis that the softening behavior is associated only with the collagen fibers. To investigate this hypothesis, we perform experiments on both collagenase treated tissues and elastase treated tissues, as well as untreated control tissues, to gain more insight in the softening mechanisms associated with the collagen fibers.

Roach and Burton [94] conducted the first study which isolated the mechanically relevant constituents of arteries, namely elastin and collagen, and investigated the resulting mechanical responses. These authors showed that elastin is responsible for the initially compliant behavior at lower strains and that collagen is responsible for a stiffening behavior at higher strains. Experiments conducted by Dobrin et al. [95] showed that the radius of

the vessels increases after elastase treatment, indicating that elastin keeps the arterial wall in its original shape. Dobrin and Canfield [96] stated that it is necessary to select enzyme activity and digestion time such that collagen is only partially digested, otherwise inflation tests are not possible due to leaking or rupture of the specimens.

Determining the mechanical properties of elastin, the main component of elastic fibers, has recently attracted increased attention. Gundiah et al. [97] performed planar biaxial extension tests that show an isotropic stress-stretch behavior which they initially modeled using the neo-Hookean material model. However, the authors report that elastic fibers of porcine arteries are oriented axially in the intima and the adventitia, and circumferentially in the media. The authors believe that this finding motivates an anisotropic model for the non-collagenous matrix. As a result of their structural findings, they propose an invariant-based orthotropic strain-energy function [98].

Lille et al. [99] performed mechanical tests on purified elastic fiber network tissue obtained from the thoracic aorta of pigs. In uniaxial tests this tissue is stiffer in the circumferential direction compared to axial. The authors then compared four constitutive models to predict the pressure-circumferential stretch behavior. They conclude that models incorporating both anisotropy and nonlinearity best predict the mechanical behavior of the elastic fiber network.

Similarly, Zou and Zang [100] investigated the mechanical properties of the elastic fiber network under biaxial tensile loading for the bovine thoracic aorta. Their experiments also show an anisotropic mechanical response with the circumferential direction being stiffer than the axial direction. The authors propose an eight-chain statistical mechanics based microstructural approach to model the mechanical behavior of the elastic fiber network. The same authors also investigated the time-dependent behavior using biaxial stress relaxation and creep experiments [101]. Their experimental results reveal that the creep response is negligible.

In this study we perform uniaxial extension tests to study the mechanical behavior of the media of the human thoracic aorta under relatively large loads. While uniaxial extension tests do not mimic the physiological loading condition, meaningful results can be obtained when the resulting data are carefully fitted [77]. Planar biaxial extension tests better represent the physiological loading conditions. However, they are difficult to perform within the supra-physiological loading domain, and they may lead to poor estimates of the stress, as shown both experimentally [102] and numerically [103]. Pressure inflation tests mimic physiological conditions well, however, the size of our samples did not allow such tests. Furthermore problems may arise due to leakage through the small side branches, especially at supra-physiological pressures.

In this study we compare the mechanical behavior of elastase and collagenase treated media from human thoracic aorta to untreated control specimens. We seek to understand the role of elastin and collagen in the softening behavior observed in untreated specimens at

physiological and supra-physiological loads. Furthermore, both the isotropic neo-Hookean model and an anisotropic model are used to mathematically describe the mechanical response of the elastic fiber network. We discuss the implications of our model fits for elastin on modeling the untreated aortic tissue. We also qualitatively describe anisotropy observed in the continuous softening of elastase treated specimens.

3.2 Materials and Methods

We conduct uniaxial extension tests on circumferentially and axially aligned specimens of the media of 17 human thoracic aortas (66 ± 8 yrs, mean $\pm$ SD), under stretch magnitudes within the physiological and supra-physiological range.

We obtain the specimens from patients undergoing autopsy up to 24 hours after death unrelated to cardiovascular disease and we stored them in physiological solution. When possible, we test tissue specimens within 48 hours after excision. Otherwise, we immediately freeze the specimens and test them within 24 hours of unfreezing. The Ethics Committee of the Medical University of Graz approved the use of autopsy material from human subjects.

We base our protocol for enzyme treatment on the work of both Dobrin and Canfield [96] and Kratzberg et al. [104]. We perform the elastase treatment for two hours in a 100 U/ml physiological solution for a complete digestion of elastin and the collagenase treatment for 16 hours in a 4000 U/ml or 20 hours in a 5000 U/ml physiological solution for partial or complete digestion of collagen, respectively, all at 37°C.

For the collagenase treated tissue, we test seven specimens containing negligible amounts of residual collagen (Donors 1 to 7) and five specimens with partially digested collagen (Donors 8 to 12). For the elastase treated tissue, we test a total of five specimens (Donors 13 to 17). If the tissue specimens are sufficiently large, we also test untreated control specimens from each donor for comparison.

In order to verify enzymatic digestion of the intended tissue constituent, we examine histological images using both Elastica van Gieson and Picrosirius red stains. If collagen is still visible in a histological image, we determine the area fraction of collagen in the cross-section using image analysis tools in MATLAB (2009b, The MathWorks, Inc., Massachusetts, United States). We include specimens with visible collagen residues of less than 5% area fraction in our analysis, but they are marked with an asterisk * to distinguish them from those specimens without visible collagen residues. Additionally, we have five specimens with larger residues in the range of $20-40$% collagen area fraction. We compare the latter qualitatively to corresponding data from control and enzyme-treated specimens.

In order to evaluate the ultrastructure of the tissue by transmission electron microscopy (TEM) we fix the aortic specimens in 2.5% glutaraldehyde in cacodylate buffer (pH 7.3)

for four hours at room temperature, followed by washing steps in cacodylate buffer solution. Subsequently, we postfix all specimens in 1% osmium tetroxide (OsO_4) solution for two hours, wash in cacodylate buffer, and dehydrate in increasing concentrations of ethanol at room temperature, passed through propyleneoxide and embedded in Agar 100 resin. We then collect ultrathin sections cut with a ultramicrotome (Drukker International, Cuijk, The Netherlands) on mesh copper grids, stain using uranyl acetate and lead citrate, and examine the specimens with a Philips 100 electron microscope (Philips Electronics N. V., Eindhoven, The Netherlands).

The protocol for mechanical testing is similar to that reported previously in [93]. Briefly, we cut dog bone specimens with a gage width of 4 mm from the aortic tissue in both circumferential and axial directions. Next, we remove the intima and adventitia using tweezers. We assume that the mechanical influence of internal and external elastic lamina, if present, can be neglected. To calculate the thickness we average four measurements taken using a videoextensometer (ME $46-350$, Messphysik, Fürstenfeld, Austria).

We conduct the mechanical tests using a uniaxial testing machine (μ-Strain ME $30-1$, Messphysik, Fürstenfeld, Austria) with the tissue in a bath of physiological solution at 37°C. The videoextensometer records the stretch in the gauge region of the specimen by tracking two black markers glued onto the specimen. We determine the unloaded length when the specimen is clamped and immersed in the bath at zero force. Labrosse et al. [105] report, e.g., that the mean circumferential and axial stretches are 1.31 and 1.11, respectively, for the human thoracic aortic wall. Our force driven protocol prescribes the first Piola-Kirchhoff stress (engineering stress) to be 10, 25, 50, 100 kPa for the elastase treated specimens as well as the axially-aligned collagenase treated specimens. Since they can bear more load, we load the circumferentially-aligned collagenase treated specimens as well as the control specimens to 50, 100, 300, 500 kPa. In these tests we complete three cycles for each load step. For four additional circumferentially-aligned, elastase treated specimens we apply cyclic loading to the first load step (10 kPa) to monitor the evolution of continuous softening in the specimen until rupture. In all cases the testing speed equals 5 mm/min to ensure quasi-static behavior of the tissue.

3.2.1 Data Analysis

In all our subsequent analyses we convert uniaxial force-displacement data to Cauchy stress-stretch data for constitutive model fitting. We evaluate the Cauchy stress σ from the experimental data as

$$\sigma = \frac{f}{WT}\lambda, \tag{3.1}$$

where f is the current force, W and T are initial width and thickness of the specimen, and λ is the applied uniaxial stretch [93, 106].

In all that follows we use convex strain-energy functions, say Ψ, defined per unit volume in the reference configuration, to model nonlinear materials undergoing finite strains. The

Cauchy stress tensor σ follows from the strain-energy function as $\sigma = 2J^{-1}\mathbf{F}(\partial\Psi/\partial\mathbf{C})\mathbf{F}^{\mathrm{T}}$, where $\mathbf{C} = \mathbf{F}^{\mathrm{T}}\mathbf{F}$ is the right Cauchy Green tensor, $\mathbf{F}$ is the deformation gradient tensor and $J > 0$ is the Jacobian, the determinant of the deformation gradient [25]. Note that we assume an incompressible behavior, and hence have $J = 1$.

We determine the constitutive parameters using a nonlinear-least squares algorithm implemented in the MATLAB. The goodness-of-fit is reported using the square of the Pearson's correlation coefficient R^2.

Collagenase treated specimens

The macroscopic mechanical response of elastin in arterial tissues is commonly modeled using an incompressible neo-Hookean material, see, e.g., [7, 107]. Correspondingly, we fit the experimental data from the collagenase treated specimens using the strain-energy function

$$\Psi_{\mathrm{nH}} = \frac{\mu_{\mathrm{nH}}}{2}\,(I_1 - 3)\,, \tag{3.2}$$

where $\mu_{\mathrm{nH}} > 0$ is the initial shear modulus and $I_1 = \mathrm{tr}\mathbf{C}$.

Since we observe an anisotropic mechanical response for all tissue specimens, and both Clark and Glagov [108] and Gundiah et al. [97] show that elastic fibers are arranged circumferentially in medial tissue, we propose a transversally isotropic strain-energy function Ψ_{ti} of the form

$$\Psi_{\mathrm{ti}} = \frac{\mu_{\mathrm{ti}}}{2}\,(I_1 - 3) + c_{\mathrm{ti}}\,(I_{4\mathrm{m}} - 1)^2\,, \tag{3.3}$$

where $\mu_{\mathrm{ti}} > 0$ and $c_{\mathrm{ti}} > 0$ are material parameters, and $I_{4\mathrm{m}} = \mathbf{M}_{\mathrm{m}} \cdot \mathbf{C}\mathbf{M}_{\mathrm{m}}$ is the square of the stretch in the direction $\mathbf{M}_{\mathrm{m}}$, describing the orientation of the elastic fibers in the reference configuration.

In this formulation, we assume that $\mathbf{M}_{\mathrm{m}}$ is aligned with the circumferential direction, hence $I_{4\mathrm{m}} = \lambda^2_{\mathrm{circ}}$. Additionally, the second term in (3.3) only contributes to the total strain energy Ψ_{ti} for $I_{4\mathrm{m}} > 1$, i.e. when the elastic fibers in the circumferential direction are in tension.

Untreated wall

We assess the influence of the two models for elastin by fitting the primary loading curves of the untreated control specimens, using both Ψ_{nH} and Ψ_{ti} and the corresponding material parameters for the elastin constituent as a starting point. We model the primary loading curve of the untreated arterial tissue by extending the strain-energy function using

$$\Psi = \Psi_{\mathrm{m}} + \Psi_{\mathrm{f},i}, \tag{3.4}$$

where Ψ_{m}, $\mathrm{m} \in [\mathrm{nH}, \mathrm{ti}]$, describes the mechanical response of the non-collagenous matrix material and $\Psi_{\mathrm{f},i}$ describes the mechanical response of two families of collagen fibers $i = 4, 6$. More specifically [39]

$$\Psi_{\mathrm{f},i} = \frac{k_1}{2k_2}\{\exp[k_2(I_i^\star - 1)^2] - 1\}, \qquad I_i^\star = \kappa I_1 + (1 - 3\kappa)I_i, \quad i = 4, 6, \tag{3.5}$$

where $k_1 > 0$ and $k_2 > 0$ are material parameters, and κ describes the dispersion of the collagen fibers about their principal directions. Additionally, $\Psi_{\mathrm{f},i}$ only contributes to the strain-energy function Ψ if $I_i^\star > 1$.

The pseudo-invariants $I_4 = \mathbf{M} \cdot \mathbf{CM}$ and $I_6 = \mathbf{M}' \cdot \mathbf{CM}'$ correspond to the square of the stretches of the collagen fibers in the mean fiber directions, while the vectors $\mathbf{M}$ and $\mathbf{M}'$ denote the directions of the collagen fibers in the reference configuration. Since the fibers are assumed to be symmetrically oriented with respect to the arterial axis and located in the tangential plane of the artery their directions are uniquely defined by the angle φ measured from the circumferential direction of the artery. We fit the untreated control specimens from Donor 1 to 7 twice: once starting from the fitted result for (3.2), i.e. μ_{nH} (denoted as Case 1 and indicated by subscript c1); and once starting from the fitted result for (3.3), i.e. μ_{ti} and c_{ti} (denoted as Case 2 and indicated by subscript c2). We use the goodness-of-fit to determine whether it is necessary to use the more sophisticated material model (3.3) for the elastin matrix when modeling the untreated tissue composite.

Elastase treated specimens

The elastase treated specimens exhibit severe continuous and discontinuous softening such that we do not fit them to a constitutive model. Rather, we analyze the amount of softening in terms of the stress applied to the tissue. To this end, we plot the incremental increase in stretch due to continuous softening, referred to as $\Delta\lambda$, versus both the applied stress and the load step number. Specifically, we define $\Delta\lambda$ as the increase in stretch at maximum load measured from one load step to the subsequent load step.

3.3 Results

To put the mechanical response of the enzyme treated specimens into context, Fig. 3.1 shows data for a representative untreated control specimen (female, 45 yrs). Note the pronounced anisotropy and discontinuous softening as well as the nonlinear stiffening.

3.3.1 Structural Changes After Enzyme Treatment

Figure 3.2 shows representative structural changes after elastase and collagenase treatment compared to the control specimens.

In Figs. 3.2(a) – (c) Elastica van Gieson stains the elastic fibers black. After elastase treatment these fibers are removed, i.e. no longer visible, whereas for the collagenase treated tissue no change is observed. SMC nuclei are still visible after elastase treatment, see the arrow in Fig. 3.2(b). In Figs. 3.2(d) – (f) Picrosirius red stains the collagen fibers dark red. After collagenase treatment these fibers are removed, i.e. no longer visible. However, after elastase treatment collagen fibers remain in the tissue, i.e. are clearly visible.

The TEM images in Figs. 3.2(g) – (i) show collagen fibrils in the untreated control and the elastase treated specimens, where the structure clearly changes. The collagen fibers in the

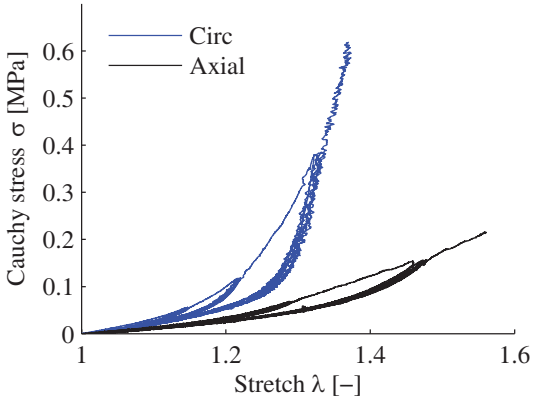

Figure 3.1: Representative untreated control specimen (female, 45 yrs) showing pronounced anisotropy, nonlinear stiffening and discontinuous softening.

elastase treated specimen (Fig. 3.2(h)) appear less organized and less densely packed when compared to the control specimen (Fig. 3.2(g)). The TEM image in Fig. 3.2(i) shows that the collagen fibrils in the collagenase treated specimen are completely removed, i.e. no longer visible.

3.3.2 Collagenase Treated Specimens

The collagenase treated tissue exhibits a slightly anisotropic response with neither continuous nor discontinuous softening. Figure 3.3(a) compares the mechanical responses in the circumferential direction of a representative untreated control specimen (blue) with a specimen where collagen is partially digested (red) and a specimen where collagen is completely digested (black). The mechanical response changes progressively from highly nonlinear, with pronounced discontinuous softening, to nearly linear without softening. Figure 3.3(b) shows a representative cross-section of a specimen with partially digested collagen. Arrows mark the area in which residual collagen is still present.

Table 3.1 summarizes the constitutive fit of the neo-Hookean model (3.2) and of the anisotropic model (3.3) to the mechanical data generated from the collagenase treated specimens. Figure 3.4 shows a representative plot of the resulting constitutive model fits to the data (Table 3.1, Donor 2). For all specimens tested, the circumferential direction exhibits a stiffer response, and the anisotropic strain-energy function yields a better goodness-of-fit.

Table 3.2 summarizes the constitutive fit and goodness-of-fit for the composite tissue model (3.4)-(3.5), using either Ψ_{nH} (3.2) or Ψ_{ti} (3.3) for Ψ_{m} in (3.4), to the mechanical data generated from the untreated tissue specimens. The goodness-of-fit does not increase notably if the anisotropic strain-energy function (3.3) is used to describe the elastin matrix in (3.4).

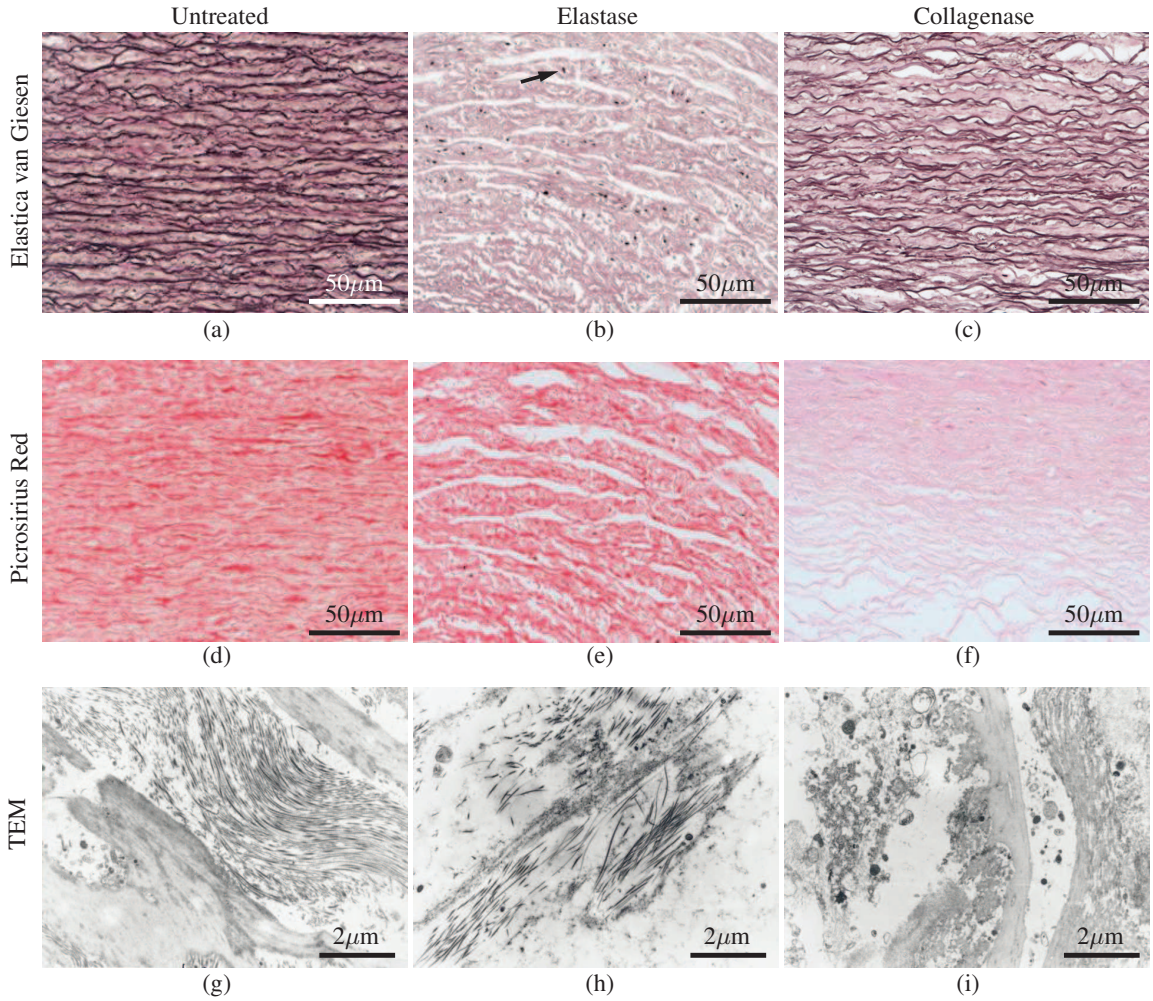

Figure 3.2: Representative comparison of elastase treated (middle), collagenase treated (right) and untreated control specimens (left) of the medial layer of the human thoracic aorta in light and transmission electron microscopy (TEM): (a) – (c) Elastica van Gieson stain visualizing elastic fibers and SMC nuclei (arrow) in black; (d) – (f) Picrosirius red stain visualizing collagen fibers in dark red; (g) – (i) TEM of the ultrastructure of collagen and elastin.

3.3.3 Elastase Treated Specimens

The elastase treated tissue from the medial layer of human thoracic aorta exhibits continuous softening as well as discontinuous softening. Figure 3.5(a) shows representative experimental data for the elastase treated tissue. Figure 3.5(b) shows the incremental increase in stretch $\Delta\lambda$, as defined in Fig. 3.5(a), versus the Cauchy stress at each load cycle for all tested specimens. The first hysteresis loop at each load step is slightly larger than the subsequent load steps, indicating discontinuous softening. Tissue anisotropy is clearly visible in the data; the stress values at a fixed stretch are much lower for the axial specimens than for the circumferential specimens. Additionally, the incremental increase of stretch at

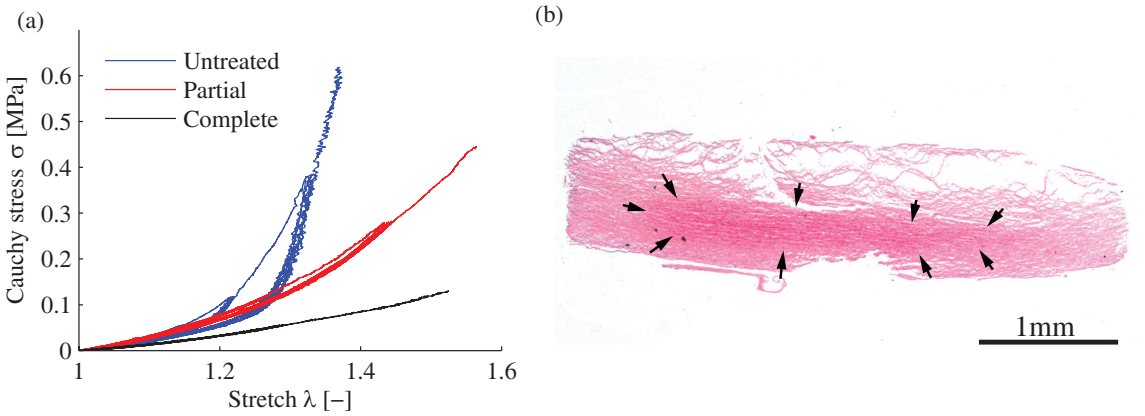

Figure 3.3: The influence of collagen digestion on the media from the human thoracic aorta: (a) representative mechanical responses in the circumferential direction of an untreated control specimen (blue, female, 45 yrs), a specimen with partial collagen digestion (red, female, 45 yrs) and a specimen with completely digested collagen (black, male 66 yrs); (b) Picrosirius red stain of a representative specimen with partially digested collagen, the area with residual collagen present is indicated by arrows.

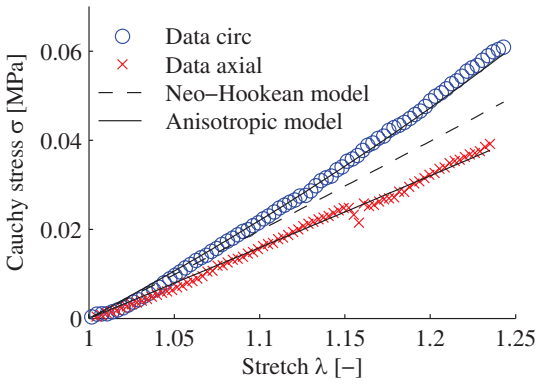

Figure 3.4: Representative constitutive model fits for the neo-Hookean (isotropic) model and the anisotropic model compared to the experimental data generated on collagenase treated tissue from the medial layer of a human thoracic aorta (female, 62 yrs).

each load cycle is higher for the axial direction than for the circumferential direction for a given stress.

Figure 3.6(a) shows a representative behavior of an elastase treated aortic media after a high number of quasi-static load cycles up to a constant maximum load, while Figure 3.6(b) shows again that the first hysteresis loop is bigger than the subsequent ones. The hysteresis resulting from continuous softening does not change appreciably with the number of applied load cycles conducted in the experiment.

Donor	Gender [m/f]	Age [yrs]	μ_{nH} [kPa]	R^2_{nH} [−]	μ_{ti} [kPa]	c_{ti} [kPa]	R^2_{ti} [−]
1	f	63	62.04	0.864	53.20	12.65	0.992
2	f	62	65.58	0.894	52.78	12.03	0.997
3*	m	76	44.60	0.926	31.35	7.62	0.990
4	m	66	50.11	0.988	37.15	4.67	0.990
5*	m	53	116.90	0.917	88.09	16.08	0.988
6	m	66	75.94	0.748	58.10	20.46	0.979
7	m	64	108.04	0.919	89.07	11.45	0.984
Median		64	65.58	0.917	53.20	12.03	0.990

Table 3.1: Constitutive parameters for the non-collagenous (elastin) matrix, from the medial layer of human thoracic aorta, for both the neo-Hookean model (μ_{nH}) and the anisotropic constitutive model (μ_{ti} and c_{ti}), including age and gender of the patients (m = male and f = female). Specimens marked with an asterisk * showed small residues of collagen on the histological specimens (area fraction $\leq 5\%$).

Additionally, the specimens exhibit residual deformation after unloading the tissue. The magnitude of residual deformation increases both with increasing load (cf. Fig. 3.5(a)) and with increasing number of load cycles (cf. 3.6(a)).

3.4 Discussion

3.4.1 Collagenase Treated Specimens

Our results demonstrate that the elastic fiber network exhibits an anisotropic mechanical response, consistent with several other studies reported in the literature [98–100]. Additionally, Gundiah et al. [97] suggest that, in spite of their isotropic data, it is better to describe the non-collagenous matrix using an orthotropic material model based on the structure of the elastic fiber network which shows axially oriented fibers in the intima and the adventitia, and circumferentially oriented fibers in the media.

The circumferential orientation of the elastic fibers might explain the higher stiffness experimentally measured in the circumferential direction of our collagenase treated tissues. Furthermore, Fig. 3.2(b) shows that smooth muscle cells are present in the tissue after the collagenase treatment. These smooth muscle cells are also aligned circumferentially in the media [108]. Thus, it is possible that their passive response might slightly add to the measured anisotropy in the tissue.

We compare the performance of a neo-Hookean to an anisotropic material model. The neo-Hookean model is commonly used to model the elastin constituent in arterial tissues. However, the collagenase treated tissue exhibits a higher stiffness in specimens oriented

Donor	$k_{1,c1}$ [MPa]	$k_{2,c1}$ [−]	φ_{c1} [°]	κ_{c1} [−]	R^2_{c1} [−]	$k_{1,c2}$ [MPa]	$k_{2,c2}$ [−]	φ_{c2} [°]	κ_{c2} [−]	R^2_{c2} [−]
1	0.191	0.00	54.14	0.28	0.981	0.113	0.00	49.11	0.15	0.983
2	0.013	10.62	33.58	0.00	0.977	0.067	15.49	19.14	0.23	0.980
3			n.a.					n.a.		
4	1.163	16.54	46.51	0.23	0.997	1.539	11.40	47.24	0.27	0.996
5	0.046	10.45	36.84	0.00	0.989	0.128	7.50	35.57	0.08	0.989
6	2.879	53.41	54.00	0.28	0.940	2.296	24.05	48.86	0.20	0.939
7	0.214	8.55	38.94	0.00	0.966	0.319	6.09	38.11	0.07	0.961
Median	0.118	10.54	41.68	0.12	0.985	0.120	9.45	41.41	0.19	0.986

Table 3.2: Constitutive parameters and goodness-of-fit for the primary loading curve generated from the untreated media of the human thoracic aorta using either a neo-Hookean (isotropic) model (subscript c1) or an anisotropic model (subscript c2) to describe the non-collagenous matrix. Parameters related to the elastin matrix correspond to those given in Table 3.1 for either (3.2) or (3.3), and parameters related to the collagen fibers correspond to (3.5), all according to (3.4).

circumferentially. This result motivates an additional term in the strain-energy function to capture the higher stiffness in the circumferential direction. The constitutive model that we present is a special case of the orthotropic model proposed by Gundiah et al. [98]. Therein, motivated by modeling the complete, untreated arterial wall where elastic fibers are oriented axially in both the intima and the adventitia, the authors add a third term to their strain-energy function which they use to increase stiffness in the axial direction as well.

For collagenase treated tissue specimens, the anisotropic model provides a notably improved fit to the experimental data relative to the neo-Hookean model, as shown in Table 3.1 and Fig. 3.4. Hence, if the mechanical response of the non-collagenous matrix are to be accurately described, a transversely isotropic model should be favored over the commonly used neo-Hookean model.

For the non-collagenous matrix, our measured initial shear modulus has a median value of approximately 62 kPa. Gundiah et al. [97, 98] report average values of 163 kPa and 73 kPa for the initial shear modulus measured from autoclaved specimens. This is a reasonably good agreement when comparing porcine and human tissue.

We previously reported a lower value (28 kPa) for the median initial shear modulus associated with the non-collagenous matrix of the untreated medial layer of the human thoracic aorta [93]. If we model untreated specimens including contributions from both the matrix and the fibers to the total strain energy (3.4), the constitutive response in the low-stress region is defined by both the parameters μ and k_1. If we model collagenase treated specimens, the low-stress response is described only by μ (such that, effectively $k_1 = 0$). Hence,

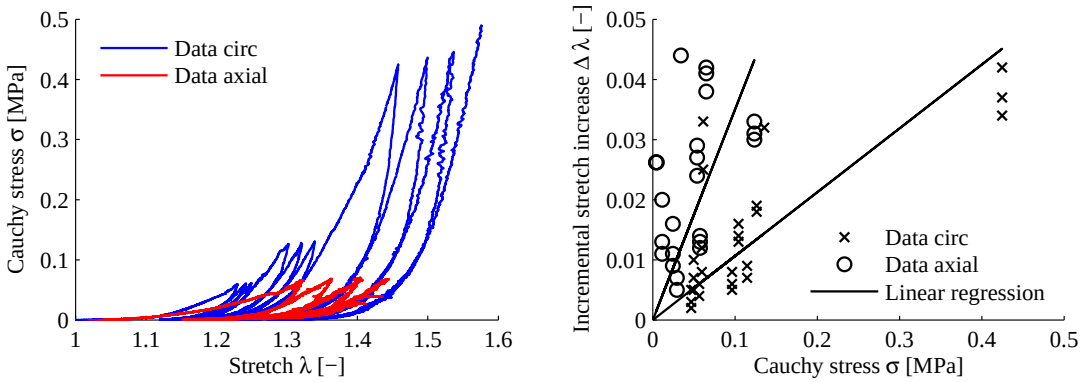

(a) (b)

Figure 3.5: Representative mechanical response of an elastase treated media from the human thoracic aorta – softening for three load cycles at each load step: (a) circumferential (blue) and axial (red) responses; (b) continuous softening of tissue in the circumferential (crosses) and axial (circles) directions, incremental increases in stretch $\Delta\lambda$ versus Cauchy stress for all tested specimens.

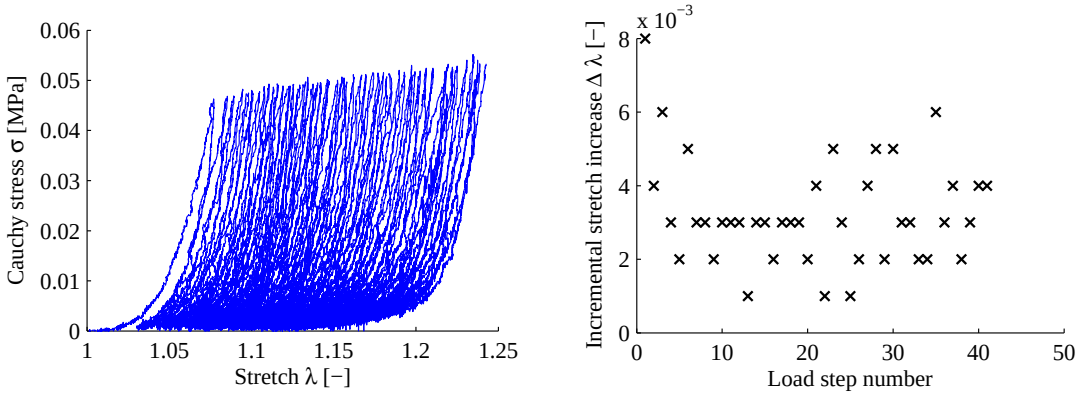

(a) (b)

Figure 3.6: Representative behavior of an elastase treated media from the human thoracic aorta under quasi-static cyclic loading of a circumferentially oriented specimen: (a) experimentally obtained Cauchy stress versus stretch; (b) incremental stretch increase versus load step number shows softening at each load cycle.

in the latter case μ must be higher to describe the same initial stiffness. The results summarized in Table 3.2 suggest that using a neo-Hookean model for the non-collagenous matrix, when building a constitutive model for the composite tissue composed of elastin and collagen, is justified despite the anisotropy of the elastic fiber network. The goodness-of-fit does not increase notably between the composite model (3.4) fitted using a neo-Hookean model for the matrix constituent and that including anisotropy of the matrix, while the number of material parameters is increased.

Our data (Fig. 3.3), support the hypothesis that the softening behavior is attributed only to the collagen fibers [93]. Thus, it is sufficient to model damage in arterial tissues by accounting for softening only in the part of the total strain-energy function associated with the collagen fibers, as performed by, e.g., [33, 93].

3.4.2 Elastase Treated Specimens

Anisotropy in the mechanical response of elastase treated human aortic tissue, as shown in Fig. 3.5(a), is largely due to the alignment of the collagen fibers within the tissue. Collagen fibers in the medial layer of human thoracic aorta generally align more toward the circumferential direction (albeit with dispersion about the mean direction), and, therefore, under an equivalent load the stretch of circumferentially aligned specimens is less than that of axially aligned specimens. The alignment of collagen fibers in arterial tissues has been shown with imaging techniques, see, e.g., [37, 40].

The specimens tested exhibit continuous softening, i.e. softening increases with the application of constant load cycles. We believe this mechanical effect implies that the collagen fibers are no longer adequately connected to the non-collagenous matrix, and that the fibers are 'sliding' against one other. Consequently, the collagen fibers can be pulled apart easily and show a creep-like behavior. The TEM image in Fig. 3.2(h) shows that the collagen fibers are less organized relative to the control specimen shown in Fig. 3.2(g). This supports our conjuncture that the integrity of the fiber network in the elastase treated tissue is reduced relative to the control specimen.

The creep-like mechanical behavior of the elastase treated tissue specimens is not likely to appear under physiological conditions as the arterial wall would enlarge during each cardiac cycle.

3.4.3 Limitations

The present study is restricted to the thoracic aortic media of arteries with non-atherosclerotic intimal thickening. Thus the dependence of the mechanical properties on age or on the location of the artery is not discussed, leaving room for further experimental studies. Furthermore, the collagenase and elastase treated tissues could not be taken from the same patient due to the sample size. However, the main conclusions of this study are not affected by this shortcoming.

The intima and adventitia were mechanically separated from the media, which may lead to artifacts or even damage in the vicinity of the separated surface. We assumed that these effects are negligible.

The model we selected to describe the untreated tissue is widely used (3.5); it assumes rotational symmetry of the collagen fibers. This is a limitation of the model as [40] showed that the out-of-plane dispersion is much lower than the in-plane dispersion. Therein, the authors also show that the collagen fibers are generally aligned more towards the circumferential direction in the media. In this light one would expect φ angels below 45° in

Table 3.2. This is not the case for all samples; however, the angels presented in Table 3.2 are fitting parameters.

Elastase treatment is used in several studies to digest elastin in arterial tissue, see, e.g., [23, 89, 96]. Elastase can attack denatured collagen, and Missirlis [109] suggest to add trypsin inhibitor during the elastase treatment to prevent collagen digestion; with such a treatment Fig. 3.6(a) may look different. Kronick and Sacks [110] use trypsin to digest proteoglycans in sheep skin. It hence is possible that elastase without trypsin inhibitor digests elastin and proteoglycans, whereas with trypsin inhibitor only elastin is digested. The role of proteoglycans on the softening of the tissue needs to be investigated in further studies.

Following Dobrin and Canfield [96], we assume that the influence of elastase treatment on the mechanical response of collagen is negligible. Results shown in Fig. 3.2 support our assumption by showing that collagen is still present after elastase treatment. Furthermore, significant digestion of collagen by collagenase takes a much longer time than digestion of elastin by elastase. Hence if denatured collagen is attacked by elastase treatment, it is likely that the activity and time of digestion are too low to have a noticeable influence on the mechanical behavior of the tissue.

3.5 Conclusion

Our mechanical experiments on the medial layer of the human thoracic aorta support a hypothesis commonly adopted in damage modeling of arterial tissue – that no softening is accumulated in the non-collagenous matrix. This matrix has an anisotropic mechanical response, with a higher stiffness in the circumferential direction. We propose an anisotropic constitutive model to describe this behavior, and successfully fit it to the experimental data. Despite the mechanical anisotropy of the non-collagenous matrix, we show that the neo-Hookean material model provides a sufficient description when building a phenomenological constitutive model for untreated tissue. However, constitutive models describing other structural aspects, e.g., growth and remodeling, may want to retain the anisotropy of the non-collagenous matrix or elastin. The mechanical response of elastase treated tissue shows both discontinuous softening and continuous softening. Thus, interaction between elastin and collagen fibers appears to be responsible for suppressing continuous damage in the untreated media.

4 A GENERALIZED PRESTRESSING ALGORITHM FOR FINITE ELEMENT SIMULATIONS OF PRE-LOADED GEOMETRIES WITH APPLICATION TO THE AORTA

Abstract Finite element models reconstructed from medical imaging data, e.g., computed tomography or magnetic resonance imaging (MRI) scans, generally represent geometries under *in vivo* load. Classical finite element approaches start from an unloaded reference configuration. We present a generalized prestressing algorithm based on a concept introduced by Gee et al. (Int. J. Num. Meth. Biomed. Eng. **26**:52-72, 2012) in which an incremental update of the displacement field in the classical approach is replaced by an incremental update of the deformation gradient field. Our generalized algorithm can be implemented in existing finite element codes with relatively low implementation effort on the element level, and is suitable for material models formulated in the current or initial configurations. Applicable to any finite element simulations started from pre-loaded geometries, we demonstrate the algorithm and its convergence properties on an academic example and on a segment of a thoracic aorta meshed from MRI data. Furthermore we present an example to discuss the influence of neglecting prestresses in geometries obtained from medical images, a topic on which conflicting statements are found in the literature.

4.1 Introduction

Medical imaging is frequently performed *in vivo*, and hence the reconstructed model geometry in the problem of interest represents the *in vivo* state, e.g., an artery at physiological blood pressure. Such *in vivo* states are generally loaded, and hence deformed and stressed. These stresses exist prior to reconstruction of the model geometry and thus we refer to this state as prestressed.

Classical continuum mechanics and finite element (FE) methods often assume that constitutive models, and the corresponding simulations, start from unloaded and stress-free reference conditions. When applying such classical approaches to patient-specific simulations of arteries a theoretical inconsistency arises: the *in vivo* determined 'initial' geometry is not an unloaded reference configuration.

Previous researchers have studied this theoretical inconsistency and generated various solutions. Schield [31] showed that the condition of equilibrium for a given elastically homogeneous material (with zero body forces) defines an inverse deformation, which for some other material is a state of equilibrium. Capitalizing on these ideas he proposed a formulation for inverse deformation problems in finite elasticity. Chadwick [111] used the duality

of the undeformed and deformed states in hyperelasticity to rewrite Schield's equilibrium equations into an energy-momentum formulation. Govindjee and Mihalic [32, 112] provided a re-parameterized formulation of the equilibrium equations in finite hyperelasticity to accommodate inverse deformations of compressible and quasi-incompressible engineering materials in a FE setting. The method is generally known as inverse design analysis and can be used to compute an unloaded reference configuration from a known deformed configuration with known boundary conditions. Inverse design analysis has been applied to engineering of turbine blades [113] and analysis of soft biological tissues [114, 115], [116] with success.

Specifically in soft tissue simulations initiated from *in vivo* imaged geometries, often the 'unloaded' reference configuration is not required, but only that the stress state within the tissue is in equilibrium with the known boundary conditions as imaged such that simulations can begin from this equilibrium state. This reframed problem has been approached by several researchers in the context of simulations of arteries. De Putter et al. [117] proposed a backward incremental method and validated it using several simple test problems with a neo-Hookean material. Unfortunately the authors provide little detail on the implementation of their method. Gee et al. [29, 30] proposed a method based on a Modified Updated Lagrangian Formulation (MULF), and used a multiplicative split of the deformation gradient to produce a displacement-free prestressed *in vivo* configuration. They obtain a prestressed state in the correct range and shape, and the maximum von Mises stress is generally predicted to within approximately 5% absolute error but do not discuss convergence properties of the algorithm. Gee et al. [30] showed that the implementation of the inverse design analysis into general FE codes is more involved than implementing MULF, and that application to comparatively thin-walled geometries can lead to buckling.

In the present work we suggest a Generalized Prestressing Algorithm (GPA) to simulate pre-loaded FE geometries, which is based on the seminal concept introduced by Gee et al. [30]. Briefly, an incremental deformation gradient is calculated from the incremental displacement field generated to ensure equilibrium at each iteration step. The incremental displacement field is then deleted and the deformation gradient field is updated with the incremental deformation gradient field. The proposed algorithm is not restricted to a specific FE formulation and can be used for hyperelastic material models formulated in the initial or current configuration. Furthermore, changes required to implement our algorithm are relatively minor and are all defined on the element level.

We demonstrate the convergence properties of the suggested algorithm using a simple academic example and a patient-specific, three-layer (intima, media, adventitia) segment of an thoracic aorta. To the authors' knowledge this is the first paper discussing the influences of a prestressing algorithm on a three-layer, patient-specific aorta segment including realistic fiber-reinforced material models based on experimental data. Our results show that inclusion of the prestress increases the maximum stresses estimated in the artery versus classical forward approaches, and that the error of the stress estimation depends on the size of the

load step per time increment. This implies that the error can be made arbitrarily small by sufficiently increasing the number of time steps. Convergence to the correct solution can be achieved with reduced computational cost by adding load-increment-free time steps at the end of the simulation.

Starting from the correct reference configuration is not only important for stress and rupture prediction in aneurysms but also for numerical simulation of catheter-based procedures such as stent-graft placement. We demonstrate that an incorrect initial reference configuration not only influences the stress magnitude and distribution, but also the estimated diameter of the vessel. Such errors have important ramifications in the simulation of patient-specific placements of stent-graft devices as the device diameter is pre-selected by the surgeon based on the artery diameter determined from medical images [5], and, e.g., its sealing properties can only be correctly predicted if the diameter and stiffness of the aorta are well approximated.

In the arterial wall mechanics literature, conflicting statements exist on how maximum stresses in the aortic wall change when accounting for prestresses in model geometries derived from medical images. Lu et al. [114] report that accounting for the correct stress-free reference configuration reduces the maximum stresses predicted in abdominal aortic aneurysms versus classical forward approaches. Using MULF, Gee et al. [29, 30] report that including the effect of prestressing reduces the maximum wall stress in the artery. Speelman et al. [118] also applied the backward incremental method for patient-specific wall stress analyses. They also conclude that accounting for prestress in a simulation increases the maximum wall stress. Raghavan et al. [119] introduced a method to compute the zero-pressure geometry of an arterial aneurysm using the assumption of a consistent deformation field with varying applied pressure. This is a straightforward approximation method, and as such, recovers only an approximation of the desired result. Here also the authors report that a theoretically consistent treatment of the reference configuration results in a reduced estimate for the maximum wall stresses.

In the context of tubular structures like arteries, we demonstrate that a change in maximum wall stress, calculated when comparing classical FE approaches to those accounting for prestresses, depends crucially on changes in the local curvature of the geometry and on how close the initial cross-section is to circular. To this end we present, as an example which accounts for prestressing, an elliptical geometry where we vary the ratio of major to minor axes. We show that for such ratios close to unity the maximum stresses decrease relative to classical FE approaches, while for ratios that differ notably from unity the maximum stresses increase.

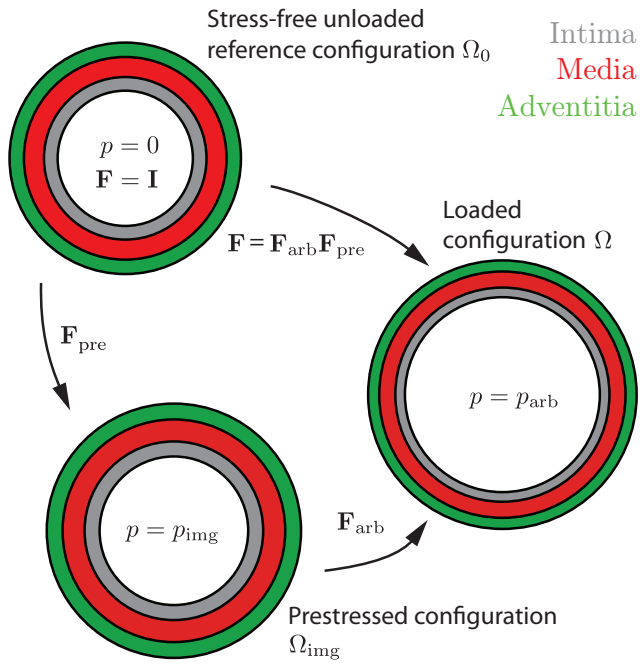

Figure 4.1: Schematic of the different configurations during a prestressing analysis: Ω_0, stress-free and unloaded reference configuration; Ω_{img}, prestressed configuration; Ω, loaded configuration (prestressed configuration with added arbitrary deformation).

4.2 Materials and Methods

4.2.1 Configurations During a Prestressing Analysis

We consider a general boundary-value problem in finite elasticity with respect to a stress-free and unloaded reference configuration $\Omega_0 \subset \mathbb{R}^3$. Figure 4.1 shows the different configurations that occur in a prestressing analysis. The configuration during medical imaging is Ω_{img} and is represented, e.g., by an artery with an inner pressure p_{img} during imaging due to the blood pressure of the patient. The deformation gradient $\mathbf{F}_{\text{pre}}$, in our approach computed, maps the reference configuration Ω_0 on the prestressed configuration Ω_{img}. When $\mathbf{F}_{\text{pre}}$ is known, then configurations with arbitrary loads described by a deformation gradient $\mathbf{F}_{\text{arb}}$ can be computed by the multiplicative decomposition $\mathbf{F} = \mathbf{F}_{\text{arb}}\mathbf{F}_{\text{pre}}$, where $\mathbf{F}$ is the deformation gradient associated with the mapping from the reference configuration Ω_0 to the loaded configuration Ω.

FE codes usually start from the undeformed and stress-free reference configuration Ω_0 and update the displacement $\mathbf{u}$ for each time increment Δt with the displacement increment $\Delta\mathbf{u}$, i.e., $\mathbf{u}_{t+1} = \mathbf{u}_t + \Delta\mathbf{u}$. The subscript $t+1$ (advancing the solution to $t + \Delta t$) denotes values from the current time step, whereas t denotes values with respect to the previous time step. In the suggested prestressing algorithm the incremental update of the displacement is replaced by the incremental update of the deformation gradient.

4.2.2 Determination of the Prestressed State

To compute the deformation gradient $\mathbf{F}_{\text{pre}}$ of the prestressed state, we start our simulation from the configuration $\Omega_{\text{img}} \subset \mathbb{R}^3$ at time t, which corresponds to the geometry obtained from medical imaging. The coordinates of points in this configuration at time t are subsequently denoted by $\mathbf{x}_t$ while coordinates in the stress-free and unloaded reference configuration Ω_0 are denoted by $\mathbf{X}$.

We propose to define the local deformation gradient $\mathbf{F}_t$ at time t as a history variable, initialized as the identity tensor $\mathbf{I}$ at the beginning of the analysis. After each time step, we determine the increment $\Delta\mathbf{u}$ of displacements.

For classical FE formulations, the deformation gradients at the time instants t and $t+1$ are defined as

$$\mathbf{F}_t = \frac{\partial \mathbf{x}_t}{\partial \mathbf{X}} = \mathbf{I} + \frac{\partial \mathbf{u}_t}{\partial \mathbf{X}}, \qquad \mathbf{F}_{t+1} = \frac{\partial \mathbf{x}_{t+1}}{\partial \mathbf{X}} = \mathbf{I} + \frac{\partial \mathbf{u}_{t+1}}{\partial \mathbf{X}}. \tag{4.1}$$

However, for a prestressing analysis, $\mathbf{X}$ is unknown and $(4.1)_2$ has to be reformulated in terms of known quantities, i.e., in terms of $\mathbf{x}_t$. Thus,

$$\mathbf{F}_{t+1} = \frac{\partial \mathbf{x}_{t+1}}{\partial \mathbf{X}} = \frac{\partial \mathbf{x}_{t+1}}{\partial \mathbf{x}_t}\frac{\partial \mathbf{x}_t}{\partial \mathbf{X}} = \frac{\partial \mathbf{x}_{t+1}}{\partial \mathbf{x}_t}\mathbf{F}_t = \left(\mathbf{I} + \frac{\partial \Delta\mathbf{u}}{\partial \mathbf{x}_t}\right)\mathbf{F}_t. \tag{4.2}$$

Now we define the increment of the deformation gradient as

$$\Delta\mathbf{F} = \mathbf{I} + \frac{\partial \Delta\mathbf{u}}{\partial \mathbf{x}_t}, \tag{4.3}$$

see also [30]. When storing $\mathbf{F}_t$ as a history variable, we can then update the deformation gradient according to

$$\mathbf{F}_{t+1} = \Delta\mathbf{F}\mathbf{F}_t. \tag{4.4}$$

Note that the notation differs from the notation used in [30].

Figure 4.2 illustrates the different configurations occurring during the generalized prestressing algorithm. We start from the geometry determined from medial imaging (but without any external load), and hence with the deformation gradient $\mathbf{F} = \mathbf{I}$. At time t we load the artery with pressure $p = p_t$, which we obtain by mapping, with the deformation gradient $\mathbf{F}^t_{\text{pre}}$, from the corresponding unloaded reference configuration Ω^t_0. Advancing one time step, we compute an increment of the displacement $\Delta\mathbf{u}$, from which we determine an increment of the deformation gradient $\Delta\mathbf{F}$. This yields a configuration loaded with $p = p_{t+1}$. To regain the geometry from medical imaging, we set $\Delta\mathbf{u}$ back to zero. Thus the configuration with the geometry from medical imaging and the inner pressure p_{t+1} has a new stress-free reference configuration Ω^{t+1}_0. This configuration deviates from equilibrium by the displacement increment $\Delta\mathbf{u}$ and is marked with an asterisk (*). We repeat this procedure for each time step until we obtain an equilibrium configuration very close to Ω_{img}.

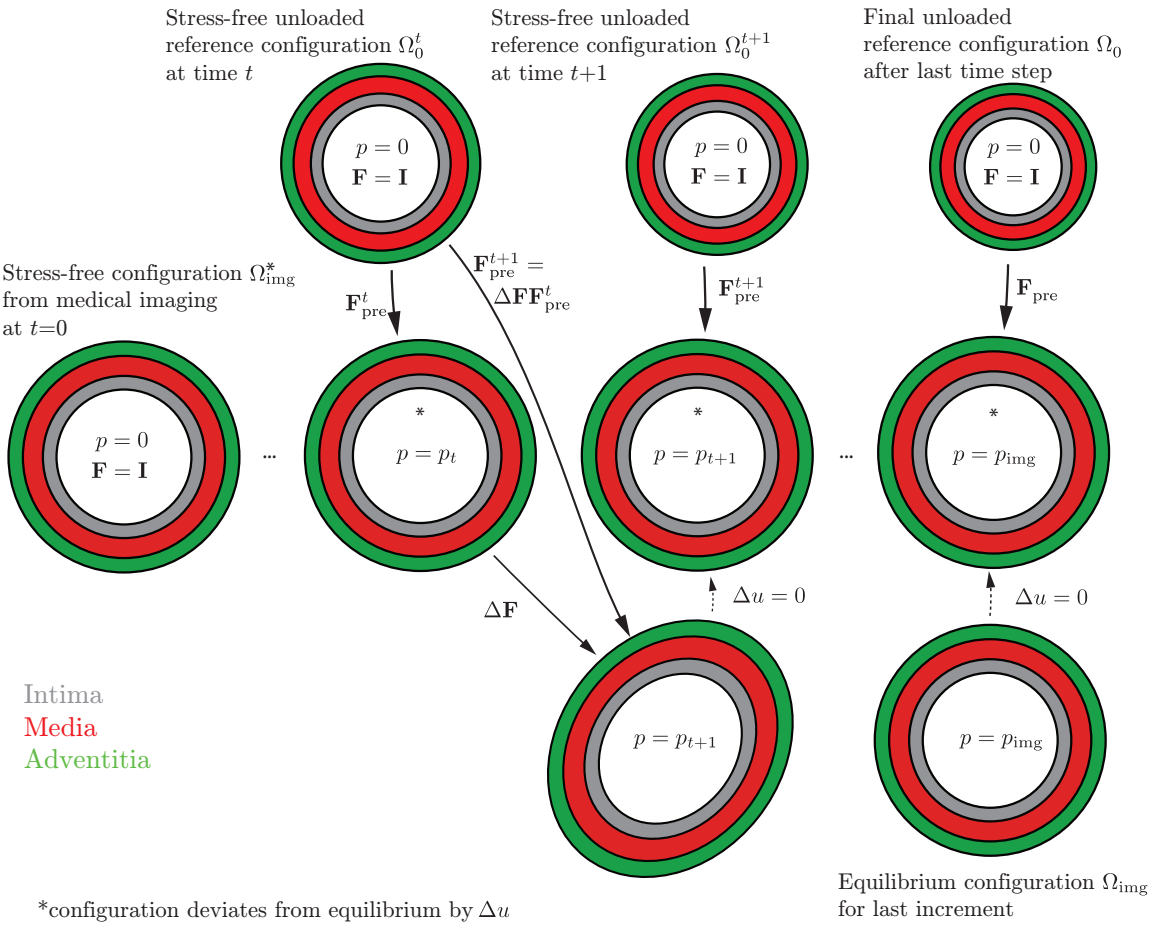

Figure 4.2: Schematic of the generalized prestressing algorithm to include prestress into pre-loaded finite element models. The different configurations with the corresponding external loads that occur during the prestressing computations are shown.

The time steps should be sufficiently small to ensure that Ω_{img} is close to the configuration determined from medical imaging Ω^*_{img} and the inner pressure p_{img}. To assure this, we propose to add load-increment-free time steps at the end of the simulation method.

In our algorithm we define one set of history variables at each Gauss point, i.e. the nine entries of the local deformation gradient, and we do not need to store or update the inverse of the Jacobian mapping. Both the deformation gradient $\mathbf{F}_{t+1}$ and the increment $\Delta\mathbf{F}$ are provided on the element level.

Figure 4.2 also illustrates the drawback of the approach, i.e., that equilibrium is computed in a virtual configuration that does not correspond to the geometry of the imaging data, cf. [30]. Hence, the larger the load increment per time step, the larger the difference between the configuration obtained from imaging and equilibrium configuration. This effect results in a dependence of the solution accuracy on the time step size.

Initialize $\mathbf{F} = \mathbf{I}$; for each time increment Δt from t to $t+1$:
1. Compute $\Delta\mathbf{u}$ from equilibrium
2. Compute $\Delta\mathbf{F}$ from (4.3), cf. (4.7)
3. Read $\mathbf{F}_t$ from history
4. Compute $\mathbf{F}_{t+1}$ from (4.2)
5. Update $\mathbf{F}_t \leftarrow \mathbf{F}_{t+1}$ (write to history)
6. Set $\Delta\mathbf{u} \leftarrow \mathbf{0}$
7. Repeat from 1. for $t \leftarrow t+1$

Table 4.1: Computation of the prestressed deformation gradient within the generalized prestressing algorithm.

4.2.3 Implementation Details

In a standard FE implementation the discrete position $\mathbf{x}$ and the discrete deformation field $\mathbf{u}$ are approximated as

$$\mathbf{x} = \sum_{i=1}^{n_\mathrm{e}} N_i(\boldsymbol{\xi})\mathbf{x}_i, \qquad \mathbf{u} = \sum_{i=1}^{n_\mathrm{e}} N_i(\boldsymbol{\xi})\mathbf{u}_i, \tag{4.5}$$

where $N_i(\boldsymbol{\xi})$ are shape functions, $\boldsymbol{\xi}$ are the natural coordinates of the element, $\mathbf{x}_i$ are (spatial) nodal positions, $\mathbf{u}_i$ are nodal displacements and n_e is the number of nodes per element. In (4.3), we require differentiation of the displacement increment $\Delta\mathbf{u}$ with respect to the current spatial configuration $\mathbf{x}_t$; this is given as

$$\frac{\partial \Delta\mathbf{u}}{\partial \mathbf{x}_t} = \Delta\mathbf{u}_i \frac{\partial N_i(\boldsymbol{\xi})}{\partial \mathbf{x}_t} = \Delta\mathbf{u}_i \frac{\partial N_i(\boldsymbol{\xi})}{\partial \boldsymbol{\xi}} \frac{\partial \boldsymbol{\xi}}{\partial \mathbf{x}_t}, \tag{4.6}$$

where summation is implied over the repeated index. Hence we may rewrite (4.3) as

$$\Delta\mathbf{F} = \mathbf{I} + \Delta\mathbf{u}_i \frac{\partial N_i(\boldsymbol{\xi})}{\partial \boldsymbol{\xi}} \frac{\partial \boldsymbol{\xi}}{\partial \mathbf{x}_t}. \tag{4.7}$$

We complete this computation immediately after the computation of $\Delta\mathbf{u}$ (and thus $\Delta\mathbf{u}_i$) since the coordinates $\mathbf{x}_t$ correspond to the imaged configuration, and thus we know all terms on the right-hand-side of (4.7). Note that (4.7) corresponds to (39) in [30] where $\partial\boldsymbol{\xi}/\partial\mathbf{x}_t$ is denoted as the inverse Jacobian $\mathbf{J}_t^{-1}$. We summarize the implementation details for the generalized prestressing algorithm in Table 5.1. All necessary modifications to a standard FE code can be accomplished at the element level.

At the end of the prestressing computation we obtain a distribution of deformation gradients for the prestressed state corresponding to $\mathbf{F}_\mathrm{pre}(\mathbf{x})$ for each Gauss point in the FE mesh. We implement the GPA as a custom user defined element in the FE code FEAP (University of California at Berkeley).

4.2.4 Forward Simulation Based on Prestressed State

From the prestressed geometry, e.g., the *in vivo* geometry in equilibrium with the *in vivo* loads, we can apply arbitrary loads to study boundary-value problems of interest. We define $\mathbf{F}_{\text{arb}}$ as an arbitrary deformation gradient associated with such arbitrary loads. From the prestressed state, we compute the deformation and the stresses using the overall deformation gradient as

$$\mathbf{F}(\mathbf{x},t) = \mathbf{F}_{\text{arb}}(\mathbf{x},t)\mathbf{F}_{\text{pre}}(\mathbf{x}). \tag{4.8}$$

In practice, we compute the deformation gradient $\mathbf{F}(\mathbf{x},t)$ in (4.8) using two steps. First, we compute the deformation gradient describing the prestressed state $\mathbf{F}_{\text{pre}}(\mathbf{x})$ for each Gauss point using a custom GPA element, and we write out this distribution as a history file. Next, we perform a classical forward computation with a standard element from the prestressed configuration, and the deformation gradient computed here under arbitrary loading $\mathbf{F}_{\text{arb}}(\mathbf{x},t)$ is multiplied by the deformation gradient describing the prestressed state $\mathbf{F}_{\text{pre}}(\mathbf{x})$ to obtain the final solution $\mathbf{F}(\mathbf{x},t)$. We solved all of the following examples using the Newton-Raphson algorithm implemented in FEAP.

4.3 Numerical Examples

4.3.1 Unit Cube Test

In this section we present results from testing an incompressible unit cube meshed with one solid mixed element (Q1P0). We assume that the cube in the unloaded configuration has dimensions $a \times a \times a$ with $a = 1\,\text{mm}$, which corresponds to the geometry used for the classical forward computation of the solution, see Fig. 4.3(a). We use a compressible neo-Hookean model, with a shear modulus of 1 MPa, and a penalty term that is used to accommodate the incompressibility condition numerically. To achieve large deformations we apply a force of $P = 4\,\text{N}$. The load increment for each time step n is $\Delta P_n = P/N$, where N is the total number of time steps.

Solving the system of equations analytically we arrive at $\sigma = 16.24\,\text{MPa}$ for the Cauchy stress in the direction of loading, with a corresponding stretch of $\lambda = 4.061$. In the two directions transverse to the loading axis, the stretch is $\lambda = 0.496$ (the Cauchy stress is zero). The final equilibrium geometry is thus $b \times c \times c$, with $b = 4.061\,\text{mm}$ and $c = 0.496\,\text{mm}$, which corresponds to the geometry used as input for the GPA, see Fig. 4.3(b).

In Fig. 4.4(a), we investigate the error in the stress prediction versus the number of time steps by comparing the result from the GPA to the corresponding result from the forward computation. For $N = 10^1$ and $N = 10^2$ the errors are reasonable for practical applications, 2.5% and 0.5% relative error, respectively (for $N = 5$ the error is 86% and for $N = 1$ no solution was found using the GPA). At $N = 10^3$ almost no deviation in the result is observable. A close-up of Fig. 4.4(a) is given in Fig. 4.4(b), which shows that the solutions of the GPA converge to the analytical solution.

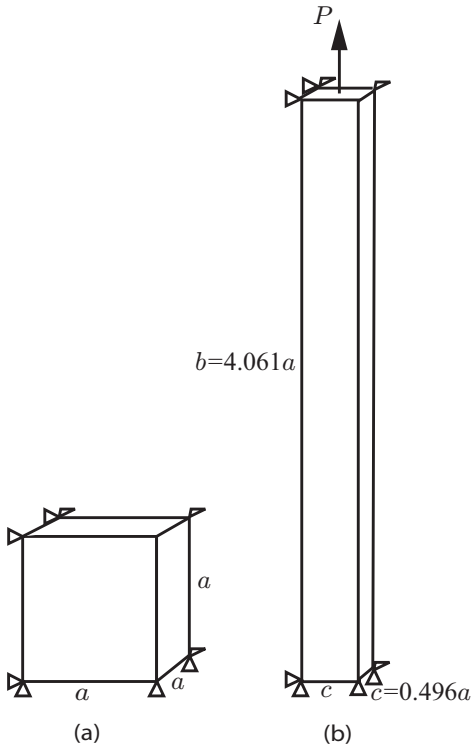

Figure 4.3: Configurations for a single element test of the Generalized Prestressing Algorithm (GPA): (a) unloaded reference configuration of a unit cube; (b) deformed configuration in equilibrium with $P = 4\,\mathrm{N}$, illustrating the large deformation. The classical forward computation starts from (a) and is in equilibrium at (b), while the GPA uses only configuration (b) to estimate the same stress/strain state.

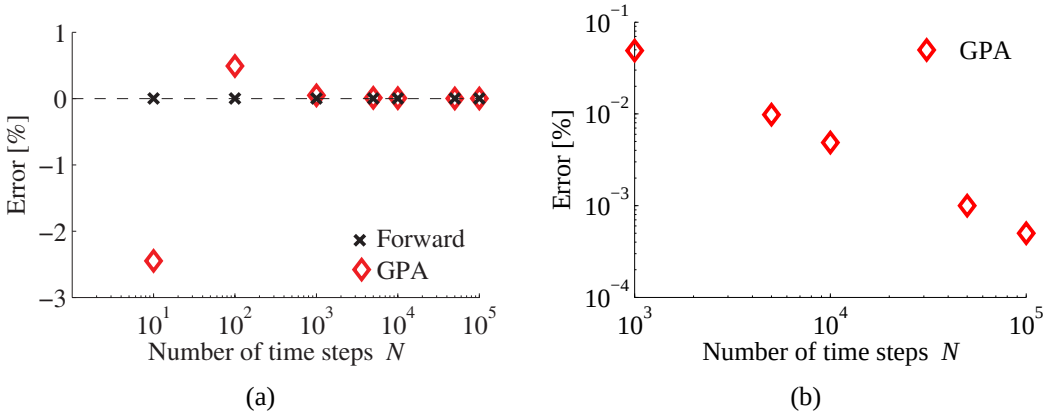

Figure 4.4: Error in the stress prediction calculated using the analytical solution versus the number of time steps N: (a) comparison of the classical forward computation with the Generalized Prestressing Algorithm (GPA); (b) detail of (a) to demonstrate the GPA convergence for a sufficiently high number of time steps.

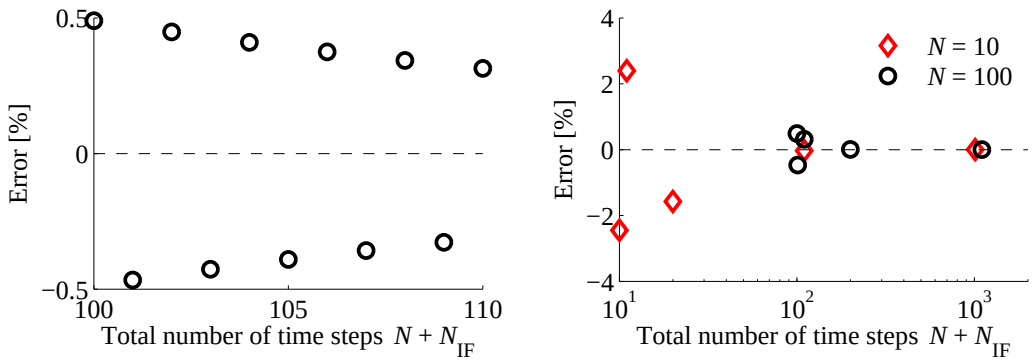

Figure 4.5: The effect of adding load-increment-free time steps to the end of a Generalized Prestressing Algorithm (GPA) computation: (a) the first ten load-increment-free time steps N_{IF} show an oscillation of the error between negative and positive values, however the magnitude of the error decreases with the number of time steps; (b) the error for a total number of time steps after applying the load with the GPA using $N = 10$ and 100 load steps and adding $N_{\mathrm{IF}} = 1$, 10, 100 and 1000 load-increment-free time steps.

Noting that the solution for a given load depends on the number of time steps used to achieve that load, we investigate the possibility of minimizing the error by adding load-increment-free time steps N_{IF} at the end of the GPA simulations. In Fig. 4.5(a) we start with $N = 100$ GPA time increments to apply the load, and then include up to ten load-increment-free time steps N_{IF}. The magnitude of the error decreases with each additional time step, however, there is an oscillation between a positive and a negative error.

In Fig. 4.5(b) we start with both $N = 10$ and $N = 100$ GPA time increments to apply the load, and then include $N_{\mathrm{IF}} = 1$, 10, 100 and 1000 load-increment-free time steps. Results for the same total number of time steps differ depending on the partitioning of the number of time steps with and without load increments, e.g., the error for a total of 110 time steps is 0.31% using $N + N_{\mathrm{IF}} = 100 + 10$ load steps while the error is only 0.03% using $N + N_{\mathrm{IF}} = 10 + 100$ load steps.

4.3.2 Representative Patient-Specific Model of a Thoracic Aorta

To demonstrate the applicability of our algorithm to larger problems, we simulate various *in vivo* conditions of a human thoracic aorta using a realistic fiber-reinforced material model, and parameters which are based on experimental data. We use a representative patient-specific geometry (male, 62 yrs) obtained from segmenting MRI data, and a finite element mesh using a custom meshing algorithm [120]. Briefly, the edges of the inner and outer aortic wall are segmented from the imaging data. We first divided the resulting volume into slices in the axial direction, and then these slices are divided into sections in the circumferential direction. The resulting mesh contains 23040 mixed eight-node brick elements (P1Q0). We used thickness ratios of $0.18/0.46/0.36$ to define the three arterial tis-

sue layers (intima/media/adventitia, respectively) as previously determined by experiment [93]. Atherosclerotic plaques are neglected in the example and therefore not modeled.

We mesh each layer of the thoracic tissue with four elements through the thickness in order to resolve radial stress gradients. The interfaces between the layers are considered to be bonded.

To generate a representative numerical test case we assume that this geometry is a stress-free and unloaded configuration, and we complete a classical forward computation using an inner pressure of $p = 85\,\text{mmHg}$, i.e. $11.33\,\text{kPa}$, which corresponds to the diastolic pressure *in vivo* (we will refer to this as case I). To test the GPA performance we compare the solution of case I to the GPA solution (case IIa); this solution uses the deformed geometry of the aorta computed in case I (at $p = 85\,\text{mmHg}$) as the initial geometry. To compute these solutions we use $N = 17$ time steps for both cases. To show that additional load-increment-free time steps reduce error we repeat the computation of case IIa with 83 additional N_{IF} time steps after the pressure of $p = 85\,\text{mmHg}$ is reached (case IIb). To study convergence properties of the GPA in more detail, we also calculate and compare several error measures for GPA solutions generated using various combinations of standard time steps plus load-increment-free time steps. To compare differences in the deformation and stress distributions resulting from a theoretically consistent calculation (versus the test cases I and IIa and IIb) we also use the GPA to calculate a solution using the medical imaged geometry as starting point (case III).

We describe the three tissue layers of the aorta using a hyperelastic material model considering dispersion of the collagen fibers [39]. The isochoric part of the deformation is captured by the strain-energy function

$$\overline{\Psi} = \frac{\mu}{2}(\overline{I_1} - 3) + \sum_{i=4,6} \frac{k_1}{2k_2} \left\{ e^{k_2[\kappa \overline{I_1} + (1-3\kappa)\overline{I_i} - 1]^2} - 1 \right\}, \tag{4.9}$$

where μ represents the initial shear modulus of the non-collagenous matrix, k_1 is a stress-like parameter, k_2 is a dimensionless parameter, $\overline{I_1}$ is the trace of the isochoric right Cauchy-Green tensor $\overline{\mathbf{C}}$, [25], and $\kappa \in [0, 1/3]$ is a dimensionless parameter describing distributed collagen fiber orientations.

We assume that two families of collagen fibers are oriented in the plane of the tissue, where $i = 4$ relates to one fiber family and $i = 6$ to the other. The pseudo-invariants $\overline{I_4} = \overline{\mathbf{C}} : \mathbf{M} \otimes \mathbf{M}$ and $\overline{I_6} = \overline{\mathbf{C}} : \mathbf{M}' \otimes \mathbf{M}'$ correspond to the square of the stretches of the fibers in the fiber directions [7]. The vectors $\mathbf{M}$ and $\mathbf{M}'$ denote the mean directions of the collagen fibers in the reference configuration. The fibers are assumed to be symmetrically oriented with respect to the circumferential direction of the artery, and thus both $\mathbf{M}$ and $\mathbf{M}'$ are uniquely defined by the structural parameter φ, which defines the angle between the circumferential direction of the artery and the fiber direction. The mean directions of the fiber reinforcement

Layer	μ [MPa]	k_1 [MPa]	k_2 [-]	φ [°]	κ [-]
Intima	0.034	4.3	13.3	46.5	0.20
Media	0.028	0.14	11.9	38.4	0.21
Adventitia	0.020	0.39	6.79	52.3	0.23

Table 4.2: Median constitutive parameters for intima, media and adventitia of the human thoracic aorta; adopted from [93].

are input at the element level using an approach similar to that of Kiousis et al. [121] implemented in MATLAB (2009b, The MathWorks, Inc., Massachusetts, United States). We use material parameters associated with the hyperelastic response taken from our previous work, as summarized in Table 5.2, [93].

As mentioned, we subject the inner wall of the artery to a pressure of $p = 85\,\text{mmHg}$. Displacements in the z-direction (along the main axis of the aorta) are constrained at nodes on the cutting planes. Furthermore, on the same cutting planes, we suppress the displacement tangential to the main axis at the nodes on the luminal side of the aortic segment. Without loss of generality, axial prestretch is neglected in the scope of these numerical examples, but it can easily be included if desired, cf. e.g., the boundary conditions of Kiousis et al. [121]. By qualitatively comparing the results of the forward calculation with the GPA the stress values and the stress distributions are virtually identical. Figure 4.6(a) compares the distribution of the principal Cauchy stresses through the wall thickness for case I (crosses) and case IIa (diamonds), i.e., of the forward and the GPA computations, respectively. Figure 4.6(b) shows the percent error of the first principal Cauchy stress for the GPA with $N = 17$ (diamonds) and $N + N_{\text{IF}} = 17 + 83$ (circles), i.e., 83 additional load-increment-free time steps. The errors decrease notably with the inclusion of additional N_{IF}.

In Table 4.3 we investigate the accuracy of the GPA solution for various solution approaches. Therein, the total number of time steps is $N + N_{\text{IF}}$, the total number of Newton iterations is NI, the maximum value of the first principal stress in the entire segment is $\sigma_1^{\max}$, the absolute and relative error of $\sigma_1^{\max}$ with respect to the forward computation are $e_{\text{a}}(\sigma_1^{\max})$ and $e_{\text{r}}(\sigma_1^{\max})$, respectively, and the average magnitude of the absolute error is $e_{\text{m}}(\sigma_1)$.

For our patient-specific segment of the thoracic aorta, 12 equally-sized time steps are required to generate a solution in equilibrium with $p = 85\,\text{mmHg}$ internal pressure. Even for $N + N_{\text{IF}} = 12 + 0$ the GPA provides a reasonable solution with the absolute and relative error of $\sigma_1^{\max}$ of $e_{\text{a}}(\sigma_1^{\max}) = 5.54\%$ and $e_{\text{r}}(\sigma_1^{\max}) = 1.87\%$, respectively. Focusing on the effect of load-increment-free time steps N_{IF} specifically, we see that for our representative example $N + N_{\text{IF}} = 100 + 0$ total time steps provides a modestly better result than $N + N_{\text{IF}} = 17 + 83$ time steps, but requires almost twice the number of Newton it-

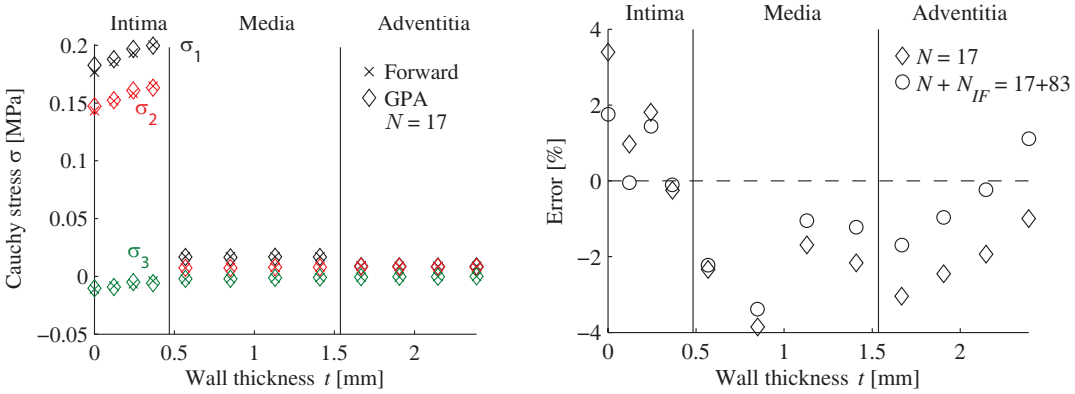

Figure 4.6: Representative comparisons of the Cauchy stress distributions through the wall thickness of the patient-specific thoracic aorta: (a) classical forward (case I, crosses) and the Generalized Prestressing Algorithm (GPA) (case II, diamonds) computations, both with $N = 17$ time steps; (b) percent error (with respect to the forward calculation) of the first principal Cauchy stress estimated using the GPA for $N = 17$ and for $N + N_{\mathrm{IF}} = 17 + 83$ time steps.

$N + N_{\mathrm{IF}}$ [–]	NI [–]	$\sigma_1^{\max}$ [kPa]	$e_{\mathrm{a}}(\sigma_1^{\max})$ [kPa]	$e_{\mathrm{r}}(\sigma_1^{\max})$ [%]	$e_{\mathrm{m}}(\sigma_1)$ [%]
12+0	53	434.1	25.5	5.54	1.87
17+0	71	436.1	23.5	5.11	1.68
17+83	195	438.8	20.8	4.53	1.43
100+0	385	440.1	19.5	4.24	1.40
100+17	435	440.5	19.1	4.16	1.38
200+0	742	440.5	19.1	4.16	1.38
1000+0	3002	440.8	18.8	4.09	1.37

Table 4.3: Representative accuracy of the generalized prestressing algorithm for various solution approaches: total number of time steps $N + N_{\mathrm{IF}}$, total number of Newton iterations NI, maximum value of the first principal Cauchy stress in the entire segment $\sigma_1^{\max}$, absolute and relative error of $\sigma_1^{\max}$ with respect to the forward computation, $e_{\mathrm{a}}(\sigma_1^{\max})$ and $e_{\mathrm{r}}(\sigma_1^{\max})$, respectively, and average magnitude of the absolute error $e_{\mathrm{m}}(\sigma_1)$.

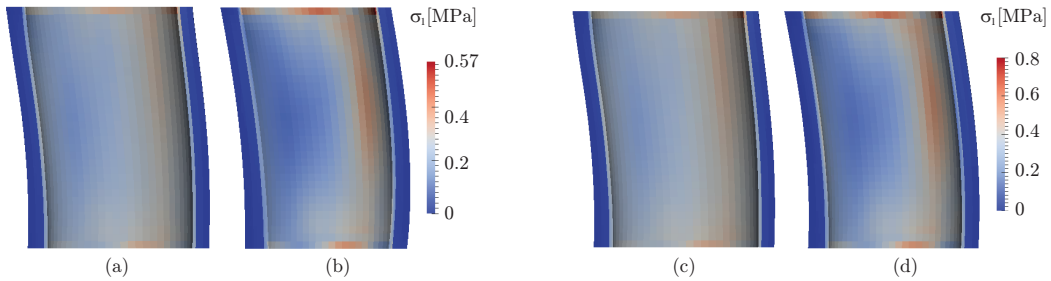

Figure 4.7: Comparison of the first principal Cauchy stress (circumferential stress) generated for a test case on a representative patient-specific thoracic aorta: (a) conventional forward calculation from the imaged geometry up to $p = 85\,\text{mmHg}$ (case I); (b) Generalized Prestressing Algorithm (GPA) computation from the imaged geometry up to $p = 85\,\text{mmHg}$ (case III); (c) conventional forward calculation from the imaged geometry up to $p = 120\,\text{mmHg}$; (d) GPA computation from the imaged geometry up to $p = 85\,\text{mmHg}$ (case III) with a subsequent forward calculation from $p = 85\,\text{mmHg}$ up to $p = 120\,\text{mmHg}$. The stress distributions are very similar. Note that the relatively high stresses near the cutting planes are effects related to the boundary conditions and should not be considered physiologically relevant.

erations to find this solution, thus greatly increasing the computational cost. Conversely, we can match the solution error generated using $N + N_{\text{IF}} = 200 + 0$ total time steps using instead $N + N_{\text{IF}} = 100 + 17$ time steps, which reduces to nearly half the number of Newton iterations required to find this solution.

To compare differences in the deformation and stress distributions resulting from a theoretically consistent calculation (versus the test cases I and IIa and IIb) we also use the GPA to calculate a solution using the medical imaged geometry as starting point. Here we perform two sets of simulations for comparison: the classical forward computation from the imaged geometry to both $p = 85\,\text{mmHg}$ (case I) and $p = 120\,\text{mmHg}$ (15.999 kPa); and the GPA simulation from the imaged geometry to $p = 85\,\text{mmHg}$ (case III) and then a consistent forward simulation from this GPA result up to $p = 120\,\text{mmHg}$ ($\Delta p = 35\,\text{mmHg}$).

Figures 4.7(a) and (b) compare the first principal Cauchy stress distributions for an inner pressure of $p = 85\,\text{mmHg}$ of a conventional forward computation (a) with the GPA computation starting on the imaged geometry (b). Figures 4.7(c) and (d) compare the stress distribution at $p = 120\,\text{mmHg}$ for the forward computation (c) and for the GPA computation to $p = 85\,\text{mmHg}$ followed by a forward computation from $p = 85\,\text{mmHg}$ to $p = 120\,\text{mmHg}$ (d). Note that the relatively high stresses near the cutting planes are effects related to the boundary conditions and should not be considered physiologically relevant.

In both comparisons (Figures 4.7(a) versus (b), and (c) versus (d)) the stress distributions are very similar, however, the minima and maxima are further apart in the GPA solutions. The magnitude of the first principal Cauchy stress marginally increases in the GPA solutions, due in part to the larger local curvature. We note a significant difference in the results from the forward and the GPA computations in the inner diameter of the aorta at both di-

astolic (85 mmHg) and systolic blood pressure (120 mmHg). At diastole the values of a representative diameter for the forward and GPA computations are 22.1 mm and 20.1 mm, respectively, while at systole the corresponding values are 22.6 mm and 20.5 mm. Such results correspond to an overestimation in the inner aortic diameter of approximately 10% if prestressing the model is ignored.

4.3.3 Elliptical Cross-Section Resulting in Varying Local Curvature

To study the effect of prestressing on the calculated stresses within the aortic wall, we build a simple parameterized FE model. Because we suspect that local curvature has a major influence, the model has an elliptical cross-section, and thus a varying local curvature, with the major axis a and the minor axis b. In the limiting case ($a = b$) we obtain a circle. The wall thickness is constant along the circumferential direction as well as along the axial direction of the idealized aortic segment.

Using symmetry we model one quarter of the ellipse with one layer of elements in the axial direction, seven elements in radial direction and 25 elements circumferentially along the 90° segment. In addition to the symmetry boundary conditions, we allow free movement in the axial direction. We use a quasi-incompressible neo-Hookean material model with an initial shear modulus $\mu = 1\,\text{MPa}$ and a bulk modulus $K = 100\,\text{MPa}$. Starting from zero, we increase the inner pressure up to $p = 10\,\text{kPa}$.

We use this model to perform two representative simulations: (i) the correct computation of the stresses (including prestress), case I, and (ii) neglecting the prestress (assuming that the geometry was obtained from medical images, case II. For the case I we compute the stresses at 10 kPa for a range of $a : b$ ratios. Note, if we started from the configuration deformed under $p = 10\,\text{kPa}$, and applied $p = 10\,\text{kPa}$ using the GPA algorithm, we would end with the same result. For the case II we use the deformed configuration of case I as the initial configuration and, subsequently, we apply a pressure of 10 kPa. Hence, the initial configuration of case II corresponds to a geometry determined from medical images. Case II corresponds to results of a computation performed without accounting for prestresses in the aorta. Note that in this example the prestressing algorithm is not used but a conventional FE analysis is performed from two different reference configurations. As regards the aortic simulations, the initial configuration of case I corresponds to Ω_0^t in Fig. 4.2, while the initial configuration of case II corresponds to Ω_{img}^*. To assess the influence of the local curvature, we vary the ratio of the minor and major axis $a : b$, with $a = 1 + \Delta d$ and $b = 1 - \Delta d$ with $\Delta d = 0, 0.05, 0.1, 0.2, 0.3, 0.4, 0.5, 0.6\,\text{mm}$, where $\Delta d = 0$ generates a circle.

Figure 4.8 illustrates the change in both maximum and mean first principal stress σ_1 versus Δd. For the simulation with the circular cross-section both the average and the mean stress decrease when accounting for prestress, and hence the diagram in Fig. 4.8 shows negative values. As the eccentricity of the model increases (increasing ratio of major to minor axis) but Δd remains less than 0.4, the maximum stress increases while the average

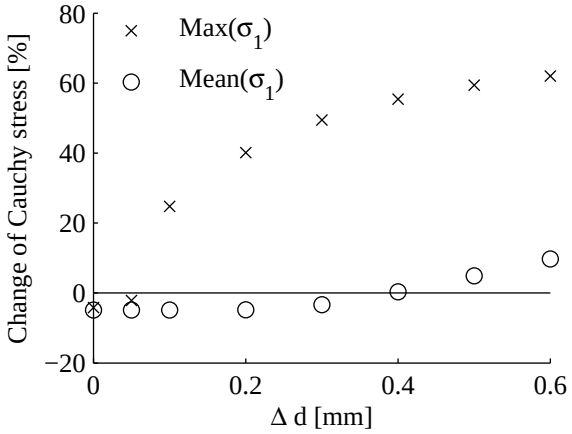

Figure 4.8: Change in maximum and average first principal Cauchy stress σ_1 between omitting and considering prestress in an elliptical cross-section with minor and major axis $a : b$, with $a = 1 + \Delta d$ and $b = 1 - \Delta d$ ($\Delta d = 0$ corresponds to a circular cross-section, $a : b$ equals unity).

stress decreases when accounting for prestress. Above $\Delta d = 0.4$, both average and mean stress increase when accounted for prestress.

Figure 4.9 illustrates the first principal Cauchy stress σ_1 for the extreme case of $\Delta d = 0.6$. The Figures 4.9(a) and (b) illustrate case I at 0 kPa and at 10 kPa respectively, while the Figures 4.9(c) and (d) show the corresponding information for case II. The configuration in Fig. 4.9(a) clearly shows the higher local curvature for the reference configuration of case I. The reference configuration for case II has the same geometry as the deformed configuration for case I, and thus a much lower local curvature.

The high stress gradient in case I results from bending stresses. Due to the applied inner pressure the ellipse wants to deform towards a circle. Thus, at the position of highest local curvature the ellipse bends open. These bending stresses are greatly reduced in case II because the ratio of major and minor axis is much lower in the initial configuration.

4.4 Discussion

4.4.1 Unit Cube Test

Results from the unit cube test (Section 4.3.1) demonstrate that the accuracy of the method depends on the size of the load increment per time step. This effect results from the fact that equilibrium is computed in a virtual configuration determined by the displacement increment $\Delta\mathbf{u}$ which acts on the imaged geometry. Thus, the smaller the load increment per time step, the smaller $\Delta\mathbf{u}$, and hence the smaller the error resulting from the 'wrong' configuration on which the equilibrium is fulfilled.

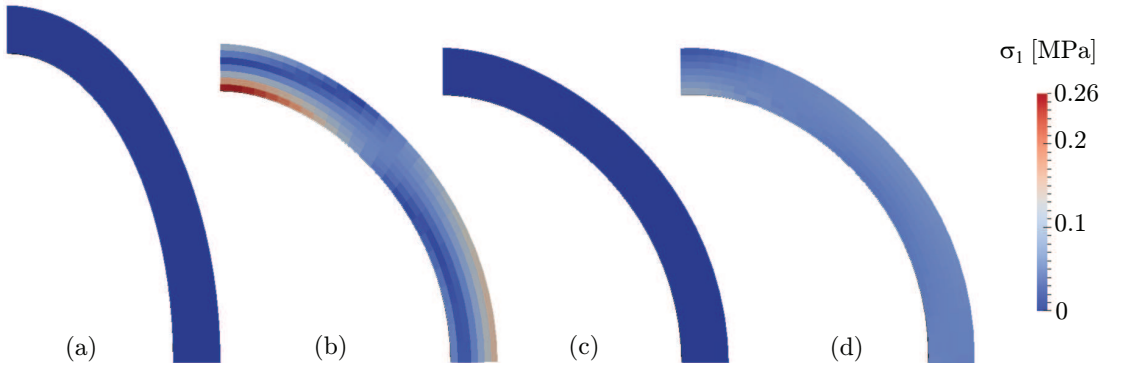

Figure 4.9: Stress distributions in the elliptical cross-section ($\Delta d = 0.6$) for (a) case I at $p = 0\,\text{kPa}$, (b)case I at $p = 10\,\text{kPa}$, (c) case II at $p = 0\,\text{kPa}$ and (d) case II at $p = 10\,\text{kPa}$. The high stress gradient in case I results from bending stresses when the elliptical cross-section deforms towards a circle. Bending stresses in case II are much lower because the ratio of major to minor axes is lower in the stress-free reference configuration.

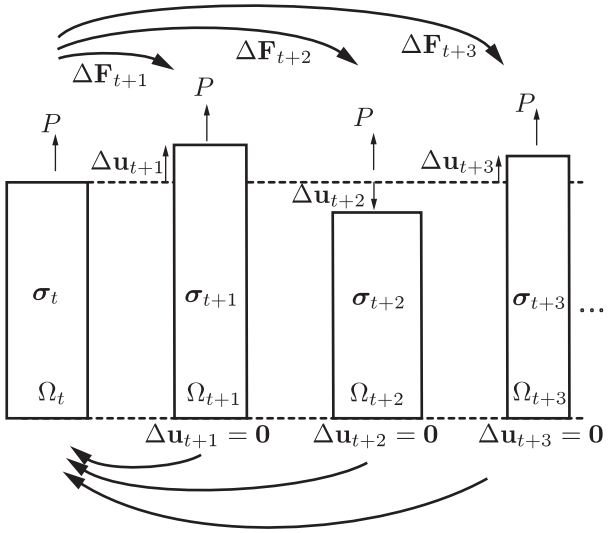

Figure 4.10: Oscillation of the error while using load-increment-free time steps N_{IF} with the generalized prestressing algorithm.

The oscillation in Fig. 4.5(a) can be explained by studying the difference between the configuration Ω_{t+1} on which the equilibrium is fulfilled, and the configuration Ω_t for which we seek a final solution. For clarity, consider, for example, the uniaxial extension of a unit cube, as shown in Fig. 4.10. Assume a standard application of the GPA results in an equilibrium stress/strain distribution after the final time step of load application on the configuration Ω_{t+1} in Fig. 4.10, and the tensile Cauchy stress in this configuration to be $\boldsymbol{\sigma}_{t+1}$.

The deformation is larger in Ω_{t+1} than in Ω_t, hence $\sigma_{t+1} > \sigma_t$, where σ_t is the exact solution for the stress in configuration Ω_t, and thus the result we seek. Before the first load-increment-free time step is computed, the configuration Ω_{t+1} is set back to Ω_t, i.e., $\Delta\mathbf{u}_{t+1} = \mathbf{0}$, but the deformation gradient (in the history) remains the same. In this case, the stress value remains σ_{t+1} and is, therefore, overestimated. In an effort to better approximate equilibrium under the constant load P the geometry must change to the configuration Ω_{t+2} in the next load-increment-free time step. Once the geometry is set back to the imaged configuration, the stress in Ω_t is underestimated. For the next load-increment-free time step Ω_{t+3} the cube must now extend to better approximate equilibrium. This oscillation of the solution proceeds while the magnitude of the error decreases monotonically until the solution converges within an acceptable tolerance. Note that the stress estimated in configuration Ω_t oscillates at each time step (even though the load is constant) because the implied unloaded reference configuration changes for each time step when the displacement is set back to zero.

It is important to regard two different aspects of solution convergence when discussing convergence of the generalized prestressing algorithm. First is the convergence of the solution for the iterations of each time step. This convergence is not affected by the GPA, and hence is the same for a given material model using a conventional forward or a GPA computation. Second is the convergence of the stress distribution for the deformed geometry Ω_t (cf. Fig. 4.4) to the exact solution. This convergence depends on the size of the time step and on the number of additional load-increment-free time steps. For a given convergence tolerance, results in Fig. 4.5(b), and Table 4.3, imply it is computationally less expensive to use relatively few time steps for application of the load and add load-increment-free time steps to the solution, than to use the equivalent number of time steps only for application of the load.

4.4.2 Patient-Specific Model of a Thoracic Aorta

Focusing now on the representative test case of the patient-specific thoracic aorta model (Section 4.3.2), agreement between the results from the classical forward computation (case I) and from the GPA calculated entirely on the corresponding deformed configuration (case IIa), as shown in Fig. 4.6, is very good, even when using the same number of time steps (relatively few) for both computations. Adding load-increment-free time steps decreases the solution error, but increases the computational cost. Therefore, it is necessary to find a good compromise between accuracy and computational cost, which depends strongly on the problem to be solved. Table 4.3 shows that the inclusion of load-increment-free time steps yields a similar accuracy for the same total number of time steps while reducing the computational cost, i.e., the number of Newton iterations is drastically reduced.

When initiating simulations from the correct imaged geometry, there is a difference in the stress distributions and especially in the maximum stresses between the forward computation (case I) and the GPA computation (case III), as shown in Fig. 4.7. Our results indicate

the inclusion of prestressing on patient-specific simulations increases both the distribution and maximum of the first principal Cauchy stress. We postulate that this effect is due to larger local curvatures in the imaged geometry versus the deformed geometry of the classical forward computation.

The significant difference between the classical forward (case I) and the GPA computations (case III) for the predicted inner diameter of the aorta, at both diastolic and systolic blood pressure, is due to the relatively low stiffness of the arterial tissue at relatively low stress, cf. [80]. A correct prediction of the diameter is especially important for modeling clinically relevant problems, e.g., surgical procedures such as stent-graft placement for thoracic or abdominal aneurysm repair. In such interventions the diameter of the stent is selected before the procedure begins, based on the diameter of the aorta but oversized by approximately 10 to 20% to insure adequate sealing [5]. Thus overestimating the inner diameter of the aorta by approximately 10% could lead to severe misinterpretations of the simulation results.

4.4.3 Influence of Prestress on Stress Distribution

Our results demonstrating increased stresses in the patient-specific model when accounting for prestresses are consistent with those reported by De Putter et al. [117] and Speelman et al. [118]. Both conclude that accounting for prestress in the patient-specific FE simulations leads to an increase in the maximum arterial wall stress. Raghavan et al. [119] report that their approximate, but theoretically consistent treatment of the reference configuration results in a reduced estimate for the maximum wall stresses. However, the result depends on the assumption of a consistent deformation field within the arterial aneurysm under varying applied pressure; thus changes in local curvature under finite deformation are neglected. Interestingly, both Lu et al. [114] and Gee et al. [29, 30] report that accounting for the correct stress-free reference configuration reduces the maximum stresses predicted in abdominal aortic aneurysms with respect to the use of a classical formulation.

In view of our example with a parameterized elliptical cross-section (Section 4.3.3), the contradiction of changes in stress distributions may result from different geometries used in the examples. When the geometry deviates from a circle, naturally, the local curvature inside the aortic model changes. When a distorted circular cross-section geometry, such as the ellipse, is inflated, the inner pressure tends to deform the distorted geometry towards a circle. This induces bending stresses and the maximum and average stresses increase in proportion to the enforced amount of bending.

As stresses resulting from bending motion play a role in the stress distribution, the transmural stress distribution should be resolved with an appropriate number of elements through the thickness of the arterial wall.

4.4.4 Limitations

As stated by Gee et al. [30], a major disadvantage is that equilibrium is not achieved on the *in vivo* configuration but in a configuration that deviates from the *in vivo* configuration by the increment of the deformation gradient $\Delta\mathbf{F}$. However, in two examples we show that our solution using the GPA from the deformed configuration converges to the solution obtained from a classical forward computation. Load-increment-free time steps at the end of the computation only account for the differences between the desired equilibrium on the imaged geometry and the obtained equilibrium on the virtual geometry. The method can be used on arbitrary geometries. However, it is only applicable to derive stress distributions in loaded geometries provided that the material can be modeled with a path-independent material law.

Regarding the example of the patient-specific model, the values of the stresses in Fig. 4.7(b) specifically, the maximum first principal stress reported in the simulation at diastole ($p = 85\,\mathrm{mmHg}$) is relatively large. However, the maximum values of the stress appear near the cutting planes at the upper and lower ends of the aortic section and are attributed to boundary effects. These should not be considered physiologically relevant. The maximum and mean first principal stresses near the center of the section simulated are approximately $\sigma_1 = 0.3\,\mathrm{MPa}$ and $\sigma_1 = 0.1\,\mathrm{MPa}$, respectively. These stress values are within the range reported by Holzapfel et al. [7] for aortic tissue.

Furthermore, the stresses reported for the intima are notably higher than the stresses in the media and the adventitia. This result is not likely from the physiological point of view because the tissue is known to be residually stressed *in vivo* [24]. Including the effect of residual stresses into our modeling framework would generally tend to homogenize our results across the layers, as the intima is under compression and the media and adventitia are under tension in the three-layer composite tissue *in vivo* [24]. Furthermore, large opening angles may lead to an increase in circumferential and longitudinal stresses towards the outer radius of the aortic wall [122]. Hence, to obtain a plausible result for the stress prediction in three-layer patient-specific models of the aorta, residual stresses need to be included in future work. This topic lies outside the scope of the current paper, and hence was not pursued further.

4.5 Conclusion

We present a Generalized Prestressing Algorithm (GPA) for finite element simulations of general pre-loaded geometries. Relative to available formulations of a similar nature, our algorithm is applicable to FE formulations based on total Lagrangian or updated Lagrangian formulations. A disadvantage of the GPA is that we enforce equilibrium in a virtual, non-existent configuration, and this may lead to errors in the stress prediction. This disadvantage can be overcome by decreasing the load increment per time step, or by adding additional load-increment-free time steps at the end of a simulation. We demonstrate the

accuracy of the GPA using both a unit cube under uniaxial tension and a patient-specific model of a thoracic aorta including a realistic anisotropic material model for the arterial wall. Our results show very good agreement with corresponding results from a classical forward computation and demonstrate that the solution error can be made arbitrarily small. With a parameterized model, in which we progressively change the geometry, we address contradicting statements in the arterial wall mechanics literature, hence an open question. Our results demonstrate that the maximum and average first principal stresses in the arterial wall may increase or decrease depending on the local curvatures of the initial configuration.

5 A COMPUTATIONAL FRAMEWORK FOR PATIENT-SPECIFIC MODELING OF HUMAN ARTERIES CONSIDERING INITIAL STRESSES AND SUPRA-PHYSIOLOGICAL LOADS

Abstract Catheter-based surgeries such as stent-graft placement, intra-aortic balloon occlusion or angioplasty may cause high stresses and damage in the aorta. We present a modeling framework to numerically evaluate stress and damage distributions inside the layers of patient-specific human aortas. Our constitutive model describes the supra-physiological load range, and our framework accounts for both layer-specific residual stresses within the tissue, and prestresses which exist because finite element models reconstructed from medical images generally represent geometries under *in vivo* loads, e.g., blood pressure. In our representative, patient-specific simulations we note significant correlation between local wall curvature and stress magnitude, resulting in large variations in the stresses predicted along the circumference of the aorta. While such effects are present in virtually all current patient-specific simulations, large stress variations are unlikely to occur *in vivo*. Thus, we propose to 'precondition' the aorta with a maximum loading corresponding to rigorous exercise, a pragmatic approach to account for material inhomogeneity, but one that leads none-the-less to physiologically relevant results. Our modeling framework, together with the material and structural parameters all based on experimental data, can be used to analyze endovascular procedures and, in the future, may help improve patient outcomes.

5.1 Introduction

Catheter-based procedures reduce pain and hospitalization time for patients with cardiovascular disease, a major cause of morbidity and death in the western world. However, deployment of stents-grafts or inflation of intra-aortic balloons can cause large deformations in the aorta, thus generating high stresses which may cause damage in the tissue. Typically, an endograft for endovascular repair of aortic aneurysms is oversized by $10-20\%$ to maintain adequate sealing between the vessel and the graft [5]. Intra-aortic balloon inflation is another procedure which may cause damage in the aorta. None-the-less, balloon occlusion is performed at a variety of positions along the aorta as part of many treatments, e.g., with hemorrhagic shock resulting from pelvic fracture [123], with aneurysm repair [124], with ruptured abdominal aortic aneurysms (AAAs) [125, 126], or to stop gastrointestinal bleeding [127].

In order to study such problems using a patient-specific, finite element (FE) framework, one requires both appropriate constitutive models, fitted to experimental data on human tis-

sue samples, and methods to account for initial stresses, namely both prestresses and residual stresses, in the simulations. In this study we use a FE implementation of the damage model published by Weisbecker et al. [93] to simulate and study the supra-physiological stress-strain response of human aortic tissue. In aged arteries the intima thickens and all three layers (intima, media, adventitia) bear significant load, and hence are mechanically relevant [77, 93]. To improve the fidelity of current modeling approaches we demonstrate our modeling framework on a representative three-layer, patient-specific model of the human thoracic aorta derived from cardiac-gated Magnetic Resonance Images (MRI).

Medical imaging is most often performed *in vivo*, and hence the reconstructed model geometry in the problem of interest will represent the *in vivo* state, e.g., a blood vessel deformed under physiological blood pressure. However, classical continuum mechanics and FE methods assume that constitutive models and the corresponding simulations begin from unloaded, stress-free reference conditions. When applying such classical approaches to patient-specific simulations of arteries a theoretical inconsistency arises: the *in vivo* determined 'initial' geometry is not an unloaded reference configuration. To address this problem Gee et al. [29, 30] proposed a method to include prestresses (stresses in equilibrium with the known boundary conditions of the initial model geometry) to patient-specific geometries of AAAs based on an updated Lagrangian approach.

We recently proposed a Generalized Prestressing Algorithm (GPA), [128], based on the concept introduced by Gee et al. [30]. Briefly, an incremental deformation gradient is calculated from the incremental displacement field. The incremental displacement field is then deleted and the deformation gradient field is updated with the incremental deformation gradient field. Our algorithm requires fewer history terms relative to Gee et al. [30], thus decreasing the memory requirements and computational cost, an advantage for large patient-specific simulations. Compared to the inverse design analysis [31, 32], which computes the actual load-free configuration prior to classical forward simulations, our GPA is easier to implement and is not prone to geometric buckling.

Residual stresses exist in healthy human arteries, and residual stresses have a significant effect on the *in vivo* distribution of stresses, and hence on the development of arterial tissues, see, e.g., Chuong and Fung [129] and Bustamante and Holzapfel [130]. Early studies investigated residual stresses in arteries by measuring the 'opening angles' of radially cut arterial rings, e.g., Fung [22] and Fonck et al. [23]. Residual stresses/stretches have previously been incorporated into FE models by simulating the closing of arterial segments, modeled with a single opening angle, to create thick-walled tubular segments prior to additional loading, see e.g., Balzani et al. [78] and Holzapfel and Gasser [34].

Holzapfel et al. [24] investigated 3D residual deformations for layer-separated tissue strips (intima, media and adventitia) in their passive states, and showed that residual deformations are three dimensional and cannot be described by a single parameter such as the 'opening angle'. We base our approach to including residual stretches in FE simulations

on the experimental data of Holzapfel et al. [24], where residual deformations of the aortic tissue layers are reported after separating these layers from one another. From these deformations we compute a residual deformation gradient and map it element-wise into our FE models. The prescribed residual deformation is not necessarily in equilibrium and may induce deformation in the geometry. We propose an iterative process to include residual stresses and to still ensure that the residually stressed geometry equals the geometry determined from medical imaging.

Alastrué et al. [35, 131] included residual stresses into patient-specific simulations of arteries using methods based on the 'opening angle'. One drawback to their approach relative to our study is that the residually stressed configuration does not match the geometry determined from the medical images. Subsequently we refer to both the prestress and the residual stress distributions as the initial stresses present in the configuration determined from the medical images.

Several researches have proposed constitutive models for soft biological tissues which include the damage behavior of particular tissue components, see, e.g., [43, 63, 132, 133]. Recently researchers have also proposed damage models specifically for arterial tissues. Li and Robertson [65] suggest a layer-specific damage model focusing on sub-failure mechanical damage of the elastin, ground matrix and collagen, represented by the recruitment of collagen fibers, gradual degeneration, failure of arterial components and changes in the tissue properties. Li et al. [134] then demonstrate the constitutive model by simulating cerebral angioplasty, however, they use axisymmetric FE geometries (not patient-specific) for the cerebral artery and do not use layer-specific experimental data for the elastic and damage properties of the artery. Marini et al. [61] propose an isotropic continuum damage model for AAA wall considering tissue heterogeneity. They demonstrate their simulation approach using a series of patient-specific models of AAA for rupture prediction and discuss potential applications in growth and remodeling. Balzani et al. [60] propose a continuum damage model using internal scalar variables to represent collagen fiber damage defined such that no damage occurs in the physiological loading domain. To demonstrate the framework, they evaluate softening in a patient-specific, arterial cross-section (2D model) at supra-physiological intraluminal pressure. None of the models discussed here employ three-layer, 3D patient-specific arterial geometries, account for initial stresses, nor examine the stress distribution through the thickness of the vessel wall.

Alastrué et al. [131] propose a similar numerical framework for patient-specific modeling of vascular tissue where a residually stressed and geometrically consistent model of the patient is obtained. However, they assume a constant wall thickness for the artery, using a single set of material parameters obtained from porcine tissue, determining the residual stresses based on an opening angle approach, and neglecting tissue softening due to supra-physiological loads. Contrary to that, the wall thickness we use is estimated from MRI, the material parameters as well as the residual stretches for all three layers are determined experimentally from human tissue and we include the softening behavior to the material.

This adds to the improved method to apply the residual stresses to geometry obtained form medical imaging.

We combine these elements with the aforementioned features to establish a framework for modeling surgical procedures such as stent-graft placement or intra-aortic balloon occlusion. Furthermore, we define a new measure, an increment of tissue damage, to describe softening associated with supra-physiological loads, as opposed to softening associated with the preconditioning behavior of arterial tissue [80].

In Section 2 we summarize the constitutive model and detail its algorithmic implementation in the context of the FE method. Furthermore, we detail our numerical methods to include initial stresses, both the residual stress/stretch and the prestress/stretch. In Section 3 we show that the three-layer model can reproduce experimental data from the intact wall. We also discuss a 3D patient-specific model of a human thoracic aorta loaded with internal pressure and study aspects of the modeling framework, including the the influence of initial stresses on the predicted stress distributions and the correlation between local tissue stresses and the local curvature along the circumference of the aorta. As a final demonstration, we simulate intra-aortic balloon occlusion in a human thoracic aorta. In Section 4 we discuss our results, while we conclude in Section 5.

5.2 Constitutive and numerical modeling

5.2.1 Constitutive relations

We consider a multiplicative decomposition of the deformation gradient $\mathbf{F} = (J^{1/3}\mathbf{I})\overline{\mathbf{F}}$ with the Jacobian determinant $J = \det\mathbf{F} > 0$. The term $J^{1/3}\mathbf{I}$ is associated with volume-changing deformations ($\mathbf{I}$ is the second-order unit tensor), while $\overline{\mathbf{F}}$, with $\det\overline{\mathbf{F}} = 1$, is associated with volume-preserving deformations of the material [81].

We base our approach on the pseudo-elastic damage model introduced by Ogden and Roxburgh [48], which has the form

$$\Psi(J, \overline{\mathbf{C}}, \eta) = \Psi_{\text{vol}}(J) + \eta\overline{\Psi}^{0}(\overline{\mathbf{C}}) + \Phi(\eta), \tag{5.1}$$

where Ψ_{vol} and $\overline{\Psi}^{0}$ describe the volumetric and isochoric elastic responses, respectively, $\overline{\mathbf{C}} = \overline{\mathbf{F}}^{\mathrm{T}}\overline{\mathbf{F}}$ denotes the modified right Cauchy-Green tensor, while Φ denotes the damage function which implicitly defines the damage variable η. Here we choose the evolution equation

$$\eta = 1 - \frac{1}{r}\text{erf}\left[\frac{1}{m}(\overline{\Psi}^{\max} - \overline{\Psi}^{0})\right], \tag{5.2}$$

where $r > 1$ determines the maximum material damage that can be induced under mechanical loading, $m > 0$ characterizes the dependence of the damage on the deformation and $\overline{\Psi}^{\max}$ is the maximum isochoric strain energy recorded over the load history.

With this definition of the damage variable, $\eta = 1$ relates to a path on the primary loading curve. Therefore, the minimum of the damage variable

$$\eta^{\min} = 1 - \frac{1}{r}\mathrm{erf}\left(\frac{1}{m}\overline{\Psi}^{\max}\right) \tag{5.3}$$

characterizes damage induced to the material. For more details on pseudo-elastic damage theory and the derivation of this damage variable from the damage function we refer to Ogden and Roxburgh [48].

In Weisbecker et al. [93] we propose a pseudo-elastic damage model for arterial tissues, and in [135] we conclude that damage is primarily related to the collagen fibers by testing specimens where either elastin or collagen are digested. Hence, the strain-energy function we use is

$$\Psi(J, \overline{\mathbf{C}}, \eta_4, \eta_6) = \Psi_{\mathrm{vol}}(J) + \overline{\Psi}^0_{\mathrm{m}}(\overline{\mathbf{C}}) + \sum_{i=4,6}[\eta_i \overline{\Psi}^0_{\mathrm{f},i}(\overline{\mathbf{C}}) + \Phi_{\mathrm{f},i}(\eta_i)], \tag{5.4}$$

$$\eta_i = 1 - \frac{1}{r_i}\mathrm{erf}\left[\frac{1}{m_i}(\overline{\Psi}^{\max}_{\mathrm{f},i} - \overline{\Psi}^0_{\mathrm{f},i})\right], \qquad i = 4,6, \tag{5.5}$$

where the subscript m refers to the non-collagenous matrix components of the tissue, and the subscript f to the collagen fiber network. Note, that the damage variable η_i only alters the strain energy of the fibers, i.e. $\overline{\Psi}^0_{\mathrm{f},i}$. The volumetric part of the strain-energy function has the form $\Psi_{\mathrm{vol}} = K\log(J)^2/2$, where the penalty parameter K enforces quasi-incompressibility. We choose a neo-Hookean behavior for the matrix component such that $\overline{\Psi}^0_{\mathrm{m}} = \mu(\overline{I_1} - 3)/2$, where $\mu > 0$ is the initial shear modulus and $\overline{I_1} = \mathrm{tr}\overline{\mathbf{C}}$. The two families of collagen fibers [7] form a network which exhibits an exponential response according to Gasser et al. [39] such that

$$\overline{\Psi}^0_{\mathrm{f},i} = \frac{k_1}{2k_2}\{\exp[k_2(\overline{I}^*_i - 1)^2] - 1\}, \qquad i = 4,6, \tag{5.6}$$

where $k_1 > 0$ is a stress-like parameter and $k_2 > 0$ is a dimensionless parameter. We define the mixed invariants $\overline{I}^*_i = \kappa\overline{I_1} + (1 - 3\kappa)\overline{I_i}$ by using $\overline{I_4} = \mathbf{M}\cdot\overline{\mathbf{C}}\mathbf{M}$ and $\overline{I_6} = \mathbf{M}'\cdot\overline{\mathbf{C}}\mathbf{M}'$, where the unit vectors $\mathbf{M}$ and $\mathbf{M}'$ characterize the mean fiber orientations. These are defined by a single parameter, namely the fiber angle $\pm\varphi$ measured from the circumferential direction of the aorta (fiber components along the radial direction of the artery wall are here neglected). The parameter $\kappa \in [0, 1/3]$ describes the dispersion of the fiber orientation. The anisotropic parts $\overline{\Psi}^0_{\mathrm{f},i}$, $i = 4,6$ of the strain-energy function only contribute to the total strain energy Ψ if $\overline{I}^*_i > 0$. This implies that damage, which is associated with the collagen fibers, is only accumulated if $\overline{I}^*_i > 0$. For more details on the constitutive model, and it's fit to experimental data, we refer to Weisbecker et al. [93].

We compute the second Piola-Kirchhoff stress tensor from (5.4) via $\mathbf{S} = 2\partial\Psi/\partial\mathbf{C} = \mathbf{S}_{\mathrm{vol}} + \overline{\mathbf{S}}_{\mathrm{m}} + \overline{\mathbf{S}}_{\mathrm{f},i}$, i = 4,6. Hence, with $\mathbf{S}_{\mathrm{vol}} = 2\partial\Psi_{\mathrm{vol}}/\partial\mathbf{C}$, $\overline{\mathbf{S}}_{\mathrm{m}} = 2\partial\overline{\Psi}_{\mathrm{m}}/\partial\mathbf{C}$ and using $\overline{\Psi}^0_{\mathrm{f},i} = \Phi'_{\mathrm{f},i}$

we have

$$\overline{\mathbf{S}}_{\mathrm{f},i} = 2\left[\eta_i \frac{\partial \overline{\Psi}^0_{\mathrm{f},i}}{\partial \mathbf{C}} + \overline{\Psi}^0_{\mathrm{f},i}\frac{\partial \eta_i}{\partial \mathbf{C}} + \Phi'_{\mathrm{f},i}\frac{\partial \eta_i}{\partial \mathbf{C}}\right] = \eta_i \overline{\mathbf{S}}^0_{\mathrm{f},i}, \qquad \overline{\mathbf{S}}^0_{\mathrm{f},i} = 2\frac{\partial \overline{\Psi}^0_{\mathrm{f},i}}{\partial \mathbf{C}}. \tag{5.7}$$

From here we then obtain the Kirchhoff stress tensor τ and the Cauchy stress tensor σ by the push forward operation $\tau = \mathbf{F}\mathbf{S}\mathbf{F}^{\mathrm{T}}$, with $\sigma = J^{-1}\tau$.

In order to obtain efficient nonlinear solutions in the context of the FE method, we need the consistently linearized elasticity tensor for use in iterative techniques of Newton's type. The elasticity tensor in the Lagrangian description is $\mathbb{C} = 4\partial^2\Psi/\partial\mathbf{C}\partial\mathbf{C} = \mathbb{C}_{\mathrm{vol}} + \overline{\mathbb{C}}_{\mathrm{m}} + \overline{\mathbb{C}}_{\mathrm{f},i}$, and thus $\mathbb{C}_{\mathrm{vol}} = 4\partial^2\Psi_{\mathrm{vol}}/\partial\mathbf{C}\partial\mathbf{C}$, $\overline{\mathbb{C}}_{\mathrm{m}} = 4\partial^2\overline{\Psi}_{\mathrm{m}}/\partial\mathbf{C}\partial\mathbf{C}$ and

$$\overline{\mathbb{C}}_{\mathrm{f},i} = 4\eta_i \frac{\partial^2 \overline{\Psi}^0_{\mathrm{f},i}}{\partial\mathbf{C}\partial\mathbf{C}} + 4\frac{\partial \overline{\Psi}^0_{\mathrm{f},i}}{\partial\mathbf{C}} \otimes \frac{\partial \eta_i}{\partial\mathbf{C}}, \qquad i = 4,6, \tag{5.8}$$

where

$$\frac{\partial \eta_i}{\partial \mathbf{C}} = \frac{\partial \eta_i}{\partial \overline{\Psi}^0_{\mathrm{f},i}}\frac{\partial \overline{\Psi}^0_{\mathrm{f},i}}{\partial \mathbf{C}} \tag{5.9}$$

such that we can write with $(5.7)_2$

$$\overline{\mathbb{C}}_{\mathrm{f},i} = 4\eta_i \frac{\partial^2 \overline{\Psi}^0_{\mathrm{f},i}}{\partial\mathbf{C}\partial\mathbf{C}} + \frac{\partial \eta_i}{\partial \overline{\Psi}^0_{\mathrm{f},i}}\overline{\mathbf{S}}^0_{\mathrm{f},i} \otimes \overline{\mathbf{S}}^0_{\mathrm{f},i}, \qquad i = 4,6. \tag{5.10}$$

Furthermore,

$$\frac{\partial \eta_i}{\partial \overline{\Psi}^0_{\mathrm{f},i}} = \frac{2}{m_i r_i \sqrt{\pi}} \exp\{-[m_i^{-1}(\overline{\Psi}^{\max}_{\mathrm{f},i} - \overline{\Psi}^0_{\mathrm{f},i})]^2\}, \tag{5.11}$$

where the property $\mathrm{d}[\mathrm{erf}(z)]/\mathrm{d}z = 2\exp(-z^2)/\sqrt{\pi}$ has been used. On the primary loading curve $\eta_i = 1$ and $\partial\eta_i/\partial\mathbf{C} = \mathbf{O}$, hence $\overline{\mathbb{C}}_{\mathrm{f},i} = 4\partial^2\overline{\Psi}^0_{\mathrm{f},i}/\partial\mathbf{C}\partial\mathbf{C}$. A derivation for the isotropic part of the elasticity tensor can be found in, e.g., Miehe [136], while the anisotropic elastic part (i.e. without damage) can be found in Gasser et al. [39]. The full anisotropic part of the Lagrangian elasticity tensor $\overline{\mathbb{C}}_{\mathrm{f},i}$ and the Eulerian elasticity tensor $\overline{\mathbb{c}}_{\mathrm{f},i}$ we derive in A.1.

It is well established that softening of arterial tissues occurs during mechanical testing at physiological loadings, a phenomenon usually referred to as preconditioning behavior of the tissue [80]. In order to distinguish softening in the physiological loading range from softening due to tissue damage, and thus allow a more accurate interpretation of the simulation results, we define the increase in softening from the physiological load, say, e.g., systolic blood pressure, to supra-physiological loads as $\Delta\eta$. We calculate the new measure, the increment of tissue damage $\Delta\eta$, by comparing the minimum of the damage variable at arbitrary supra-physiological loads $\eta^{\min}$ and the minimum of the damage variable at

Initialize $\overline{\Psi}^{\max}_{\mathrm{f},i} = 0$ $(i = 4,6)$, for each Newton iteration and each fiber family i:

1. Compute $\overline{\tau}^{0}_{\mathrm{f},i}$ from the push forward of $(5.7)_2$ and determine $\overline{\mathbb{c}}^{0}_{\mathrm{f},i}$, see the A.1
2. Compute $\overline{\Psi}^{0}_{\mathrm{f},i}$ from (5.6)
3. Read $\overline{\Psi}^{\max}_{\mathrm{f},i}$ from history
4. Check:
   if $\overline{\Psi}^{0}_{\mathrm{f},i} > \overline{\Psi}^{\max}_{\mathrm{f},i}$
   $\overline{\Psi}^{\max}_{\mathrm{f},i} \leftarrow \overline{\Psi}^{0}_{\mathrm{f},i}$ (write to history)
   end if.
5. Compute η_i, $\dfrac{\partial \eta_i}{\partial \overline{\Psi}^{0}_{\mathrm{f},i}}$ and $\overline{\tau}^{0}_{\mathrm{f},i}$ from (5.5), (5.11) and the push forward of $(5.7)_2$
6. Compute $\overline{\tau}_{\mathrm{f},i} = \eta_i \overline{\tau}^{0}_{\mathrm{f},i}$ and $\overline{\mathbb{c}}_{\mathrm{f},i} = \eta_i \overline{\mathbb{c}}^{0}_{\mathrm{f},i} + \dfrac{\partial \eta_i}{\partial \overline{\Psi}^{0}_{\mathrm{f},i}} \overline{\tau}^{0}_{\mathrm{f},i} \otimes \overline{\tau}^{0}_{\mathrm{f},i}$

Table 5.1: Computation of fiber contributions (fiber families $i = 4,6$) to the total Kirchhoff stress and the Eulerian elasticity tensors for the damage model presented in Section 5.2.1.

physiological blood pressure $\eta^{\min}_{\mathrm{phy}}$. In order to have consistency with the definition of the damage variable η (i.e. $\Delta\eta_i = 1$ refers to an undamaged collagen fiber network i, and $\Delta\eta_i \to 0$ refers to severely damaged fibers), we propose

$$\Delta\eta_i = 1 - (\eta^{\min}_{\mathrm{phy},i} - \eta^{\min}_{i}), \qquad i = 4,6. \tag{5.12}$$

Using the generalized error function

$$\mathrm{erf}(a,b) = \frac{2}{\sqrt{\pi}} \int_a^b e^{-s^2} \mathrm{d}s = \mathrm{erf}(b) - \mathrm{erf}(a), \tag{5.13}$$

we can reinterpret $\Delta\eta_i$ as

$$\Delta\eta_i = 1 - \frac{1}{r}\mathrm{erf}\left(\frac{\overline{\Psi}^{\max}_{\mathrm{phy},i}}{m}, \frac{\overline{\Psi}^{\max}_{\mathrm{f},i}}{m}\right), \qquad i = 4,6, \tag{5.14}$$

which has the same form as (5.3), and where $\overline{\Psi}^{\max}_{\mathrm{phy},i}$ is the isochoric strain energy recorded in the fiber family i under physiological loads and $\overline{\Psi}^{\max}_{\mathrm{f},i}$ is the maximum isochoric strain energy recorded in the fiber family i over the (supra-physiological) load history. In what follows we refer to $\Delta\eta_i$ as the damage increase in the collagen fiber family i.

5.2.2 Numerical implementation

We realize the algorithmic FE implementation of the damage model for each fiber family in the collagen network. For the corresponding hyperelastic model of Gasser et al. [39] the

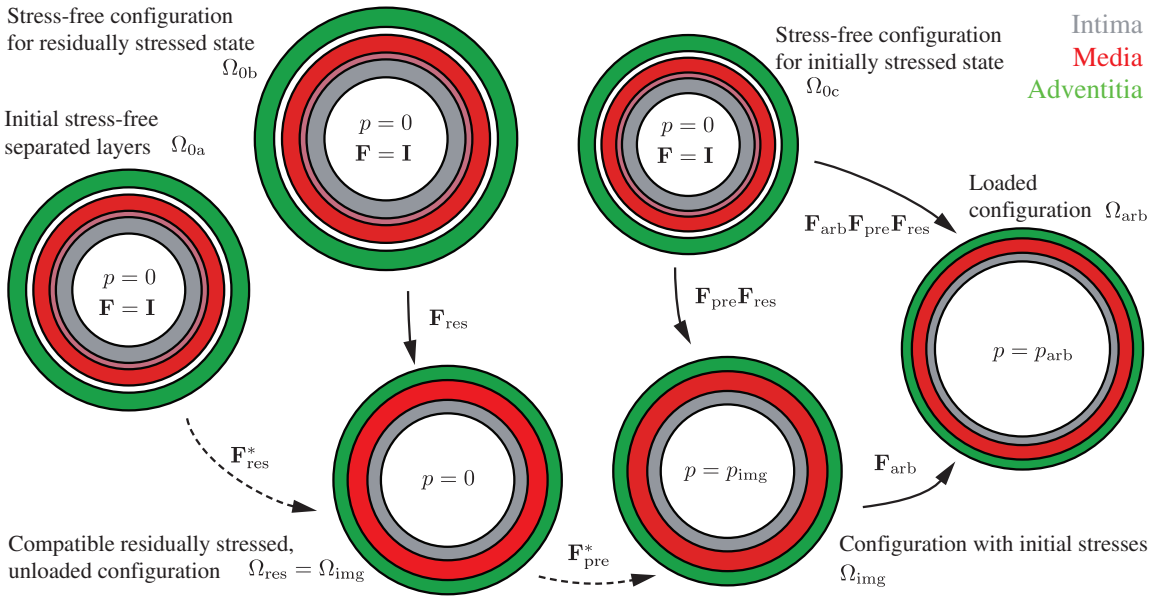

Figure 5.1: Deformation history of the aortic arterial layers up to loading with an arbitrary internal pressure p_{arb} including the effects of initial stresses. The reference configuration Ω_{0a} relates to the imaginary residually stressed configuration without an iteration procedure. The reference configuration Ω_{0b} relates to the geometry of Ω_{img} with an iteration procedure but without a prestressing algorithm. The reference configuration Ω_{0c} relates to the arbitrary loaded configuration. The asterisk and the dashed arrows denote deformations in which the current configuration does not change its geometry.

iterative process to compute the entries for the stress and stiffness matrices is shown in Table 5.1.

Figure 5.1 schematically illustrates the steps used to include initial stresses and describes the deformation history. The configuration we assume to be stress-free and on which we apply the residual stresses is Ω_{0a}. Here the residual stresses are released by separating the layers, therefore the layers form a non-compatible geometry. No internal pressure acts on the inner aortic wall. After applying the residual stresses with an iterative procedure and obtaining a compatible geometry, the configuration Ω_{res} is achieved [128]. This configuration comprises residual stresses but the internal pressure p remains zero. By using the iterative procedure, we obtain a residually stressed state on $\Omega_{res} = \Omega_{img}$, which corresponds to the geometry from medical imaging. Since the strain-energy function uniquely relates stresses and strains, and the stress state changed without any changes of the geometry, the configuration Ω_{res} obtained with the iteration procedure relates to a new reference configuration Ω_{0b}.

In the next step, we increase the internal pressure without updating the geometry and obtain the configuration Ω_{img}. The stress state has now changed compared to Ω_{res} but the geometry has not. Again, as the strain-energy function uniquely relates stresses and strains the unloaded reference configuration of Ω_{img} has changed compared to Ω_{res}, say Ω_{0c}. After applying the initial stresses, the geometry can be loaded with arbitrary loads and we obtain Ω_{arb}. The individual steps described here are detailed in what follows. In Fig. 5.1 solid curves depict deformations that relate two configurations. If the reference configurations change due to the used algorithms (iteration procedure or prestressing), it is marked with dashed curves and the corresponding deformation gradients are marked with an asterisk.

Residual stresses

In order to account for residual stresses in our modeling framework, we draw on the experimentally measured residual deformations from Holzapfel et al. [24]. Therein, when the three layers of the composite aortic wall (Intima, Media, Adventitia) are separated, the authors measure the resulting residual deformations experimentally, e.g., the intima enlarges and the media and adventitia shrink after separation. We use these data to define a deformation gradient $\mathbf{F}_{\text{res}}(\mathbf{x})$ describing the residual deformation in the intact aortic wall. To map the deformation gradient into a (possibly patient-specific) FE model, we compute a local coordinate system for each element, where the local circumferential direction θ, the local axial direction z and the local radial direction r of the aortic geometry are determined based on the element's position within the aorta.

To this end, we define the element coordinate system at the center of each element using the local circumferential $\mathbf{N}_\theta$, axial $\mathbf{N}_z$ and radial $\mathbf{N}_r$ basis vectors of the aortic section, implemented using a custom MATLAB (2009b, The MathWorks, Inc., Massachusetts, USA) code. First we define the local axial direction $\mathbf{N}_z$ parallel to the direction of the lumen center line, at the MRI stack height of the element center. We next define the local circumferential direction $\mathbf{N}_\theta$ as normal to the plane spanned by $\mathbf{N}_z$ and a vector from the lumen center line (at the MRI stack height of the element center) to the center of the element. Finally, the local radial direction $\mathbf{N}_r$ is the direction perpendicular to both $\mathbf{N}_\theta$ and $\mathbf{N}_z$. Our method is similar to that introduced in Kiousis [121].

We define the local deformation gradient in the initial element coordinate system as (in matrix notation)

$$[\mathbf{F}^{\text{loc}}_{\text{res},l}] = \begin{bmatrix} \lambda_{\theta,l} & 0 & 0 \\ 0 & \lambda_{z,l} & 0 \\ 0 & 0 & \lambda_{r,l} \end{bmatrix}, \tag{5.15}$$

with $l \in$ [Intima, Media, Adventitia] and stretches $\lambda_{\theta,l}$ and $\lambda_{z,l}$ determined experimentally [24]; we compute $\lambda_{r,l}$ assuming isochoric deformations, i.e. $\det[\mathbf{F}^{\text{loc}}_{\text{res},l}] = 1$. For the FE model, we need the deformation gradient in the global coordinate system and thus transform it using the tensor transformation

$$\mathbf{F}_{\text{res}} = \mathbf{Q}^{\text{T}} \mathbf{F}^{\text{loc}}_{\text{res},l} \mathbf{Q} \tag{5.16}$$

where $\mathbf{Q}$ is an orthogonal (transformation) tensor. Prior to the first load step, the FE program reads in the deformation gradient and prescribes the corresponding values to the Gauss points. As a result, the stress-free configuration Ω_0 is not part of the numerical simulation.

After we prescribe the deformation gradient $\mathbf{F}_{\text{res}}$ to $\Omega_{0\text{a}}$ at each Gauss point of a simulation, global equilibrium is no longer fulfilled. To generate a robust solution we initially apply fixed displacement boundary conditions to the model which we gradually relax such that the residually stressed geometry represents a load-free configuration. However, once the residual stresses are in equilibrium, the deformed model geometry differs from the imaged geometry Ω_{res}. In order to correct this situation, we propose an iterative scheme to map the residual stresses back onto Ω_{res}. We map the deformation gradient field from the first relaxation $\mathbf{F}_{\text{res},1}$ onto the geometry Ω_{res} and again relax the boundary conditions. We then map the resultant deformation gradient field $\mathbf{F}_{\text{res},2}$ onto the imaged geometry and again relax the boundary conditions. We repeat this process until the change between the resulting deformation gradient fields $\mathbf{F}_{\text{res,n}}$ and $\mathbf{F}_{\text{res,n+1}}$ falls below a prescribed tolerance. In our example five iterations are sufficient to reduce the mean square error between the deformation gradient fields calculated from two subsequent relaxations to approximately 10^{-5} to 10^{-8}. After this iterative relaxation procedure we obtain the compatible residually stressed, unloaded configuration on Ω_{res}.

Prestresses

In order to account for prestresses in our modeling framework, we use the GPA [128], a generalized and modified version of an algorithm introduced by Gee et al. [29, 30]. Briefly, we calculate an incremental deformation gradient from the incremental displacement determined from each converged iteration step. We then delete the incremental displacement and update the total deformation gradient with the incremental deformation gradient. To do this, we define the total deformation gradient as an additional history variable during the computation.

After accounting for both residual stresses and prestress, an arbitrary deformation $\mathbf{F}_{\text{arb}}$, now computed with a conventional FE scheme, yields the corresponding configuration Ω_{arb}. In summary, we compute the total deformation gradient at each Gauss point in the FE model as

$$\mathbf{F}(\mathbf{x},t) = \mathbf{F}_{\text{arb}}(\mathbf{x},t)\mathbf{F}_{\text{pre}}(\mathbf{x})\mathbf{F}_{\text{res}}(\mathbf{x}). \tag{5.17}$$

The essential idea is similar to the strategy presented in [131], however, details such as the iteration procedure for the initial stresses are improved and the implementation of the prestressing algorithm differ.

5.2.3 Numerical examples

To demonstrate different aspects of our modeling framework, we simulate both the uniaxial extension of a tissue sample taken from the thoracic aorta and physiological and supra-

	μ [MPa]	k_1 [MPa]	k_2 [-]	φ [°]	κ [-]	r_f [-]	m_f [-]
Intima	0.034	4.34	13.3	46.5	0.20	1.00	0.014
Media	0.028	0.14	11.9	38.4	0.21	1.87	0.009
Adventitia	0.020	0.39	6.79	52.3	0.23	1.15	0.022

Table 5.2: Median constitutive parameters for the intima, media and adventitia of the human thoracic aorta, as reported in [93].

	$\lambda_{\theta,l}$ [-]	$\lambda_{z,l}$ [-]
Intima	0.963	0.959
Media	1.081	1.042
Adventitia	1.059	1.096

Table 5.3: Residual stretches in the circumferential and axial directions, $\lambda_{\theta,l}$ and $\lambda_{z,l}$, respectively, for the intima, media and adventitia, as reported in [24]. Residual stretch in the radial direction $\lambda_{r,l}$ is calculated assuming isochoric deformations, i.e. $\lambda_{\theta,l}\lambda_{z,l}\lambda_{r,l} = 1$.

physiological loading conditions of the human thoracic aorta. For all examples presented in this paper we use 8-node mixed (Q1P0) brick elements within FEAP (University of California at Berkeley, CA, USA). We model aortic tissue as a three-layer composite, where we specifically model the intima, media and adventitia of the tissue. To this end, we use experimentally determined thickness ratios of $0.19/0.45/0.36$ for the intima/media/adventitia, as reported in Weisbecker et al. [93]. To describe the layers of the thoracic aorta we use the median constitutive parameters for intima, media and adventitia reported also in [93] and summarized in Table 5.2. We incorporate residual stretches (resulting in residual stresses) into our simulations based on the experimental results reported in Holzapfel et al. [24], as summarized in Table 5.3.

Uniaxial extension of a tissue sample taken from the thoracic aorta

First, we study the influence of residual stresses on the predicted transmural stress distributions by comparing results generated with the inclusion of experimentally determined residual stretches (Table 5.3), and without these residual stretches, coincident with the framework described in Fig. 5.1, but omitting the prestresses. We simulate one-fourth of a square sample of thoracic arterial tissue (10×10 mm) with symmetry boundary conditions on two perpendicular edges. The total sample thickness (2.59 mm) and the thickness ratios of the individual layers are experimentally determined [93].

Next, we use this three-layer model with residual stretches, to obtain a stress-stretch response of the intact wall. We simulate a uniaxial extension test with displacement controlled quasi-static cyclic loading to $\lambda = 1.3$ and then to $\lambda = 1.4$. We calculate an average Cauchy stress, say $\bar{\sigma} = f_{\text{sum}}/A_f$, by using the sum of the reaction forces f_{sum} and the current cross-sectional area A_f normal to the force. For a comparison with the correspond-

ing experimentally determined constitutive parameters, we then fit the constitutive model to the stretch-stress relationship representing the mechanical behavior of the intact three-layer aortic wall.

Physiological and supra-physiological loadings of the human thoracic aorta

To test our modeling framework on clinically relevant problems, we study physiological and supra-physiological loading conditions of the human thoracic aorta on a representative patient. Our representative patient-specific simulations use the thoracic aorta geometry of a 62 year old male patient, derived from MRI. We simulate a section of his aorta which has an inner diameter of approximately 20 mm and a length of 32 mm. Briefly, we segment the edges of the inner and outer aortic wall from the imaging data, and mesh this geometry using a custom meshing algorithm.

We compute the nodes of the hexahedral mesh using the axial slices of the binary segmented MRI. In each slice, we divide the axial contour of both the lumen and the outer wall edge into 10 sections of 36°, using the center of mass of the lumen in each slice. With these nodes, we compute the spline curves that minimize the fitting error. Then we use the resulting spline curves to divide each section into six cubically interpolated subsections, thus determining the 60 circumferential elements. We perform a similar procedure in the axial direction, interpolating along subsets of nodes with equal circumferential positions to determine 32 elements axially. Using the experimentally determined thickness ratios (0.18/0.46/0.36) from [93] to define three arterial tissue layers (intima/media/adventitia) in the FE mesh, we generate each layer of thoracic tissue with four elements through the thickness in order to resolve radial stress and damage gradients. In total the mesh contains 23 040 eight-node brick elements.

Regarding the boundary conditions, we constrain the displacement in z-direction (along the main axis of the aorta) at nodes on the cutting planes of our model, i.e. at the top and bottom of the segment shown in Fig. 5.2(b). Furthermore, on each of these cutting planes, we constrain four nodes on the luminal side at approximately 90° increments along the circumferential direction. These eight nodes can only move in the radial direction within the cutting planes to prevent rigid body rotation around the axial direction.

Once the mesh is finalized, we input the mean fiber directions at the element level, using an approach similar to that of Kiousis et al. [121], implemented in MATLAB and using the local element basis described in Section 5.2.2.

For our initial simulations, we subject the inner wall of the artery to a pressure of $p = 85\,\text{mmHg}\ (= 11.3\,\text{kPa})$, corresponding to the (physiological) diastolic blood pressure and we demonstrate some aspects of our modeling framework. To assess the influence of initial stresses, both residual stresses and prestresses, on the tissue's transmural stress distributions we complete four simulations: (i) a conventional forward calculation from the MRI determined geometry; (ii) a calculation including only prestretches; (iii) a calculation including only residual stretches; (iv) a calculation including both residual stretches and

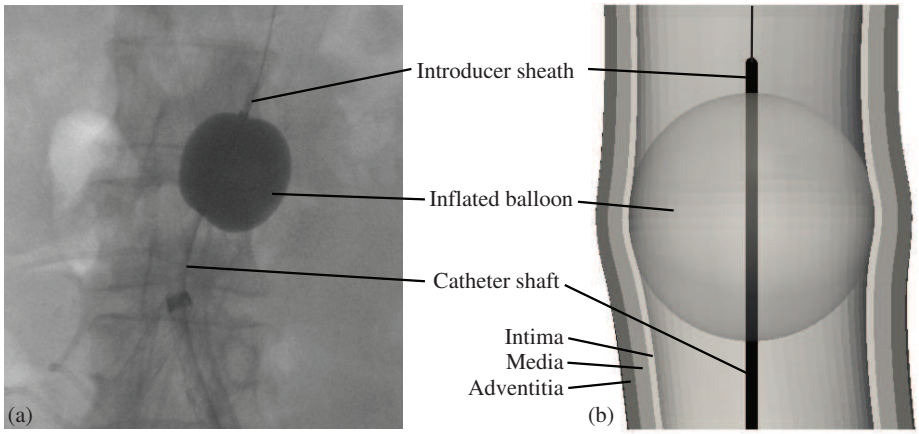

Figure 5.2: Representative intra-aortic balloon occlusion in the thoracic aorta: (a) angiogram of an inflated balloon occlusion in the thoracic aorta [124]; (b) corresponding simulation with the fully inflated balloon inside the patient's aorta. Since the introducer sheath and the catheter shaft do not influence the stress distributions in the aortic segment of our example we do not include them in the simulation.

prestretches. Using these models we also study other aspects of the predicted stress distributions, including those predicted after a load history including a systolic blood pressure of 200 mmHg (= 26.7 kPa) representing rigorous exercise, see, e.g., MacDougall et al. [137]. To this end, we compare the stresses predicted in the thoracic aorta at $p = 85$ mmHg for a maximum loading over the history of both $p_{\max} = 85$ and 200 mmHg.

To study a representative catheter-based procedure on a specific patient, we simulate inflation of an intra-aortic balloon, which may cause high tissue stresses and thus damage in the tissue. Figure 5.2(a) shows an angiogram of an inflated balloon in the thoracic aorta [124]. Figure 5.2(b) shows a cross-section of our corresponding simulation with the fully inflated balloon inside the patient's aorta. To complete this simulation, we approximate the intra-aortic balloon as a rigid sphere since these balloons generally exhibit very high stiffness once they are (nearly) fully inflated, see, e.g., Fig. 7 in [138]. The sphere representing the balloon is fixed at its center on the center line of the aorta. Then the radius of the sphere is increased with each time step until it first comes into contact with the tissue and then it is 'inflated' to its final diameter. The contact algorithm for the simulation is the rigid to node formulation using the penalty method as implemented in FEAP. Since the introducer sheath and the catheter shaft do not influence the stress distributions in the aortic segment of our example we do not include them in the simulation, they are shown only for illustrative purposes. We complete our simulation in two steps. First, we apply an intra-luminal pressure of $p = 85$ mmHg, and second, we 'inflate' the intra-aortic balloon to a diameter of $d = 23.2$ mm. When presenting our results, we plot element stress distributions from the axial center of the aorta on a plane normal to the axial direction. We plot Cauchy stress distributions versus the circumferential direction θ of the aorta.

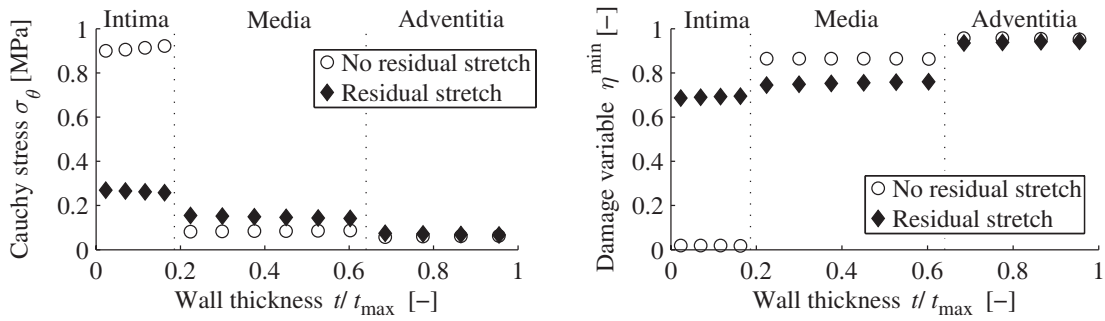

(a) (b)

Figure 5.3: Three-layer tissue sample of a human thoracic aorta under a circumferential stretch of 1.3. Representative transmural distributions predicted by including experimentally determined residual stretches in the simulation, and without including these residual stretches: (a) first principal Cauchy stress σ_θ and (b) fiber damage distribution in form of the damage variable $\eta^{\min}$ versus normalized wall tissue $t/t_{\max}$.

To investigate the influence of the curvature on the predicted stress distributions, we compute the local curvature in the circumferential direction κ_θ as

$$\kappa_\theta = \frac{r^2 + 2\dot{r}^2 - r\ddot{r}}{(r^2 + \dot{r}^2)^{2/3}}, \tag{5.18}$$

where $\dot{r} = \partial r(\theta)/\partial\theta$. We use a least-squares differentiation filter for unequally spaced data to compute the differentiation of the radius $r(\theta)$ with respect to the circumferential coordinate θ [139].

5.3 Results

5.3.1 Uniaxial extension of a tissue sample taken from the thoracic aorta

First, we report the influence of residual stresses on the predicted transmural stress distributions by comparing results generated with and without including experimentally determined residual stretches. Figure 5.3(a) shows a representative transmural distribution of the first principal Cauchy stress σ_θ, while Fig. 5.3(b) shows the resulting fiber damage distribution in form of the damage variable $\eta^{\min}$ for an applied uniaxial (circumferential) stretch of $\lambda = 1.3$.

Next, we compare the stress-stretch behavior of the three-layer finite element model with experimental data obtained from arterial tissue to see whether we can reproduce the behavior of arterial wall. As we use the median of the constitutive parameters for the numerical model, we compare the results to the median values of the intact tissue. We then fit the constitutive model to the obtained stretch-stress relationship to obtain constitutive parameters for the numerical experiment. The results of this simulation correspond to the parameters

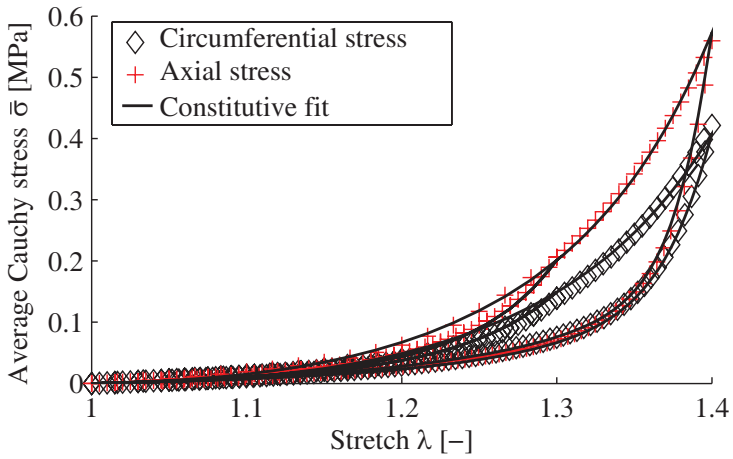

Figure 5.4: Average Cauchy stress $\bar{\sigma}$ versus applied stretch λ (up to 1.4) of numerical uniaxial extension tests in the circumferential (diamonds) and the axial (+) directions, and the corresponding constitutive model fit.

	μ [MPa]	k_1 [MPa]	k_2 [-]	φ [°]	κ [-]	r_f [-]	m_f [-]
Simulation	0.019	0.66	6.72	45.9	0.1	1.27	0.0076
Experiment	0.017	0.56	16.21	51.0	0.18	1.59	0.008
$[Q_1, Q_3]$	$[0.014, 0.019]$	$[0.24, 0.94]$	$[5.79, 34.79]$	$[46.8, 53.8]$	$[0.08, 0.28]$	$[1.25, 1.83]$	$[0.004, 0.011]$

Table 5.4: Comparison of constitutive parameters from the finite element model with experimentally obtained data from [93] for the intact wall of the thoracic aorta.

measured in uniaxial extension tests of the intact wall, see Weisbecker et al. [93]. Figure 5.4 shows the resulting model fit to the simulated uniaxial extension test which accounts for residual stresses, and Table 5.4 compares the experimentally and numerically obtained values for the constitutive parameters. The coefficient-of-determination for our fitting is $r^2 = 0.999$, and except for the angle φ all fitted parameters lie within the interquartile range of the experimental data. Furthermore, if we prescribe φ to be located within the bounds corresponding to the interquartile rage during the fitting process, then all constitutive parameters are within the interquartile range and the coefficient-of-determination remains excellent, with $r^2 = 0.998$.

5.3.2 Physiological and supra-physiological loadings of the human thoracic aorta

Iterative process to determine residual stresses on the imaged geometry

This section demonstrates the influence of the iteration process on the geometry and the stress distribution of the tissue in the unloaded configuration. Figure 5.5 shows the first principal Cauchy stress with (a) and without (b) the iteration procedure. The geometry in Fig. 5.5(a) is the same as the geometry segmented from MRI. In Fig. 5.5(b) the geometry changes, as highlighted by the underlying gray area from imaging. Hence, the iteration

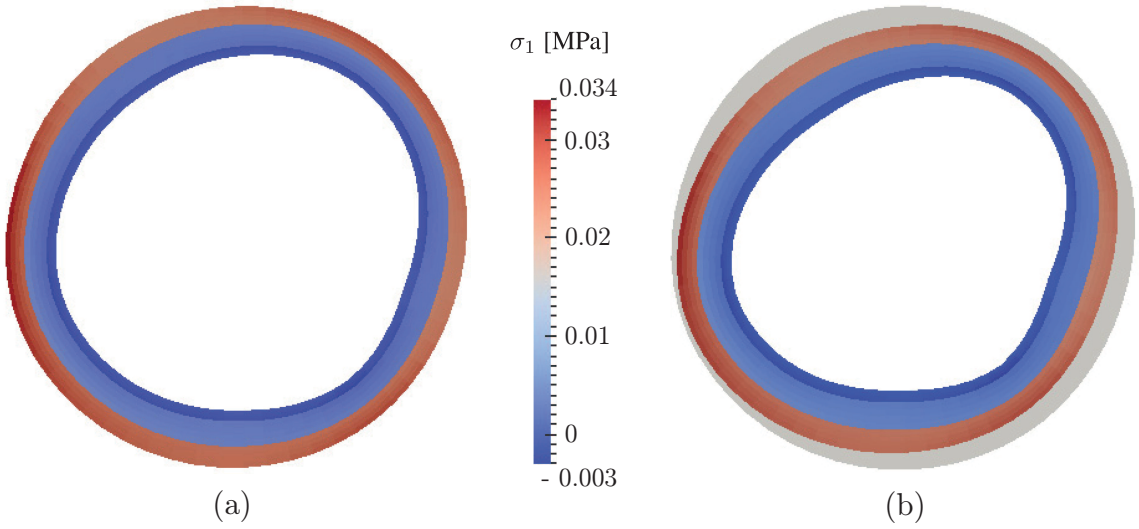

Figure 5.5: Comparison of the first principal Cauchy stress with (a) and without (b) the iteration procedure for the residual stresses. The gray area in (b) corresponds to the geometry obtained from medical imaging. Note that (a) has the reference configuration Ω_{0b} and (b) the reference configuration Ω_{0a}, compare with Fig. 5.1.

process has a notable influence on the geometry, whereas the influence on the stress distribution is negligible.

Influence of initial stresses

To assess the influence of initial stresses on the tissue's transmural stress distribution we analyze four simulations with an arterial pressure of $p = 85\,\text{mmHg}$, as shown in the Figs. 5.6(a)-(d). Figure 5.6(a) illustrates the numerically obtained principal Cauchy stress results of a conventional forward computation from the MRI-determined geometry, while Fig. 5.6(b) illustrates a computation where only prestresses are included, Fig. 5.6(c) shows the computational results including only residual stresses and Fig. 5.6(d) shows the computation including both residual stresses and prestresses. Since we plot the cross-sections, it is clear that the diameter predicted at $p = 85\,\text{mmHg}$ changes notably with the inclusion of initial stresses.

Figure 5.7(a) shows the circumferential Cauchy stresses at the luminal side of the intima plotted along the circumference of the aorta (referring to the case described in Fig. 5.6(d)). The stress variations along the circumferential direction are very high. Figure 5.7(b) shows the correlation between the circumferential Cauchy stress with the local circumferential curvature. The correlation coefficient r^2 equals 0.89 and the positive correlation between the Cauchy stress magnitude and the aortic curvature is statistically significant with $p < 0.05$.

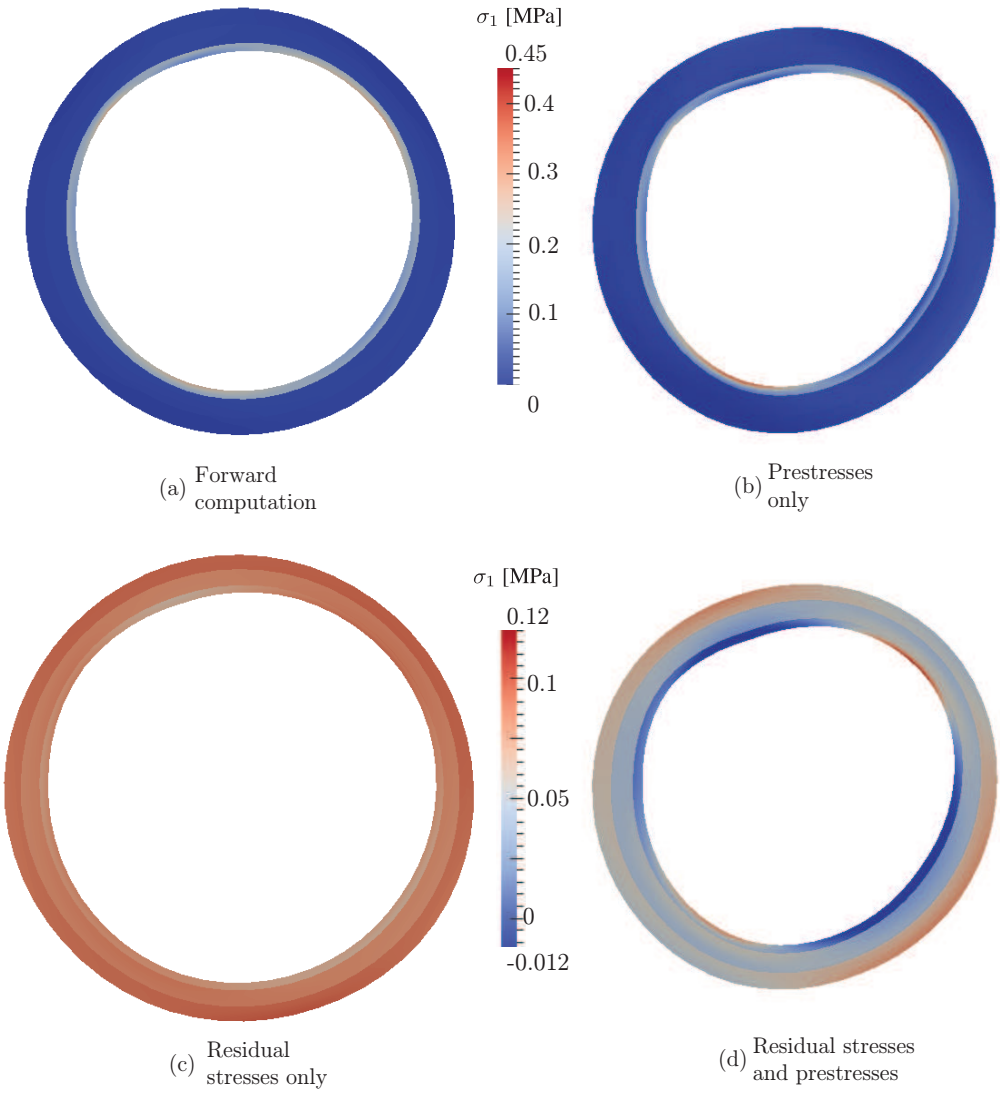

Figure 5.6: First principal Cauchy stress σ_1 in the thoracic aorta at diastolic blood pressure $p = 85\,\text{mmHg}$ at the center of the aortic section: (a) conventional forward computation; (b) results including only prestresses; (c) computation including only residual stresses and (d) computation including both residual stresses and prestresses.

Numerical preconditioning

To illustrate that stress softening occurs after tissue exposure to high blood pressure and that it effects the stress distributions predicted at physiological blood pressure, we compare the stresses predicted at $p = 85\,\text{mmHg}$ for both a maximum load of $p_{\text{max}} = 85$ and of 200 mmHg over the history, the latter representing an example of intraluminal pressure that can be reached during rigorous exercise. Figure 5.8(a) shows the circumferential Cauchy stress σ_θ for $p = 85\,\text{mmHg}$, with the load history of $p_{\text{max}} = 85\,\text{mmHg}$, at the lu-

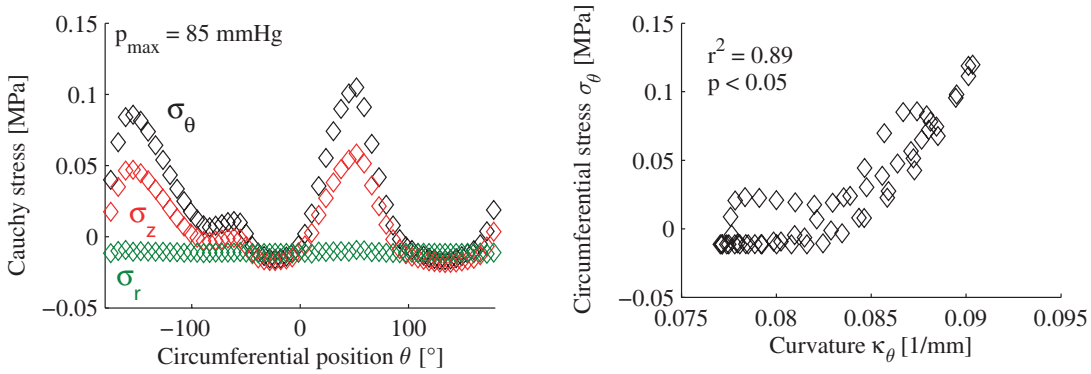

(a) (b)

Figure 5.7: Representative results from a patient-specific simulation of a human thoracic aorta at a blood pressure of $p = 85\,\text{mmHg}$ reached during primary loading: (a) circumferential Cauchy stress σ_θ (black), axial stress σ_z (red) and radial stress σ_r (green) at the luminal side of the intima versus the circumferential position θ; (b) circumferential Cauchy stress σ_θ versus the local circumferential curvature κ_θ, the correlation is statistically significant ($p < 0.05$).

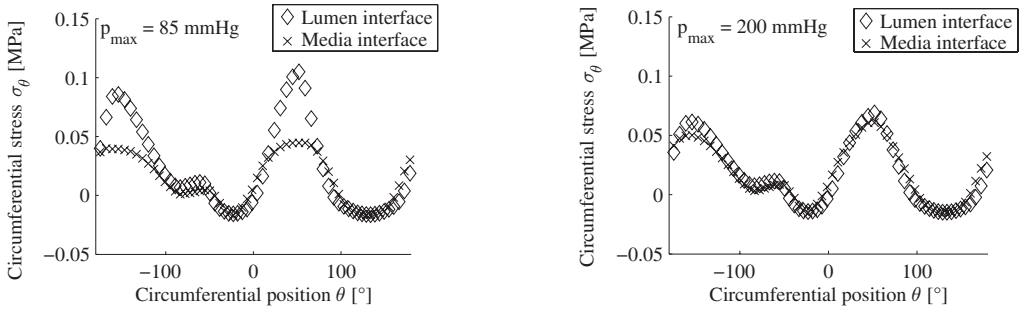

(a) (b)

Figure 5.8: Representative patient-specific simulation of a human thoracic aorta at a blood pressure of $p = 85\,\text{mmHg}$, circumferential Cauchy stress σ_θ in the intima at the lumen interface (diamonds) and at the interface with the media (crosses) versus the circumferential direction θ: (a) predicted with $p_{\max} = 85\,\text{mmHg}$ in the load history; (b) predicted with $p_{\max} = 200\,\text{mmHg}$ in the load history.

minal (diamonds) and medial (crosses) side of the intima. The difference between these curves illustrates the high stress gradient through the thickness of the intima at several circumferential locations of the aorta. Figure 5.8(b) shows the corresponding circumferential Cauchy stress σ_θ for $p = 85\,\text{mmHg}$, with the load history of $p_{\max} = 200\,\text{mmHg}$, at the luminal (diamonds) and medial (crosses) side of the intima, showing a marked decrease in both the stress variation along the circumferential direction θ and the stress gradient through the thickness of the intima.

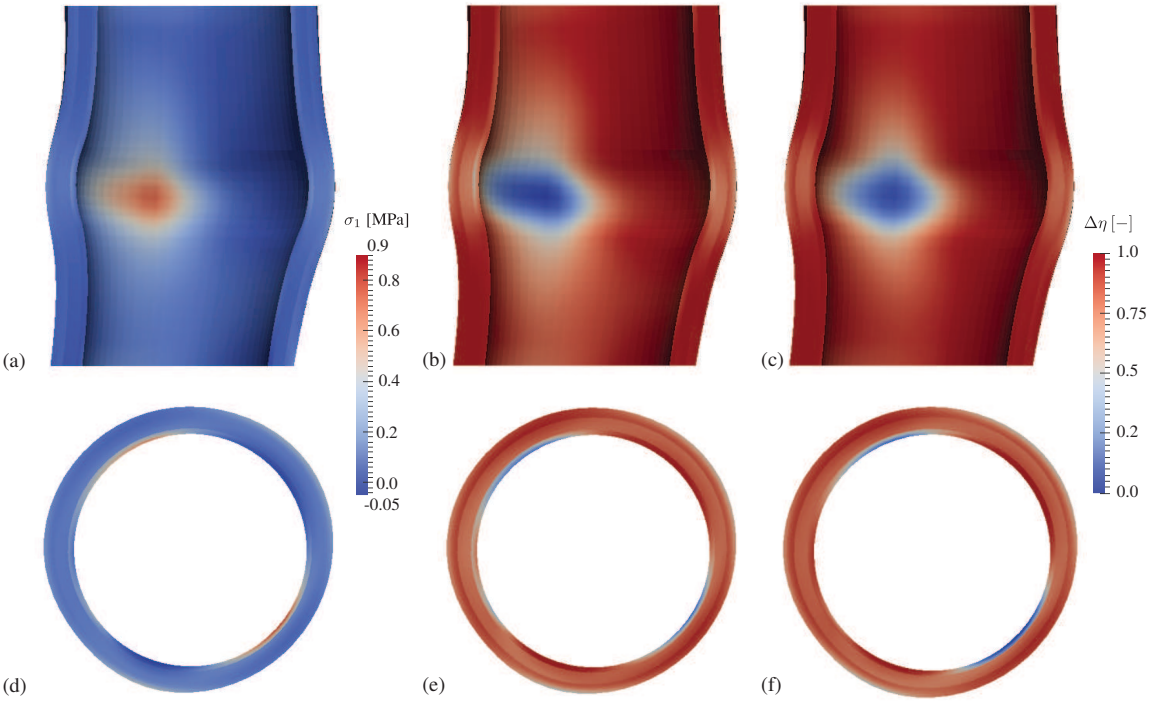

Figure 5.9: Representative patient-specific simulation of a human thoracic aorta undergoing intra-aortic balloon occlusion: (a),(d) distribution of first principal Cauchy stress σ_1 at maximum balloon inflation; (b),(e) $\Delta\eta$ at maximum balloon inflation for the first family of fibers; (d),(f) $\Delta\eta$ at maximum balloon inflation for the second family of fibers.

Intra-aortic balloon occlusion

Figure 5.9 shows stress and damage distributions for a representative simulation of an intra-aortic balloon occlusion, as shown in Fig. 5.2. In particular, Figs 5.9(a),(d) illustrate the distribution of the first principal Cauchy stress σ_1 after intra-aortic balloon occlusion due to a full expansion of the device. As expected, the stresses vary notably around the circumferential direction and reach a maximum value of 0.89 MPa. Figures 5.9(b),(e) and (c),(f) show the damage increase $\Delta\eta$, based on the damage variable $\eta_{\min}$ at $p = 85$ mmHg, for both families of fibers. Figure 5.10 illustrates the evolution of the damage increase $\Delta\eta$ for the most damaged aortic tissue versus the diameter of the inflated balloon ranging from 21 mm to over 23 mm.

5.4 Discussion

To the authors' knowledge this is the first study proposing a modeling framework with such fidelity, particularly for analyzing surgical procedures, where:

(i) 3D patient-specific models include the measured arterial wall thickness estimated from medical images,

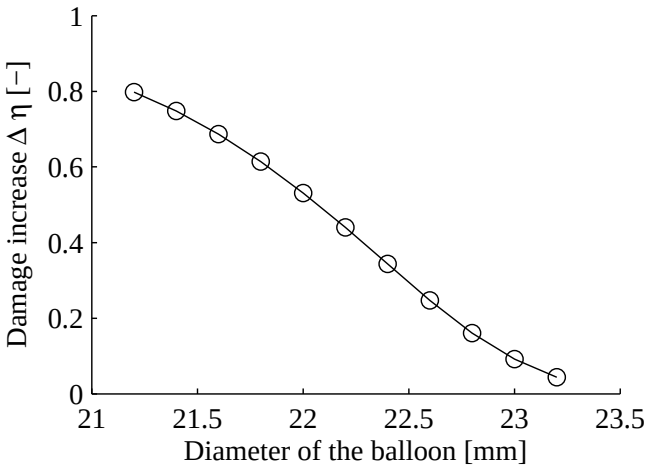

Figure 5.10: Damage increase $\Delta\eta$ versus diameter of the intra-aortic balloon during a representative patient-specific simulation of intra-aortic balloon occlusion.

(ii) three layers of the aorta are explicitly simulated based on experimentally determined thickness ratios of intima/media/adventitia,

(iii) both layer-specific residual stresses and prestresses are mapped on the exact geometry determined from medical imaging to maintain theoretical consistency,

(iv) constitutive model specifically captures the supra-physiological stress-strain response of human arteries,

(v) all layer-specific material parameters and residual stretches are determined experimentally.

Humphrey and Holzapfel [140] emphasize the necessity to include a non-uniform wall thickness to FE models, a request which is based on experimental results, see, e.g., Raghaven et al. [141].

Addressing our FE modeling framework, our custom meshing algorithm allows a great deal of control in the number and distribution of the hexahedral elements using three input parameters specifying the number of elements in the circumferential θ, axial z and radial r directions. In preliminary computations with different meshes (not shown), we found that the presented mesh gives converged solution for the stress and damage distributions.

In addition, data presented in the literature on the thickness ratios of intima/media/adventitia vary. For example, Holzapfel et al. [24] measured the ratios as 0.21/0.46/0.33 [93], while in our recent study we measured 0.19/0.45/0.36. We studied how varying the thickness ratios of the intima/media/adventitia in our numerical simulations, by up to 25% from our measured values, impacts the predicted stress distributions (while including initial stresses). Our results (not shown) demonstrate that the predicted stress distributions are relatively

insensitive to variations in the thickness ratios within this range. Hence, we present all our results using recently published data [93].

5.4.1 Uniaxial extension of a tissue sample taken from the thoracic aorta

Figure 5.3 shows that accounting for residual stresses in the modeling framework has a significant influence on the predicted transmural stress and damage distributions. As a result, the maximum stresses and damage, both occurring in the intima, decrease. Meanwhile, the stresses and damage in both the media and the adventitia increase, resulting in more homogeneous transmural distributions of stresses and damage. Chuong and Fung [129, 142] and Fung [22] demonstrated that arterial residual stresses tend to homogenize the transmural stress distribution of the tissue in the physiological state. Additionally, numerous studies have shown that the inclusion of residual stresses in analyses of arteries under physiological loading conditions substantially reduces the variation in circumferential and axial stresses within the arterial wall [7, 80, 131, 143–147].

Figure 5.4 and Table 5.4 show that the constitutive model provides an excellent fit to the numerical experiment, and that the resulting material (and damage) parameters are close to the median parameters determined from the corresponding mechanical tests. Thus, our simulation of the three-layer tissue, based on experimentally determined constitutive parameters and residual stretches, can reproduce the mechanical behavior of the intact wall satisfactorily.

5.4.2 Physiological and supra-physiological loadings of the human thoracic aorta

As opposed to the studies of Alastrué et al. [35, 131] we use an iterative procedure to maintain the geometry from medical imaging after applying residual stresses to our model. As Fig. 5.5 demonstrates, the iterative procedure has little impact on the stress distribution but assures that the geometry reconstructed from MRI remains unchanged.

Figure 5.6 compares qualitatively the distributions of the first principal Cauchy stress σ_1 predicted from a classical forward simulation to those including only residual stresses, only prestresses, or including both sources of initial stresses. Without considering residual stresses, i.e. Figs 5.6(a),(b), the intima exhibits unrealistically higher stresses than the media and the adventitia. This effect results from the exponential stiffening of the intimal layer which occurs at much lower stretches compared to the medial and adventitial layers [38, 93]. Residual stresses reduce this discrepancy, as the intima is under compression while both the media and adventitia are under tension in the composite tissue [24]. In fact, we estimate the lowest stress variations along the circumference and through the layers when only residual stresses are included. Compared to the conventional forward computation, inclusion of both prestresses and residual stresses leads to stress distributions that are more uniform through the layers, but higher stress gradients are estimated.

We require prestresses in the modeling framework for theoretical consistency, and have accounted for them using the generalized prestressing algorithm as documented in [128].

Accounting for prestresses generally yields a geometry that has a smaller diameter compared to that predicted from a conventional calculation. Naturally, smaller diameters mean larger local curvatures in the imaged geometry versus the deformed geometry of the classical forward calculation. As a result, the magnitudes and gradients of the Cauchy stresses increase. Our results are consistent with those reported by Putter et al. [117] and Speelman et al. [118], who both conclude that accounting for prestresses in the patient-specific FE simulations leads to an increase in the maximum arterial wall stress. When accounting for initial stresses the first principal stress σ_1 is larger in the adventitia than in the media. Our results differ from those reported in [34], where the authors account only for the opening angle of the medial and adventitial layers, and neglect the mechanical significance of the intima.

Figure 5.7(a) shows the principal Cauchy stresses at the luminal side of the intima along the circumference of the aorta. The predicted stresses along the circumference vary on the order of 100 kPa. Such large variations have also been shown in other studies with patient-specific geometries of arteries, see, e.g., [35, 131, 145, 147], but the circumferential variation of σ_1 in these results was never discussed in detail. Such results are a consequences of the patient-specific geometry where the tissue geometry and thickness is estimated from MRI, however this is not plausible under physiological loads. Experiments suggest that remodeling in healthy arteries aims at maintaining a nearly constant wall stress, e.g., by changing the composition of constituents or the wall thickness [148, 149]. Additionally, the high stress variation contradicts growth and remodeling theories that assume deviation from a uniform homeostatic stress is the principal driver of tissue adaptation [150, 151].

Figure 5.7(b) shows the correlation between the circumferential Cauchy stress and the inner aortic curvature, which is again an artifact of our 3D patient-specific modeling framework. There are several references noting the influence of local curvature on predicted stress results in simulations of aortic aneurysms (see, e.g., [152, 153]), but to the author's knowledge corresponding analysis in healthy human aortas with patient-specific geometries has not yet been reported.

In light of the stress variations highlighted in Fig. 5.7, we suggest to 'precondition' the thoracic aorta with a maximum loading over the history. To this end, Fig. 5.8 compares, for a representative patient-specific simulation of a human thoracic aorta at an internal pressure of $p = 85\,\text{mmHg}$, the circumferential stress in the intima (both at the lumen interface and at the interface with the media) with the circumferential position for results predicted with $p_{\max} = 85\,\text{mmHg}$ in the load history and those predicted with $p_{\max} = 200\,\text{mmHg}$ in the load history. The stress distribution after numerical preconditioning of the tissue, cf. Fig. 5.8(b), yields more realistic results, where the circumferential stresses after numerical preconditioning are in the same range as those reported in, e.g., [7] or [134].

After numerical preconditioning stress gradients inside the tissue decrease, as shown, e.g., in Fig. 5.8. This is a rather pragmatic approach to account for the inhomogeneity of the material parameters or residual stresses within the layers of the tissue. Variations along the

circumferential direction still remain but the transmural stress gradient reduces to almost zero. Such results motivate growth and remodeling schemes for predicting the distribution of material parameters and residual stresses in patient-specific geometries based on the physical principles of remodeling.

Experimental studies, such as Nicosia et al. [154] and Kim and Baek [155], report that the stiffness of aortic tissue varies along the circumferential direction. Thus, we hypothesize that the material parameters might change along the circumference of the aorta in proportion to the local tissue thickness or the local curvature of the tissue. Recently, Reeps et al. [156] found that for abdominal aortic aneurysm wall stiffness and strength correlate with wall thickness. Although this result is derived from diseased tissue, it is possible that the same holds for healthy aortic tissues. Further studies are necessary to better understand intra-patient variation in material parameters, and to reveal correlations between the material parameters and local geometric features such as wall thickness and curvature.

Figure 5.9 shows the distribution of the first principal Cauchy stress after intra-aortic balloon occlusion due to full expansion of the device. We attribute the large stress variations in the contact interface shown in Fig. 5.9(a),(d) to features present in the patient-specific geometry. Hence, simulation of balloon or stent interventions using an idealized geometry, e.g., a cylindrical tube [134], can not lead to a full understanding of the influence of the device inside a patient's artery. The first principal stresses vary notably around the circumferential direction and reach a maximum value of 0.89 MPa at the maximum balloon inflation. This maximum value lies well below the circumferential failure stress for the thoracic aorta of 1.8 MPa, reported in Vorp et al. [157] (cf. also Humphrey and Holzapfel [140]).

Figures 5.9(b),(e) and (c),(f) show the damage increase $\Delta\eta$, based on the damage variable $\eta_{\min}$ at $p = 85$ mmHg. We chose $\eta_{\min}$ at $p = 85$ mmHg as an example reference because the blood pressure during the occlusion procedure is likely lowered due to the effects of anesthesia. There are slight differences in the distribution of $\Delta\eta$ for each family of fibers, however, the overall picture is the same. Contrary to the intima, there is much less damage associated with the fibers present in the media or adventitia.

Figure 5.10 shows the maximum damage increase $\Delta\eta$ versus the diameter of the balloon during the intra-aortic balloon occlusion detailed in Fig. 5.9. Damage is mainly accumulated in the intimal layer, and hence the maximum damage increase $\Delta\eta$ occurs in the intima for all of our representative simulations. This figure is an example of the type of data that can be generated in advance of a specific procedure to help surgeons define thresholds for balloon diameter or balloon pressure.

5.4.3 Limitations

There are some limitations in our modeling framework. When accounting for residual stresses by using the residual stretch data determined experimentally (from Holzapfel et al. [24] and summarized in Table 5.3), we consider only the changes in the dimensions of the separated layers. When the separated layers are fully relaxed, they also have residual

curvatures which are not taken into account here. This simplification may affect the stress distribution through the thickness of each layer, but it should not alter the mean stress values because the stresses resulting from the curvatures can be regarded as bending stresses, thus the mean values should all be about zero.

By focusing specifically on our representative example of the intra-aortic balloon occlusion, we modeled the balloon as a rigid sphere in light of its relatively high stiffness. It would be more informative to accurately model the constitutive behavior of the balloon so that the pressure-diameter response of the device is accurately predicted. Such an approach would improve the insights on surgical procedures employing intra-aortic balloons. However, the focus of this study is to demonstrate the feasibility of the proposed modeling framework to predict stress and damage distributions in aortic tissues using patient-specific geometries, not to accurately model the balloon device.

Our definition of the damage variable η and damage increase $\Delta\eta$ uses a phenomenological approach. More experiments are required to actually get a better physical interpretation of the damage variable and to better understand the evolution of the damage. Nonetheless, we provide a repeatable quantitative measure to help surgeons to better define thresholds for balloon expansion diameter or balloon pressure, ultimately to improve patient outcomes of catheter-based interventions.

5.5 Conclusion

We present a modeling framework to numerically evaluate stress and damage distributions inside the layers of the human aorta of specific patients undergoing surgical procedures. Our constitutive model, including damage associated with the collagen fibers, describes the material behavior in the supra-physiological range, and our FE implementation accounts for both layer-specific residual stresses within the tissue and for prestresses, i.e. the fact that the geometry reconstructed from *in vivo* imaging data is loaded by blood pressure.

Large variations in the stresses and stress gradients, noted especially in the intima, can be explained by the local, patient-specific curvature of the aorta. Such large stress variations are not likely to occur in the tissue in the physiological environment. Thus, we propose to 'precondition' the thoracic aorta by loading up by an internal pressure to 200 mmHg. This is a rather pragmatic approach to account for the inhomogeneity of the material parameters or residual stresses within the layers of the tissue. In the future we suggest either to vary the material parameters or to vary the residual stretches along the circumference of the aorta based on the local curvature or other geometric features.

Our modeling framework, together with the material and structural parameters which are all based on experimental data, can be used to simulate endovascular procedures such as intra-aortic balloon occlusion or stent-graft placement.

Appendix A

A.1 Elasticity Tensor

We first provide more details of the Lagrangian form of the elasticity tensor $\overline{\mathbb{C}}_{\mathrm{f},i}$, $i=4,6$, for each family of fibers, see (5.8)–(5.11). In all that follows the index $i=4,6$ does not employ Einstein summation notation; it refers to a specific family of collagen fibers. Denoting the fictitious elasticity tensor as

$$\tilde{\mathbb{C}}_{\mathrm{f},i} = 4J^{-4/3}\frac{\partial^2\overline{\Psi}^0_{\mathrm{f},i}}{\partial\overline{\mathbf{C}}\partial\overline{\mathbf{C}}} = 4J^{-4/3}\psi''_{\mathrm{f},i}\mathbf{H}_i\otimes\mathbf{H}_i, \tag{A.1}$$

with the Lagrangian structure tensors $\mathbf{H}_4=\kappa\mathbf{I}+(1-3\kappa)\mathbf{M}\otimes\mathbf{M}$ and $\mathbf{H}_6=\kappa\mathbf{I}+(1-3\kappa)\mathbf{M}'\otimes\mathbf{M}'$, and the scalar elasticity function

$$\psi''_{\mathrm{f},i} = k_1[1+2k_2(\overline{I}^*_i-1)^2]\exp[k_2(\overline{I}^*_i-1)^2]. \tag{A.2}$$

The elasticity tensor $\overline{\mathbb{C}}_{\mathrm{f},i}$ can then be written as

$$\begin{aligned}\overline{\mathbb{C}}_{\mathrm{f},i} = {}& \eta_i\mathbb{P}:\tilde{\mathbb{C}}_{\mathrm{f},i}:\mathbb{P}^{\mathrm{T}}+\frac{2}{3}\eta_i\mathrm{Tr}(J^{-2/3}\tilde{\mathbf{S}}^0_{\mathrm{f},i})\tilde{\mathbb{P}}\\ &-\frac{2}{3}\eta_i(\mathbf{C}^{-1}\otimes\overline{\mathbf{S}}^0_{\mathrm{f},i}+\overline{\mathbf{S}}^0_{\mathrm{f},i}\otimes\mathbf{C}^{-1})+\frac{\partial\eta_i}{\partial\overline{\Psi}_{\mathrm{f},i}}\overline{\mathbf{S}}^0_{\mathrm{f},i}\otimes\overline{\mathbf{S}}^0_{\mathrm{f},i},\end{aligned} \tag{A.3}$$

where $\partial\eta_i/\partial\overline{\Psi}_{\mathrm{f},i}$ is according to (5.11), then $\mathrm{Tr}(\cdot)=(\cdot):\mathbf{C}$, $\mathbb{P}=\mathbb{I}-(\mathbf{C}^{-1}\otimes\mathbf{C})/3$ is the Lagrangian projection tensor, $(\mathbb{I})_{KLMN}=(\delta_{KM}\delta_{LN}+\delta_{KN}\delta_{LM})/2$ is the the fourth-order unit tensor, $\tilde{\mathbf{S}}^0_{\mathrm{f},i}=2\partial\overline{\Psi}^0_{\mathrm{f},i}/\partial\overline{\mathbf{C}}$ is the fictitious second Piola-Kirchhoff stress tensor, $\tilde{\mathbb{P}}=\mathbf{C}^{-1}\odot\mathbf{C}^{-1}-(\mathbf{C}^{-1}\otimes\mathbf{C}^{-1})/3$ is a modified projection tensor and $(\mathbf{C}^{-1}\odot\mathbf{C}^{-1})_{KLMN}=(C^{-1}_{KM}C^{-1}_{LN}+C^{-1}_{KN}C^{-1}_{LM})/2$, see [25].

Now we perform the push-forward operation twice to obtain the Eulerian description of the elasticity tensor $\overline{\mathbb{c}}_{\mathrm{f},i}$, which (in index notation) gives

$$(\overline{\mathbb{c}}_{\mathrm{f},i})_{klmn} = \overline{F}_{kK}\overline{F}_{lL}\overline{F}_{mM}\overline{F}_{nN}(\overline{\mathbb{C}}_{\mathrm{f},i})_{KLMN}, \tag{A.4}$$

with the result

$$\begin{aligned}\overline{\mathbb{c}}_{\mathrm{f},i} = {}& \eta_i\mathbb{p}:\tilde{\mathbb{c}}_{\mathrm{f},i}:\mathbb{p}+\frac{2}{3}\eta_i\mathrm{tr}(\tilde{\tau}^0_{\mathrm{f},i})\mathbb{p}\\ &-\frac{2}{3}\eta_i(\mathbf{I}\otimes\overline{\tau}^0_{\mathrm{f},i}+\overline{\tau}^0_{\mathrm{f},i}\otimes\mathbf{I})+\frac{\partial\eta_i}{\partial\overline{\Psi}_{\mathrm{f},i}}\overline{\tau}^0_{\mathrm{f},i}\otimes\overline{\tau}^0_{\mathrm{f},i},\end{aligned} \tag{A.5}$$

where $\mathrm{tr}(\cdot)=(\cdot):\mathbf{I}$, $\tilde{\tau}^0_{\mathrm{f},i}=\overline{\mathbf{F}}\tilde{\mathbf{S}}^0_{\mathrm{f},i}\overline{\mathbf{F}}^{\mathrm{T}}$ is the fictitious Kirchhoff stress tensor, $\mathbb{P}=\mathbb{I}-(\mathbf{I}\otimes\mathbf{I})/3$ is the Eulerian projection tensor and $\mathbb{P}:\tilde{\mathbb{C}}_{\mathrm{f},i}:\mathbb{P}=4J^{-4/3}\psi''_{\mathrm{f},i}(\mathbb{P}:\overline{\mathbf{h}}_i)\otimes(\mathbb{P}:\overline{\mathbf{h}}_i)$, with the Eulerian structure tensors $\overline{\mathbf{h}}_4=\kappa\overline{\mathbf{b}}+(1-3\kappa)\overline{\mathbf{m}}\otimes\overline{\mathbf{m}}$, $\overline{\mathbf{h}}_6=\kappa\overline{\mathbf{b}}+(1-3\kappa)\overline{\mathbf{m}}'\otimes\overline{\mathbf{m}}'$, the modified left Cauchy-Green tensor $\overline{\mathbf{b}}=\overline{\mathbf{F}}\overline{\mathbf{F}}^{\mathrm{T}}$, and $\overline{\mathbf{m}}=\overline{\mathbf{F}}\mathbf{M}$, $\overline{\mathbf{m}}'=\overline{\mathbf{F}}\mathbf{M}'$, while $\psi'_{\mathrm{f},i}$ is according to (A.2). Thus, the Eulerian elasticity tensor consists of four terms, which we write as

$$\overline{\mathbb{c}}_{\mathrm{f},i}=\overline{\mathbb{c}}^1_{\mathrm{f},i}+\overline{\mathbb{c}}^2_{\mathrm{f},i}+\overline{\mathbb{c}}^3_{\mathrm{f},i}+\overline{\mathbb{c}}^4_{\mathrm{f},i}, \tag{A.6}$$

where

$$\overline{\mathbb{c}}^1_{\mathrm{f},i}=\eta_i\mathbb{P}:\tilde{\mathbb{c}}:\mathbb{P}=4\eta_i J^{-4/3}\psi''_{\mathrm{f},i}(\mathbb{P}:\overline{\mathbf{h}}_i)\otimes(\mathbb{P}:\overline{\mathbf{h}}_i), \tag{A.7}$$

$$\overline{\mathbb{c}}^2_{\mathrm{f},i}=\frac{2}{3}\eta_i\mathrm{tr}(\tilde{\tau}^0_{\mathrm{f},i})\mathbb{P}, \tag{A.8}$$

$$\overline{\mathbb{c}}^3_{\mathrm{f},i}=-\frac{2}{3}\eta_i(\mathbf{I}\otimes\overline{\tau}^0_{\mathrm{f},i}+\overline{\tau}^0_{\mathrm{f},i}\otimes\mathbf{I}), \tag{A.9}$$

$$\overline{\mathbb{c}}^4_{\mathrm{f},i}=\frac{\partial\eta_i}{\partial\overline{\Psi}_{\mathrm{f},i}}\overline{\tau}^0_{\mathrm{f},i}\otimes\overline{\tau}^0_{\mathrm{f},i}. \tag{A.10}$$

To facilitate implementation in a FE code we write these terms in matrix notation. We write the matrix quantities consistent with the implementation in FEAP, where the elastic Kirchhoff stress matrix is $[\tilde{\tau}^0_{\mathrm{f},i}]=[\tilde{\tau}^0_{\mathrm{f},i11},\tilde{\tau}^0_{\mathrm{f},i22},\tilde{\tau}^0_{\mathrm{f},i33},\tilde{\tau}^0_{\mathrm{f},i12},\tilde{\tau}^0_{\mathrm{f},i23},\tilde{\tau}^0_{\mathrm{f},i13}]^{\mathrm{T}}$. The deviatoric elastic Kirchhoff stress matrix is

$$[\overline{\tau}^0_{\mathrm{f},i}]=[\tilde{\tau}^0_{\mathrm{f},i11}-\mathrm{tr}(\tilde{\tau}^0_{\mathrm{f},i})/3,\tilde{\tau}^0_{\mathrm{f},i22}-\mathrm{tr}(\tilde{\tau}^0_{\mathrm{f},i})/3,\tilde{\tau}^0_{\mathrm{f},i33}-\mathrm{tr}(\tilde{\tau}^0_{\mathrm{f},i})/3,\tilde{\tau}^0_{\mathrm{f},i12},\tilde{\tau}^0_{\mathrm{f},i23},\tilde{\tau}^0_{\mathrm{f},i13}]^{\mathrm{T}}, \tag{A.11}$$

and the projection of the Eulerian structure tensor gives

$$[\mathbb{P}:\overline{\mathbf{h}}_i]=\begin{bmatrix}\overline{h}_{11}-\mathrm{tr}(\overline{\mathbf{h}}_i)/3\\ \overline{h}_{22}-\mathrm{tr}(\overline{\mathbf{h}}_i)/3\\ \overline{h}_{33}-\mathrm{tr}(\overline{\mathbf{h}}_i)/3\\ \overline{h}_{12}\\ \overline{h}_{23}\\ \overline{h}_{13}\end{bmatrix}=\begin{bmatrix}(p\overline{h})_1\\ (p\overline{h})_2\\ (p\overline{h})_3\\ (p\overline{h})_4\\ (p\overline{h})_5\\ (p\overline{h})_6\end{bmatrix}. \tag{A.12}$$

The four terms of the Eulerian elasticity tensor are thus

$$[\overline{\mathbb{c}}^1_{\mathrm{f},i}]=4\eta_i J^{-4/3}\psi''_{\mathrm{f},i}$$

$$\begin{bmatrix}(p\overline{h})^2_1 & (p\overline{h})_1(p\overline{h})_2 & (p\overline{h})_1(p\overline{h})_3 & (p\overline{h})_1(p\overline{h})_4 & (p\overline{h})_1(p\overline{h})_5 & (p\overline{h})_1(p\overline{h})_6\\ & (ph)^2_2 & (ph)_2(ph)_3 & (ph)_2(ph)_4 & (ph)_2(ph)_5 & (ph)_2(ph)_6\\ & & (ph)^2_3 & (ph)_3(ph)_4 & (ph)_3(ph)_5 & (ph)_3(ph)_6\\ & & & (ph)^2_4 & (ph)_4(ph)_5 & (ph)_4(ph)_6\\ & \mathrm{sym} & & & (ph)^2_5 & (ph)_5(ph)_6\\ & & & & & (ph)^2_6\end{bmatrix}, \tag{A.13}$$

$$[\overline{\mathbb{C}}^2_{\mathrm{f},i}] = \frac{2}{3}\eta_i \mathrm{tr}(\tilde{\tau}^0_{\mathrm{f},i}) \begin{bmatrix} 2/3 & -1/3 & -1/3 & 0 & 0 & 0 \\ & 2/3 & -1/3 & 0 & 0 & 0 \\ & & 2/3 & 0 & 0 & 0 \\ & & & 1/2 & 0 & 0 \\ & \mathrm{sym} & & & 1/2 & 0 \\ & & & & & 1/2 \end{bmatrix}, \tag{A.14}$$

$$[\overline{\mathbb{C}}^3_{\mathrm{f},i}] = -\frac{2}{3}\eta_i \begin{bmatrix} 2\overline{\tau}^0_{\mathrm{f},i11} & \overline{\tau}^0_{\mathrm{f},i11}+\overline{\tau}^0_{\mathrm{f},i22} & \overline{\tau}^0_{\mathrm{f},i11}+\overline{\tau}^0_{\mathrm{f},i33} & \overline{\tau}^0_{\mathrm{f},i12} & \overline{\tau}^0_{\mathrm{f},i23} & \overline{\tau}^0_{\mathrm{f},i13} \\ & 2\overline{\tau}^0_{\mathrm{f},i22} & \overline{\tau}^0_{\mathrm{f},i22}+\overline{\tau}^0_{\mathrm{f},i33} & \overline{\tau}^0_{\mathrm{f},i12} & \overline{\tau}^0_{\mathrm{f},i23} & \overline{\tau}^0_{\mathrm{f},i13} \\ & & 2\overline{\tau}^0_{\mathrm{f},i33} & \overline{\tau}^0_{\mathrm{f},i12} & \overline{\tau}^0_{\mathrm{f},i23} & \overline{\tau}^0_{\mathrm{f},i13} \\ & & & 0 & 0 & 0 \\ & \mathrm{sym} & & & 0 & 0 \\ & & & & & 0 \end{bmatrix}, \tag{A.15}$$

and

$$[\overline{\mathbb{C}}^4_{\mathrm{f},i}] = \frac{\partial \eta_i}{\partial \overline{\Psi}_{\mathrm{f},i}} \begin{bmatrix} \overline{\tau}^{0\,2}_{\mathrm{f},i11} & \overline{\tau}^0_{\mathrm{f},i11}\overline{\tau}^0_{\mathrm{f},i22} & \overline{\tau}^0_{\mathrm{f},i11}\overline{\tau}^0_{\mathrm{f},i33} & \overline{\tau}^0_{\mathrm{f},i11}\overline{\tau}^0_{\mathrm{f},i12} & \overline{\tau}^0_{\mathrm{f},i11}\overline{\tau}^0_{\mathrm{f},i23} & \overline{\tau}^0_{\mathrm{f},i11}\overline{\tau}^0_{\mathrm{f},i13} \\ & \overline{\tau}^{0\,2}_{\mathrm{f},i22} & \overline{\tau}^0_{\mathrm{f},i22}\overline{\tau}^0_{\mathrm{f},i33} & \overline{\tau}^0_{\mathrm{f},i22}\overline{\tau}^0_{\mathrm{f},i12} & \overline{\tau}^0_{\mathrm{f},i22}\overline{\tau}^0_{\mathrm{f},i23} & \overline{\tau}^0_{\mathrm{f},i22}\overline{\tau}^0_{\mathrm{f},i13} \\ & & \overline{\tau}^{0\,2}_{\mathrm{f},i33} & \overline{\tau}^0_{\mathrm{f},i33}\overline{\tau}^0_{\mathrm{f},i12} & \overline{\tau}^0_{\mathrm{f},i33}\overline{\tau}^0_{\mathrm{f},i23} & \overline{\tau}^0_{\mathrm{f},i33}\overline{\tau}^0_{\mathrm{f},i13} \\ & & & \overline{\tau}^{0\,2}_{\mathrm{f},i12} & \overline{\tau}^0_{\mathrm{f},i12}\overline{\tau}^0_{\mathrm{f},i23} & \overline{\tau}^0_{\mathrm{f},i12}\overline{\tau}^0_{\mathrm{f},i13} \\ & \mathrm{sym} & & & \overline{\tau}^{0\,2}_{\mathrm{f},i23} & \overline{\tau}^0_{\mathrm{f},i23}\overline{\tau}^0_{\mathrm{f},i13} \\ & & & & & \overline{\tau}^{0\,2}_{\mathrm{f},i13} \end{bmatrix}. \tag{A.16}$$

REFERENCES

[1] Allam AH, Thompson RC, Wann LS, Miyamoto MI, Nur el Din AeH, el Maksoud GA, Al-Tohamy Soliman M, Badr I, el Rahman Amer HA, Sutherland ML, Sutherland JD, Thomas GS. Atherosclerosis in ancient Egyptian mummies: The horus study. *JACC: Cardiovasc. Imaging* 2011; **4**:315–327.

[2] European Heart Network. *European Cardiovascular Disease Statistics*. *http://www.ehnheart.org/cvd-statistics.html*, 2012.

[3] Roger VL, Go AS, Lloyd-Jones DM, Benjamin EJ, Berry JD, Borden WB, Bravata DM, Dai S, Ford ES, Fox CS, Fullerton HJ, Gillespie C, Hailpern SM, Heit JA, Howard VJ, Kissela BM, Kittner SJ, Lackland DT, Lichtman JH, Lisabeth LD, Makuc DM, Marcus GM, Marelli A, Matchar DB, Moy CS, Mozaffarian D, Mussolino ME, Nichol G, Paynter NP, Soliman EZ, Sorlie PD, Sotoodehnia N, Turan TN, Virani SS, Wong ND, Woo D, Turner MB. Executive summary: Heart disease and stroke statistics – 2012 update: A report from the American Heart Association. *Circulation* 2012; **125**:188–197.

[4] Wang L, Kong L, Wu F, Bai Y, Burton R. Preventing chronic diseases in China. *The Lancet* 2005; **366**:1821–1824.

[5] Qureshi MA, Conway BD, Greenberg RK. Thoracic aortic aneurysms-clinical assessment and treatment. *Biomechanics and Mechanobiology of Aneurysms*, McGloughlin T (ed.). Springer: Heidelberg, 2011; 285–329.

[6] Rhodin JAG. Architecture of the vessel wall. *Handbook of Physiology, Section 2, Volume 2*, Berne RM (ed.). Am Physiol Soc: Bethesda, 1979.

[7] Holzapfel GA, Gasser TC, Ogden RW. A new constitutive framework for arterial wall mechanics and a comparative study of material models. *J. Elasticity* 2000; **61**:1–48.

[8] Mithieux SM, Weiss AS. Elastin. *Adv. Protein Chem.* 2005; **70**:437–461.

[9] Gotte L, Giro M, Volpin D, Horne R. The ultrastructural organization of elastin. *J. Ultrastruct. Res.* 1974; **46**:23–33.

[10] Horn F, Armbruster M, Berghold S, Blaeschke F, Grillhösl C, Helferich S, Moc I, Pritsch M, Schneider N, Ziegler P. *Biochemie des Menschen*. Thieme, 2009.

[11] Fratzl P (ed.). *Collagen. Structure and Mechanics*. Springer: New York, 2008.

[12] von der Mark K. Localization of collagen types in tissues. *Int. Rev. Conn. Tiss. Res.* 1981; **9**:265–324.

[13] Voet D, Voet JG, Pratt CW. *Lehrbuch der Biochemie*. Wiley, 2010.

[14] Azeloglu EU, Albro MB, Thimmappa VA, Ateshian GA, Costa KD. Heterogeneous transmural proteoglycan distribution provides a mechanism for regulating residual stresses in the aorta. *Am. J. Physiol. Heart Circ. Physiol.* 2008; **294**:H1197–H1205.

[15] Gasser CT. An irreversible constitutive model for fibrous soft biological tissue: A 3-D microfiber approach with demonstrative application to abdominal aortic aneurysms. *Acta Biomater.* 2011; **7**:2457–2466.

[16] Murtada S, Kroon M, Holzapfel GA. A calcium–driven mechanochemical model for prediction of force generation in smooth muscle. *Biomech. Model. Mechanobiol.* 2010; **9**:749–762.

[17] Murtada S, Kroon M, Holzapfel GA. Modeling the dispersion effects of contractile fibers in smooth muscles. *J. Mech. Phys. Solids* 2010; **58**:2065–2082.

[18] Stålhand J, Klarbring A, Holzapfel GA. Smooth muscle contraction: mechanochemical formulation for homogeneous finite strains. *Prog. Biophys. Mol. Biol.* 2008; **96**:465–481.

[19] Stålhand J, Klarbring A, Holzapfel GA. A mechanochemical 3D continuum model for smooth muscle contraction under finite strains. *J. Theor. Biol.* 2011; **268**:120–130.

[20] Lawton RW. The thermoelastic behavior of isolated aortic strips of the dog. *Circ. Res.* 1954; **2**:344–353.

[21] Carew TE, Vaishnav RN, Patel DJ. Compressibility of the arterial wall. *Circ. Res.* 1968; **23**:61–68.

[22] Fung YC. What are the residual stresses doing in our blood vessels? *Ann. Biomed. Eng.* 1991; **19**:237–249.

[23] Fonck E, Prod'hom G, Roy S, Augsburger L, Rüfenacht DA, Stergiopulos N. Effects of elastin degradation on carotid wall mechanics as assessed by a constituent-based biomechanical model. *Am. J. Physiol. Heart Circ. Physiol.* 2007; **292**:H2754–H2763.

[24] Holzapfel GA, Sommer G, Auer M, Regitnig P, Ogden RW. Layer-specific 3D residual deformations of human aortas with non-atherosclerotic intimal thickening. *Ann. Biomed. Eng.* 2007; **35**:530–545.

[25] Holzapfel GA. *Nonlinear Solid Mechanics. A Continuum Approach for Engineering*. John Wiley & Sons: Chichester, 2000.

[26] Bathe KJ. *Finite Element Procedures*. Prentice-Hall: Englewood Cliffs, New Jersey, 1996.

[27] Zienkiewicz OC, Taylor RL. *The Finite Element Method. Solid Mechanics*, vol. 2. 5th edn., Butterworth Heinemann: Oxford, 2000.

[28] Taylor RL. *FEAP – A Finite Element Analysis Program, Version 8.2 Theory Manual*. University of California at Berkeley, Berkeley, California, 2009.

[29] Gee MW, Reeps C, Eckstein GG, Wall WA. Prestressing in finite deformation abdominal aortic aneurysm simulation. *J. Biomech.* 2009; **42**:1732–1739.

[30] Gee MW, Förster C, Wall WA. A computational strategy for prestressing patient-specific biomechanical problems under finite deformation. *Int. J. Numer. Method Biomed. Eng.* 2010; **26**:52–72.

[31] Schield RT. Inverse deformation results in finite elasticity. *Z. Angew. Math. Phys.* 1967; **18**:490–500.

[32] Govindjee S, Mihalic PA. Computational methods for inverse finite elastostatics. *Comput. Meth. Appl. Mech. Eng.* 1996; **136**:47–57.

[33] Balzani D, Schröder J, Gross D. Simulation of discontinuous damage incorporating residual stresses in circumferentially overstretched atherosclerotic arteries. *Acta Biomater.* 2006; **2**:609–618.

[34] Holzapfel GA, Gasser CT. Computational stress–deformation analysis of arterial walls including high-pressure response. *Int. J. Cardiol.* 2007; **116**:78–85.

[35] Alastrué V, Peña E, Martínez MA, Doblaré M. Assessing the use of the 'Opening Angle Method' to enforce residual stresses in patient-specific arteries. *Ann. Biomed. Eng.* 2007; **35**:1821–1837.

[36] Holzapfel GA, Mulvihill JJ, Cunnane EM, Walsh MT. Computational approaches for analyzing the mechanics of atherosclerotic plaques: A review. *J. Biomech.* 2014; in press.

[37] Finlay HM, McCullough L, Canham PB. Three-dimensional collagen organization of human brain arteries at different transmural pressures. *J. Vasc. Res.* 1995; **32**:301–312.

[38] Holzapfel GA, Sommer G, Gasser CT, Regitnig P. Determination of the layer-specific mechanical properties of human coronary arteries with non-atherosclerotic intimal thickening, and related constitutive modelling. *Am. J. Physiol. Heart Circ. Physiol.* 2005; **289**:H2048–2058.

[39] Gasser TC, Ogden RW, Holzapfel GA. Hyperelastic modelling of arterial layers with distributed collagen fibre orientations. *J. R. Soc. Interface* 2006; **3**:15–35.

[40] Schriefl AJ, Zeindlinger G, Pierce DM, Regitnig P, Holzapfel GA. Determination of the layer-specific distributed collagen fiber orientations in human thoracic and abdominal aortas and common iliac arteries. *J. R. Soc. Interface* 2012; **9**:1275–1286.

[41] Schriefl AJ, Wolinski H, Regitnig P, Kohlwein SD, Holzapfel GA. An automated approach for 3d quantification of fibrillar structures in optically cleared soft biological tissues. *J. R. Soc. Interface* 2013; **10**:20120 760.

[42] Gasser TC, Gallinetti S, Xing X, Forsell C, Swedenborg J, Roy J. Spatial orientation of collagen fibers in the abdominal aortic aneurysm's wall and its relation to wall mechanics. *Acta Biomater.* 2012; **8**:3091–3103.

[43] Rodríguez JF, Cacho F, Bea JA, Doblaré M. A stochastic-structurally based three dimensional finite-strain damage model for fibrous soft tissue. *J. Mech. Phys. Solids* 2006; **54**:864–886.

[44] Li D, Robertson AM. A structural multi-mechanism constitutive equation for cerebral arterial tissue. *Int. J. Solids Structures* 2009; **46**:2920–2928.

[45] Simo JC. On a fully three-dimensional finite-strain viscoelastic damage model: Formulation and computational aspects. *Comput. Meth. Appl. Mech. Eng.* 1987; **60**:153–173.

[46] Miehe C. Discontinuous and continuous damage evolution in ogden-type large-strain elastic materials. *Eur. J. Mech. A/Solids* 1995; **14**:697–720.

[47] Pena E, Doblare M. An anisotropic pseudo-elastic approach for modelling Mullins effect in fibrous biological materials. *Mech. Res. Commun.* 2009; **36**:784–790.

[48] Ogden RW, Roxburgh DG. A pseudo-elastic model for the Mullins effect in filled rubber. *Proc. R. Soc. Lond. A* 1999; **455**:2861–2877.

[49] Dorfmann A, Ogden RW. A constitutive model for the Mullins effect with permanent set in particle-reinforced rubber. *Int. J. Solids Structures* 2004; **41**:1855–1878.

[50] Guo Z, Sluys LJ. Computational modelling of the stress-softening phenomenon of rupbber-like materials under cyclic loading. *Eur. J. Mech. A/Solids* 2006; **25**:887–896.

[51] Lanir Y. Constitutive equations for fibrous connective tissues. *J. Biomech.* 1983; **16**:1–12.

[52] Miehe C, Göktepe S, Lulei F. A micro-macro approach to rubber-like materials – Part I: The non-affine micro-sphere model of rubber elasticity. *J. Mech. Phys. Solids* 2004; **52**:2617–2660.

[53] Chandran PL, Barocas VH. Deterministic material-based averaging theory model of collagen gel micromechanics. *J. Biomech. Eng.* 2007; **129**:137–147.

[54] Oktay HS, Kang T, Humphrey JD, Bishop GG. Changes in the mechanical behavior of arteries following balloon angioplasty. *ASME 1991 Biomechanics Symposium, AMD – Vol. 120*, Spilker RL, Friedman MH (eds.), The American Society of Mechanical Engineers, 1991.

[55] Horný L, Gultová E, Chlup H, Sedláček H, Kronek J, Veselý J, Žitný R. Mullins effect in aorta and limiting extensibility evolution. *Bulletin of Applied Mechanics* 2010; **6**:1–5.

[56] Famaey N, Verbeken E, Vinckier S, Willaert B, Herijgers P, Vander Sloten J. In vivo soft tissue damage assessment for applications in surgery. *Med. Eng. Phys.* 2010; **32**:437–443.

[57] Movat HZ, More RH, Haust MD. The diffuse intimal thickening of the human aorta with aging. *Am. J. Pathol.* 1958; **34**:1023–1031.

[58] Hokanson J, Yazdani S. A constitutive model of the artery with damage. *Mech. Res. Commun.* 1997; **24**:151–159.

[59] Balzani D. Polyconvex anisotropic energies and modeling of damage applied to arterial walls. PhD Thesis, Universität Duisburg-Essen 2006.

[60] Balzani D, Brinkhues S, Holzapfel GA. Constitutive framework for the modeling of damage in collagenous soft tissues with application to arterial walls. *Comput. Meth. Appl. Mech. Eng.* 2012; **213–216**:139–151.

[61] Marini G, Maier A, Reeps C, Eckstein HH, Wall WA, Gee MW. A continuum description of the damage process in the arterial wall of abdominal aortic aneurysms. *Int. J. Numer. Method Biomed. Eng.* 2012; **28**:87–99.

[62] Rodríguez JF, Alastrué V, Doblaré M. Finite element implementation of a stochastic three dimensional finite-strain damage model for fibrous soft tissue. *Comput. Meth. Appl. Mech. Eng.* 2008; **197**:946–958.

[63] Calvo B, Peña M, Martinez MA, Doblaré M. An uncoupled directional damage model for fibred biological soft tissues. Formulation and computational aspects. *Int. J. Numer. Meth. Engng* 2007; **69**:2036–2057.

[64] Alastrué V, Rodríguez JF, Calvo B, Doblaré M. Structural damage models for fibrous biological soft tissues. *Int. J. Solids Structures* 2007; **44**:5894–5911.

[65] Li D, Robertson AM. A structural multi-mechanism damage model for celebral arterial tissue. *J. Biomech. Eng.* 2009; **131**:101 013–1.

[66] Peña E, A J, Peña, M, Doblaré. On the Mullins effect and hysteresis of fibered biological materials: A comparison between continuous and discontinuous damage models. *Int. J. Solids Structures* 2009; **46**:1727–1735.

[67] Peña E, Calvo B, Martínez MA, Doblaré M. On finite-strain damage of viscoelastic-fibred materials. Application to soft biological tissues. *Int. J. Numer. Meth. Engng* 2008; **74**:1198–1218.

[68] Peña E, Alastrué V, Laborda A, Matrínez MA, Doblaré M. A constitutive formulation of vascular tissue mechanics including viscoelasticity and softening behaviour. *J. Biomech.* 2010; **43**:984–989.

[69] Peña E. Prediction of the softening and damage effects with permanent set in fibrous biological materials. *Int. J. Solids Structures* 2011; **59**:1808–1822.

[70] Famaey N, Sommer G, Vander Sloten J, Holzapfel GA. Arterial clamping: Finite element simulation and in vivo validation. *J. Mech. Behav. Biomed. Mater.* 2012; **12**:107–118.

[71] Colombo A, Guha S, Mackle J, Cahill P, Lally C. Cyclic strain amplitude dictates the growth response of vascular smooth muscle cells in vitro: role in in-stent restenosis and inhibition with a sirolimus drug-eluting stent. *Biomech. Model. Mechanobiol.* 2012; **12**:671–683.

[72] Kuo KH, Herrera AM, Wang L, Paré PD, Ford LE, Stephens NL, Seow CY. Structure-function correlation in airway smooth muscle adapted to different lengths. *Am. J. Physiol. Cell Physiol.* 2003; **285**:C384–C390.

[73] Bossé Y, Sobieszek A, Paré PD, Seow CY. Length adaptation of airway smooth muscle. *Proc. Am. Thorac. Soc.* 2008; **5**:62–67.

[74] Sáez P, Alastrué V, Peña E, Doblaré M, Martínez M. Anisotropic microsphere-based approach to damage in soft fibered tissue. *Biomech. Model. Mechanobiol.* 2012; **11**:595–608.

[75] Hadi MF, Sander EA, Barocas VH. Multiscale model predicts tissue-level failure from collagen fiber-level damage. *J. Biomech. Eng.* 2012; **134**:091 005.

[76] European Heart Network. *European Cardiovascular Disease Statistics 2008. http://www.epha.org/a/2920*, 2008.

[77] Holzapfel GA. Determination of material models for arterial walls from uniaxial extension tests and histological structure. *J. Theor. Biol.* 2006; **238**:290–302.

[78] Balzani D, Neff P, Schröder J, Holzapfel GA. A polyconvex framework for soft biological tissues. adjustment to experimental data. *Int. J. Solids Structures* 2006; **43**:6052–6070.

[79] Rodríguez JF, Alastrue V, Doblaré M. Finite element implementation of a stochastic three dimensional finite-strain damage model for fibrous soft tissue. *Comput. Meth. Appl. Mech. Eng.* 2008; **197**:946–958.

[80] Humphrey JD. *Cardiovascular Solid Mechanics. Cells, Tissues, and Organs*. Springer-Verlag: New York, 2002.

[81] Flory PJ. Thermodynamic relations for highly elastic materials. *Trans. Faraday Soc.* 1961; **57**:829–838.

[82] Beatty MF, Krishnaswamy S. The Mullins effect in equibiaxial deformation. *Zeitschrift f. Angew. Math. Phys.* 2000; **51**:984–1015.

[83] Elías-Zúñuiga A. A phenomenological energy-based model to characterize stress-softening effect in elastomers. *Polymer* 2005; **46**:3496–3506.

[84] Holzapfel GA, Weizsäcker HW. Biomechanical behavior of the arterial wall and its numerical characterization. *Comp. Biol. Med.* 1998; **28**:377–392.

[85] Sommer G, Regitnig P, Költringer L, Holzapfel GA. Biaxial mechanical properties of intact and layer – dissected human carotid arteries at physiological and supra-physiological loadings. *Am. J. Physiol. Heart Circ. Physiol.* 2010; **298**:H898–912.

[86] Ogden RW, Saccomandi G, Sgura I. Fitting hyperelastic models to experimental data. *Comput. Mech.* 2004; **34**:484–502.

[87] Wilens SL. The nature of diffuse intimal thickening of arteries. *Am. J. Pathol.* 1951; **27**:825–839.

[88] Bader H. Dependence of wall stress in the human thoracic aorta on age and pressure. *Circ. Res.* 1967; **20**:354–361.

[89] Greenwald SE. Ageing of the conduit arteries. *J. Pathol.* 2007; **211**:157–172.

[90] Haskett D, Johnson G, Zhou A, Utzinger U, Vande Geest J. Microstructural and biomechanical alterations of the human aorta as a function of age and location. *Biomech. Model. Mechanobiol.* 2010; **9**:725–736.

[91] Benetos A, Laurent S, Hoeks AP, Boutouyrie PH, Safar ME. Arterial alterations with aging and high blood pressure. A noninvasive study of carotid and femoral arteries. *Arterioscler. Thromb. Vasc. Biol.* 1993; **13**:90–97.

[92] Schwartz RS, Huber KC, Murphy JG, Edwards WD, Camrud AR, Vliestra RE, Holmes DR. Restenosis and proportional neointimal response to coronary artery injury: results in a porcine model. *J. Am. Coll. Cardiol.* 1992; **19**:267–274.

[93] Weisbecker H, Pierce DM, Regitnig P, Holzapfel GA. Layer-specific damage experiments and modeling of human thoracic and abdominal aortas with non-atherosclerotic intimal thickening. *J. Mech. Behav. Biomed. Mater.* 2012; **12**:93–106.

[94] Roach MR, Burton AC. The reason for the shape of the distensibility curves of arteries. *Canad. J. Biochem. Physiol.* 1957; **35**:681–690.

[95] Dobrin PB, Baker WH, Gley WC. Elastolytic and collagenolytic studies of arteries. Implications for the mechanical properties of aneurysms. *Arch. Surg.* 1984; **119**:405–409.

[96] Dobrin PB, Canfield TR. Elastase, collagenase, and the biaxial elastic properties of dog carotid artery. *Am. J. Physiol.* 1984; **247**:H124–H131.

[97] Gundiah N, Ratcliffe MB, Pruitt LA. Determination of strain energy function for arterial elastin: Experiments using histology and mechanical tests. *J. Biomech.* 2007; **40**:586–594.

[98] Gundiah N, Ratcliffe MB, Pruitt LA. The biomechanics of arterial elastin. *J. Mech. Behav. Biomed. Mater.* 2009; **2**:288–296.

[99] Lillie M, Shadwick R, Gosline J. Mechanical anisotropy of inflated elastic tissue from the pig aorta. *J. Biomech.* 2010; **43**:2070–2078.

[100] Zou Y, Zhang Y. An experimental and theoretical study on the anisotropy of elastin network. *Ann. Biomed. Eng.* 2009; **37**:1572–1583.

[101] Zou Y, Zhang Y. The orthotropic viscoelastic behavior of aortic elastin. *Biomech. Model. Mechanobiol.* 2011; **10**:613–625.

[102] Waldman SD, Michael Lee J. Boundary conditions during biaxial testing of planar connective tissues. Part 1: Dynamic behavior. *J. Mater. Sci. Mater. Med.* 2002; **13**:933–938.

[103] Sun W, Sacks MS, Scott MJ. Effects of boundary conditions on the estimation of the planar biaxial mechanical properties of soft tissues. *J. Biomech. Eng.* 2005; **127**:709–715.

[104] Kratzberg JA, Walker PJ, Rikkers E, Raghavan ML. The effect of proteolytic treatment on plastic deformation of porcine aortic tissue. *J. Mech. Behav. Biomed. Mater.* 2009; **2**:65–72.

[105] Labrosse MR, Beller CJ, Mesana T, Veinot JP. Mechanical behavior of human aortas: Experiments, material constants and 3-D finite element modeling including residual stress. *J. Biomech.* 2009; **42**:996–1004.

[106] Holzapfel GA, Sommer G, Regitnig P. Anisotropic mechanical properties of tissue components in human atherosclerotic plaques. *J. Biomech. Eng.* 2004; **126**:657–665.

[107] Watton PN, Ventikos Y, Holzapfel GA. Modelling the mechanical response of elastin for arterial tissue. *J. Biomech.* 2009; **42**:1320–1325.

[108] Clark JM, Glagov S. Transmural organization of the arterial media: The lamellar unit revisited. *Arteriosclerosis* 1985; **5**:19–34.

[109] Missirlis YF. Use of enzymolysis techniques in studying mechanical properties of connective tissue componentes. *J. Bioeng.* 1977; **1**:215–222.

[110] Kronick PL, Sacks MS. Matrix macromolecules that affect the viscoelasticity of calfskin. *J. Biomech. Eng.* 1994; **116**:140–145.

[111] Chadwick P. Applications of an energy-momentum tensor in non-linear elastostatics. *J. Elasticity* 1975; **5**:249–258.

[112] Govindjee S, Mihalic PA. Computational methods for inverse deformations in quasi-incompressible finite elasticity. *Int. J. Numer. Meth. Engng* 1998; **43**:821–838.

[113] Fachinotti V, Cardona A, Jetteur P. Finite element modelling of inverse design problems in large deformation anisotropic hyperelasticity. *Int. J. Numer. Meth. Engng* 2008; **74**:894–910.

[114] Lu J, Zhou X, Raghavan ML. Inverse elastostatic stress analysis in pre-deformed biological structures: Demonstration using abdominal aortic aneurysms. *J. Biomech.* 2007; **40**:693–696.

[115] Lu J, Zhou X, Raghavan M. Inverse method of stress analysis for cerebral aneurysms. *Biomech. Model. Mechanobiol.* 2008; **7**:477–486.

[116] Kroon M, Holzapfel GA. Elastic properties of anisotropic vascular membranes examined by inverse analysis. *Comput. Meth. Appl. Mech. Eng.* 2009; **198**:3622–3632.

[117] de Putter S, Wolters BJBM, Rutten MCM, Breeuwer M, Gerritsen FA, van de Vosse FN. Patient-specific initial wall stress in abdominal aortic aneurysms with a backward incremental method. *J. Biomech.* 2007; **40**:1081–1090.

[118] Speelman L, Bosboom EMH, Schurink GWH, Buth J, Breeuwer M, Jacobs MJ, van de Vosse FN. Initial stress and nonlinear material behavior in patient-specific AAA wall stress analysis. *J. Biomech.* 2009; **42**:1713–1719.

[119] Raghavan ML, Ma B, Fillinger M. Non-invasive determination of zero-pressure geometry of arterial aneurysms. *Ann. Biomed. Eng.* 2006; **34**:1414–1419.

[120] Tarjuelo-Gutiérrez J, Rodriguez-Vila B, Pierce DM, Fastl TE, Vergrugghe P, Fourneau I, Maleux G, Herijgers P, Holzapfel GA, Gómez E. High-quality conforming hexahedral meshes of patient-specific abdominal aortic aneurysms including their intraluminal thrombi. *Med. Biol. Eng. Comput.* 2014; **52**:159–168.

[121] Kiousis DE, Rubinigg SF, Auer M, Holzapfel GA. A methodology to analyze changes in lipid core and calcification onto fibrous cap vulnerability: The human atherosclerotic carotid bifurcation as an illustratory example. *J. Biomech. Eng.* 2009; **131**:121 002.

[122] Labrosse MR, Gerson ER, Veinot JP, Beller CJ. Mechanical characterization of human aortas from pressurization testing and a paradigm shift for circumferential residual stress. *J. Mech. Behav. Biomed. Mater.* 2013; **17**:44–55.

[123] Martinelli T, Thony F, Decléty P, Sengel C, Broux C, Tonetti J, Payen JF, Ferretti G. Intra-aortic balloon occlusion to salvage patients with life-threatening hemorrhagic shocks from pelvic fractures. *J. Trauma* 2010; **68**:942–948.

[124] Fernandez JD, Craig JM, Garrett Jr HE, Burgar SR, Bush AJ. Endovascular management of iliac rupture during endovascular aneurysm repair. *J. Vasc. Surg.* 2009; **50**:1293–1300.

[125] Assar AN, Zarins CK. Endovascular proximal control of ruptured abdominal aortic aneurysms: the internal aortic clamp. *J. Cardiovasc. Surg.* 2009; **50**:381–385.

[126] Malina M, Veith F, Ivancev K, Sonesson B. Balloon occlusion of the aorta during endovascular repair of ruptured abdominal aortic aneurysm. *J. Endovasc. Ther.* 2005; **12**:556–559.

[127] Karkos CD, Bruce IA, Lambert ME. Use of the intra-aortic balloon pump to stop gastrointestinal bleeding. *Ann. Emerg. Med.* 2001; **38**:328–331.

[128] Weisbecker H, Pierce DM, Holzapfel GA. A generalized prestressing algorithm for finite element simulations on pre-loaded geometries with application to the aorta. *Int. J. Numer. Method Biomed. Eng.* 2014; in press.

[129] Chuong CJ, Fung YC. On residual stress in arteries. *J. Biomech. Eng.* 1986; **108**:189–192.

[130] Bustamante R, Holzapfel GA. Methods to compute 3D residual stress distributions in hyperelastic tubes with application to arterial walls. *Int. J. Eng. Sci.* 2010; **48**:1066–1082.

[131] Alastrué V, Garía A, Peña E, Rodríguez JF, Martínez MA, Doblaré M. Numerical framework for patient-specific computational modelling of vascular tissue. *Int. J. Numer. Meth. Biomed. Engng.* 2010; **26**:35–51.

[132] Natali AN, Pavan PG, Carniel EL, Dorow C. A transversally isotropic elasto-damage constitutive model for the periodontal ligament. *Comput. Methods Biomech. Biomed. Engin.* 2003; **6**:329–336.

[133] Ehret AE, Itskov M. Modeling of anisotropic softening phenomena: Application to soft biological tissues. *Int. J. Plasticity* 2009; **25**:901–919.

[134] Li D, Robertson AM, Lin G, Lovell M. Finite element modeling of cerebral angioplasty using a structural multi-mechanism anisotropic damage model. *Int. J. Numer. Method Biomed. Eng.* 2012; **92**:457–474.

[135] Weisbecker H, Viertler C, Pierce DM, Holzapfel GA. The role of elastin and collagen in the softening behavior of the human aortic media 2013; **46**:1859–1865.

[136] Miehe C. Multisurface thermoplasticity for single crystals at large strains in terms of Eulerian vector updates. *Int. J. Solids Structures* 1996; **33**:3103–3130.

[137] MacDougall JD, Tuxen D, Sale DG, Moroz JR, Sutton JR. Arterial blood pressure response to heavy resistance exercise. *J. Appl. Phys.* 1985; **58**:785–790.

[138] Kiousis DE, Wulff A, Holzapfel GA. Experimental studies and numerical analysis of the inflation and interaction of vascular balloon catheter-stent systems. *Ann. Biomed. Eng.* 2009; **37**:315–330.

[139] Gorry PA. General least-squares smoothing and differentiation of nonuniformly spaced data by the convolution method. *Anal. Chem.* 1991; **63**:534–536.

[140] Humphrey JD, Holzapfel GA. Mechanics, mechanobiology, and modeling of human abdominal aorta and aneurysms. *J. Biomech.* 2012; **45**:805–814.

[141] Raghavan ML, Kratzberg J, Castro de Tolosa EM, Hanaoka MM, Walker P, da Silva ES. Regional distribution of wall thickness and failure properties of human abdominal aortic aneurysm. *J. Biomech.* 2006; **39**:3010–3016.

[142] Chuong CJ, Fung YC. Three-dimensional stress distribution in arteries. *J. Biomech. Eng.* 1983; **105**:268–274.

[143] Vaishnav RN, Vossoughi J. Residual stress and strain in aortic segments. *J. Biomech.* 1987; **20**:235–239.

[144] Matsumoto T, Hayashi K. Stress and strain distribution in hypertensive and normotensive rat aorta considering residual strain. *J. Biomech.* 1996; **118**:62–73.

[145] Delfino A, Stergiopulos N, Moore Jr JE, Meister JJ. Residual strain effects on the stress field in a thick wall finite element model of the human carotid bifurcation. *J. Biomech.* 1997; **30**:777–786.

[146] Peterson SJ, Okamoto RJ. Effect of residual stress and heterogeneity on circumferential stress in the arterial wall. *J. Biomech. Eng.* 2000; **122**:454–456.

[147] Raghavan ML, Trivedi S, Nagaraj A, McPherson DD, Chandran KB. Three-dimensional finite element analysis of residual stress in arteries. *Ann. Biomed. Eng.* 2004; **32**:257–263.

[148] Liu SQ, Fung YC. Relationship between hypertension, hypertrophy, and opening angle of zero-stress state of arteries following aortic constriction. *J. Biomech. Eng.* 1989; **111**:325–335.

[149] Matsumoto T, Hayashi K. Mechanical and dimensional adaptation of rat aorta to hypertension. *J. Biomech. Eng.* 1994; **116**:278–283.

[150] Taber LA, Eggers DW. Theoretical study of stress-modulated growth in the aorta. *J. Theor. Biol.* 1996; **180**:343–357.

[151] Humphrey JD. Mechanisms of arterial remodeling in hypertension. *Hypertension* 2008; **52**:195–200.

[152] Elger DF, Blackketter RS, Budwig RS, Johansen KH. The influence of shape on the stresses in model abdominal aortic aneurysms. *J. Biomed. Eng.* 1996; **118**:326–332.

[153] Sacks MS, Vorp DA, Raghavan ML, Federle MP, Webster MW. In vivo three-dimensional surface geometry of abdominal aortic aneurysms. *Ann. Biomed. Eng.* 1999; **27**:469–479.

[154] Nicosia MA, Kasalko JS, P CR, Einstein DR, Kunzelman KS. Biaxial mechanical properties of porcine ascending aortic wall tissue. *J. Heart Valve Dis.* 2002; **11**:680–686.

[155] Kim J, Baek S. Circumferential variations of mechanical behavior of the porcine thoracic aorta during the inflation test. *J. Biomech.* 2011; **44**:1941–1947.

[156] Reeps C, Maier A, Pelisek J, Härtl F, Grabher-Meier V, Wall W, Essler M, Eckstein HH, Gee M. Measuring and modeling patient-specific distributions of material properties in abdominal aortic aneurysm wall. *Biomech. Model. Mechanobiol.* 2013; **12**:717–733.

[157] Vorp DA, Schiro BJ, Ehrlich MP, Juvonen TS, Ergin MA, Griffith BP. Effect of aneurysm on the tensile strength and biomechanical behavior of the ascending thoracic aorta. *Ann. Thorac. Surg.* 2003; **800**:1210–1214.

EIDESSTATTLICHE ERKLÄRUNG

Ich erkläre an Eides statt, dass ich die vorliegende Arbeit selbstständig verfasst, andere als die angegebenen Quellen/Hilfsmittel nicht benutzt und die den benutzten Quellen wörtlich und inhaltlich entnommenen Stellen als solche kenntlich gemacht habe.

Graz, am _____ _____

Datum Unterschrift

STATUTORY DECLARATION

I declare that I have authored this thesis independently, that I have not used other than the declared sources/resources and that I have explicitly marked all material which has been quoted either literally or by content from the used sources.

Graz, _____ _____

Date Signature